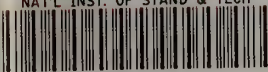


Reference

NBS
Publi-
cations

NBSIR 82-2617

NAT'L INST. OF STAND & TECH



A11106 261531

Technical Activities 1982

Office of Nondestructive Evaluation

U.S. DEPARTMENT OF COMMERCE
National Bureau of Standards
National Measurement Laboratory
Office of Nondestructive Evaluation
Washington, DC 20234

December 1982

Prepared for

U.S. DEPARTMENT OF COMMERCE
National Bureau of Standards
Washington, DC 20234

QC

100

.U56

82-2617

1982

NATIONAL BUREAU
OF STANDARDS
LIBRARY
JAN 18 1983
not acc-120
DC-100
120
12-2617
1982

NBSIR 82-2617

**TECHNICAL ACTIVITIES 1982
OFFICE OF NONDESTRUCTIVE
EVALUATION**

H. Thomas Yolken , Editor

U.S. DEPARTMENT OF COMMERCE
National Bureau of Standards
National Measurement Laboratory
Office of Nondestructive Evaluation
Washington, DC 20234

December 1982

Prepared for
U.S. DEPARTMENT OF COMMERCE
National Bureau of Standards
Washington, DC 20234



U.S. DEPARTMENT OF COMMERCE, Malcolm Baldrige, *Secretary*
NATIONAL BUREAU OF STANDARDS, Ernest Ambler, *Director*

TECHNICAL ACTIVITIES

TECHNICAL ACTIVITIES
TABLE OF CONTENTS

ULTRASONICS AND ACOUSTIC EMISSION

"EPRI/NBS Joint Program on Acoustic Emission,"	4
D. Eitzen, F. Breckenridge, N. Hsu and T. Proctor	
Task # 15770	
"Further Development of the NBS Conical Transducer,"	20
T. Proctor	
Task # 15770	
"Acoustic Emission for NDE Surveillance and Quality Control,"	25
J. Simmons, R. Clough, H. Wadley and R. Mehrabian	
Task # 15770	
"Ultrasonic Techniques for Nondestructive Evaluation,"	42
M. Linzer and S. Norton	
Task # 15760	
"Transfer Standards for Ultrasonic Power Measurements,"	46
S. Fick and C. Tschiegg	
Task # 15760	
"Improved Ultrasonic Reference Blocks,"	47
G. Blessing and D. Eitzen	
Task # 15760	
"NDE Terms and Definitions: Ultrasonics,"	50
D. Eitzen and M. Cadoff	
Task # 15770	
"Contactless Laser Generation and Optical Interferometric Detection of Ultrasonic Waves,"	51
M. Rosen, S. Fick, F. Nadeau and R. Mehrabian	
Task # 15760	

ELECTRICAL AND MAGNETIC METHODS

"Eddy Current Standards,"	53
A. McAlister	
Task # 15750	
"Eddy Current Testing,"	55
G. Free	
Task # 15750	
"High Frequency Broadband Eddy Current Probes for Improved Flaw Characterization,"	57
C. Fortunko and S. Padgett	
Task # 15750	
"Theoretical Modelling in Eddy Current NDE,"	67
A. Kahn	
Task # 15750	

"Magnetic Measurements," 69
 L. Swartzendruber
 Task # 15750

"Magnetic Particle Inspection Standards," 70
 L. Swartzendruber
 Task # 15750

RADIOGRAPHIC METHODS

"Development and Application of a Second Generation Image Intensifier
 for Real Time Microradiography," 71
 M. Kuriyama, W. Boettinger, H. Burdette, R. Spal
 Task # 15770

"Radiography," 73
 J. Motz, R. Placious and D. Polansky
 Task # 15760

"Design Study of a Facility for Neutron-Activation Autoradiography
 of Paintings at NBS Reactor," 79
 Y. Cheng and M. Ganoczy
 Task # 15760

"Development of High Optical Density Standards," 84
 J. Hsia, C. Popenoe and R. Booker
 Task # 15760

"Visual Acuity Requirements for NDT," 89
 G. Yonemura
 Task # 15750

OPTICAL AND INFRARED METHODS

"Optical Measurement of Surface Roughness," 90
 E. Teague, T. Vorburger, F. Scire, D. Gilsinn, M. McLay and
 C. Trahan
 Task # 15750

"Light Scattering from Grooves," 96
 G. White
 Task # 15750

"Holographic NDE," 100
 C. Vest
 Task # 15750

"Infrared Methods of Nondestructive Testing 104
 J. Cohen
 Task # 15760

"Evaluation of Organic Coatings Performance on Metallic Substrates
 Using Infrared Thermography 105
 M. Knight and J. Martin
 Task # 15760

NDE OF MATERIALS PROPERTIES

"Small-Angle Neutron Scattering Facility,"	107
C. Glinka	
Task # 15760	
"Investigation of SiC-Al Composite Material by Neutron Scattering," . .	110
H. Alperin and S. Singhal	
Task # 15760	
"Ultrasonic Applications to NDT and Materials Evaluation,"	112
G. Blessing	
Task # 15760	
"An Ultrasonic Residual Stress Reference Sample,"	113
G. Blessing, N. Hsu and T. Proctor	
Task # 15760	
"NDE Characterization of Thin Structurally Modified Surface Layers on Bulk Substrates,"	115
M. Rosen, F. Nadeau and R. Mehrabian	
Task # 15770	
"NDE of Composites,"	116
H. Ledbetter and J. Moulder	
Task # 15760	
"Green State NDE,"	121
T. Negas	
Task # 15770	
"Crystallization Kinetics Study Amorphous Zr-Cu By Ultrasonics and Microhardness Measurements,"	123
M. Rosen, F. Nadeau, and R. Mehrabian	
Task # 15770	
"Non-Destructive Characterization of Polymer Films via Ultrasonics," .	126
D. Hunston	
Task # 15770	
"Nondestructive Evaluation of Distributed Damage,"	131
E. Fuller, R. Fields, E. Case, S. Singhal and C. Glinka	
Task # 15770	
"Leak Rate Reference Standards,"	141
S. Ruthberg	
Task # 15770	
"Fluorescent Glass Standards for Use in Dye Penetrant Tests,"	146
R. Burke and D. Hancock	
Task # 15750	
"Dye Penetrant Crack Research,"	148
D. Lashmore and D. Kelley	
Task # 15750	
"Wear Condition Monitoring,"	152
A. Ruff	
Task # 15770	

"Engine Condition Monitoring Through Oil Analysis,"	153
S. Hsu	
Task # 15770	
"Electromagnetic Noise,"	159
U. Bertocci	
Task # 15770	
"Analysis and Modeling of NDE Round-Robin Data for Engineering Applications,"	161
J. Fong	
Task # 15770	
"Use of NDE in Rehabilitation and Preservation,"	165
J. Clifton	
Task # 15770	

Appendices

A. NDE Related Conferences	167
B. NDE Seminars Organized	168
C. Invited Talks by NDE Office Personnel	169
D. Awards	170
E. Technical and Professional Committee Participation and Leadership	172
F. Publications	175

INTRODUCTION

This report provides brief reviews of the technical activities in nondestructive evaluation (NDE) that were carried out by or for the National Bureau of Standards (NBS) in fiscal year 1982. Most of this work was supported and administered by the Bureau's Office of Nondestructive Evaluation but some of the articles describe activities that were funded by other NBS units or by non-NBS sources.

Technical activities in NDE have been conducted at NBS for many years but the NDE Program has been administered as a separate entity only since 1975. Summary reports such as this have been issued annually since 1978. A parallel series of reports provides annual bibliographies with abstracts for the Bureau's publications in NDE.

The principal function of these reports is to serve as an introduction to the Bureau's NDE Program. Many readers will want further details on specific aspects of the work or its outputs, and such inquiries are welcomed and encouraged, both by the principal NDE investigators (whose names and affiliations precede each of the articles in this report) and by the Office of Nondestructive Evaluation. Either can be addressed in care of NBS, Washington, D. C. 20234, or reached by telephone via (301) 921-1000. Requests for further information and suggestions for new NDE projects always receive prompt and careful attention.

There is evidence that the NDE Program continues to gain recognition in the national scientific and engineering communities. See, for example, the prestigious awards that were conferred this year upon participants in the Program (p.170). It is especially gratifying that NBS personnel received an IR-100 award for an NDE-related development for the fourth consecutive year. Other evidence of the Program's standing derives from the requests received for NDE expertise. For example, NBS engineers were called upon to ultrasonically characterize a crack in a titanium billet that had been destined for NASA's Galileo mission (see p.112). Also the Office of the Federal Inspector arranged for an NBS expert to review the weld radiographs of the Alaska-Canada gas pipeline. And similarly, NBS consultation was sought in connection with radiographic and liquid penetrant inspections of debris from the Hyatt Hotel disaster in Kansas City.

COMPARISON OF COMMON NONDESTRUCTIVE TESTING METHODS

Method	Characteristics Detected	Advantages	Limitations	Example of Use
Ultrasonics	Changes in acoustic impedance caused by cracks, nonbonds, inclusions, or interfaces.	Can penetrate thick materials; excellent for crack detection; can be automated.	Normally requires coupling either by contact to surface or immersion in a fluid. Orientation can present problems in detection or interpretation of defect.	Adhesive assemblies for bond integrity. Detection of cracks.
Radiography	Changes in material density from voids, inclusions, material variations; placement or internal parts.	Can be used to inspect wide range of materials and thicknesses; versatile; film provides record of inspection.	Radiation safety requires precautions; expensive; detection of cracks can be difficult.	Pipeline welds for penetration, inclusions, voids. Verification of parts in assemblies.
Eddy Currents	Changes in electrical conductivity or magnetic permeability caused by material variations, cracks, voids, or inclusions.	Readily automated; moderate cost.	Limited to electrically conducting materials; limited penetration depth. Interpretation of defect signals can be difficult.	Heat exchanger tubes for wall thinning and cracks. Verification of material heat treatment.
Visual-Optical	Surface characteristics such as finish, scratches, cracks or color; strain in transparent materials.	Often convenient; can be automated.	Can be applied only to surfaces, through surface openings or to transparent material.	Paper, wood, or metal for surface finish and uniformity.

Table I (continued)

Liquid Penetrant	Surface openings due to cracks, porosity, seams, or folds.	Inexpensive, easy to use, readily portable, sensitive to small surface flaws.	Flaw must be open to surface. Not useful on porous materials.	Turbine blades for surface cracks or porosity.
Magnetic Particles	Leakage magnetic flux caused by surface or near-surface cracks, voids, inclusions, material or geometry changes.	Inexpensive, sensitive both to surface and near-surface flaws.	Limited ferromagnetic material; surface preparation and post-inspection demagnetization may be required.	Railroad wheels for cracks. Detection of weld defects.

ELECTRIC POWER RESEARCH INSTITUTE/NATIONAL BUREAU OF STANDARDS
JOINT PROGRAM ON ACOUSTIC EMISSION

D. Eitzen, F. Breckenridge, N. Hsu, and T. Proctor

Mechanical Production Metrology Division

Center for Manufacturing Engineering

and

R. Clough, J. Simmons, C. Stockton, and H. Wadley

Metallurgy Division

Center for Materials Science

Acoustic emission (AE) techniques have great potential for determining and monitoring structural integrity. Acoustic emission signals contain potentially useful information about the location and intensity of defects and about the criticality of the defects in a structure under load. However, current signal reception methods do not preserve all of the available information and signal processing techniques, such as threshold counting, RMS recording, energy measurement, peak detection, and spectral analysis, and they often fail to extract the remaining information unambiguously. The difficulty in interpreting AE signals lies in the inherent complexity of the generating mechanisms, the transient wave propagation details, and the physics of the mechanical-to-electrical conversion process of the sensor.

The objective of the EPRI/NBS Joint Program on Acoustic Emission is to develop certain of the information needed to form a basis for the AE monitoring of electric power producing structures and to establish the feasibility of AE monitoring in simpler structures. The achievements of the first phase of the work were summarized in (1) and included:

- Contributions to data interchangeability of laboratory and field measurements through the development of a transducer calibration service.
- Advancement in the state-of-the-art of AE transducer design.
- Contributions to the reliability of AE field data through the development of calibrated sources.
- A better understanding of AE source behavior through theoretical modeling of AE sources.
- A better understanding of the limitations of conventional AE methods through a critical analysis of these methods.
- A framework for understanding the AE process from source to measured voltage.
- An analysis of the potential information in AE signals, an understanding of the modification to signals by wave propagation, experimentally verified theoretical predictions of remote displacement due to an AE source, and part of the basis for secondary sensor calibrations, all through the theoretical solution for wave propagation in a plate.

- Demonstration of the feasibility of determining the actual AE source function in glass and in steel from remote measurements using time-domain deconvolution.
- Development of a methodology for determining the significance of defects from received AE signals
- Development of several additional very promising signal processing techniques.

Some of these developments are being used in industrial applications, and others are being used by other AE researchers. While these accomplishments are consistent with the technical plan, additional information must be developed before utility power plant operators can obtain all the information from AE that is desired.

In this report we summarize some of our recent work towards quantitative acoustic emission measurements.

The acoustic emission work we describe here focuses on three areas:

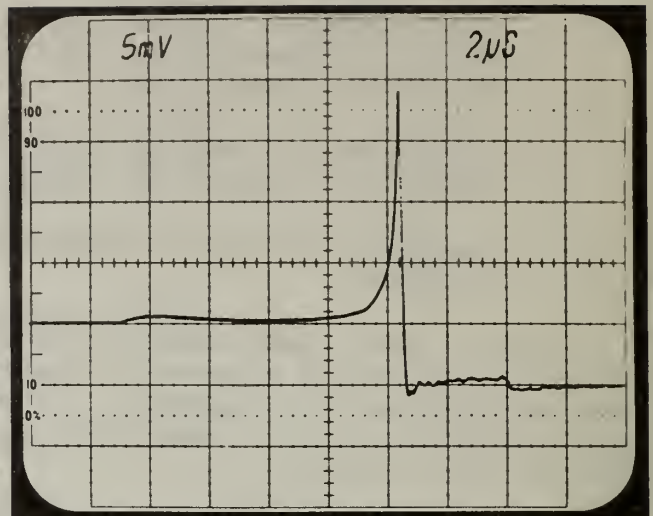
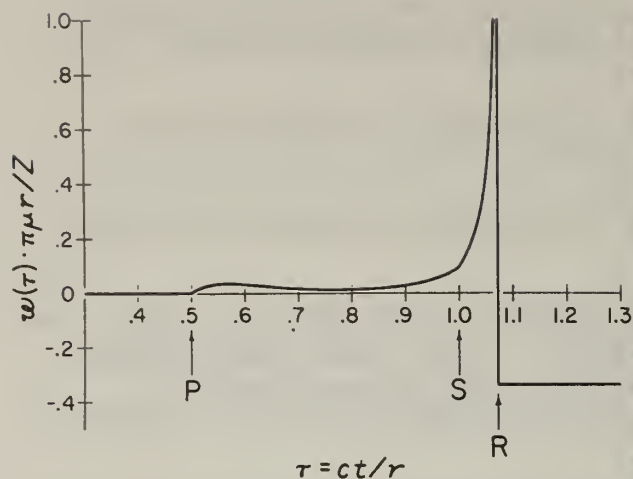
- calibration and sensor activities
- characterization of AE sources
- determination of source significance (activity terminated January 1982).

Significant progress towards implementing a quantitative acoustic emission measurement system for continuously monitoring structures has been made.

CALIBRATION ACTIVITIES

In January 1980 we implemented a calibration service for acoustic emission transducers using the surface-pulse method. Since then almost 300 calibrations have been performed, about half of these at the request of other laboratories or other NBS units and the rest for internal calibration improvements and quality control and for the development of the NBS Conical Transducer described below.

This calibration method makes use of the theoretical solution for the normal displacement of a half-space due to a point-force step-function. This prediction of normal displacement versus time is shown in Fig. 1 a. The surface-pulse calibration method also relies on our ability to mechanically produce a point-force step-function (we use the breaking glass capillary method (2-4)) and it relies on an accurate measurement of actual surface displacement using a capacitive transducer (5). Figure 1 b is a measurement of the surface displacement on an elastic block due to a breaking glass capillary event using the standard capacitive transducer.



a b
Fig. 1. Surface pulse -- theory and experiment.

A schematic of the calibration facility is shown in Fig. 2. The large steel block (A) weighs about 2200 kg and has polished faces. For calibrations by the surface-pulse method, the source (B) and standard (G) and unknown (H) transducers are all located on the top surface of the block. We have also started developing a through-pulse calibration method, in which the source is still located on the top surface but the unknown sensor is located directly below on the bottom surface of the block.

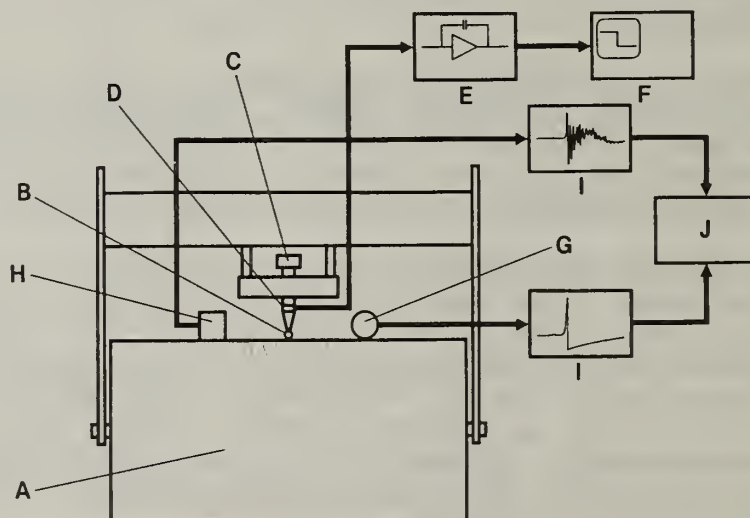


Fig. 2. Schematic of the AE sensor calibration apparatus. See (1) for details.

Further Developments of the Surface-Pulse System

Repeatability of calibration has been a problem with certain types of transducers. Although most transducers can be calibrated repeatably without using any special or unusual mounting practices, there are some which apparently require special measures to insure repeatability of the calibration. The measures which we have developed (described in last year's report) are, in our experience, sufficient to guarantee reproducible calibrations, although they are not always necessary. The reason why some transducers require these measures and others do not, is not clear to us at this time. We suspect that porosity of the wear face may cause air entrapment and resulting bubbles in the couplant layer, but this is not known.

Figure 3 shows three calibrations of a transducer with remounting in between. Previously, for some of the troublesome transducers, subsequent calibrations would differ by 20 dB or more, and, in general, there would be scant resemblance between the shapes of the curves. Using the new procedure dramatically increases the repeatability comparable to that shown in Fig. 3. Some transducer manufacturers have been notified of repeatability problems.

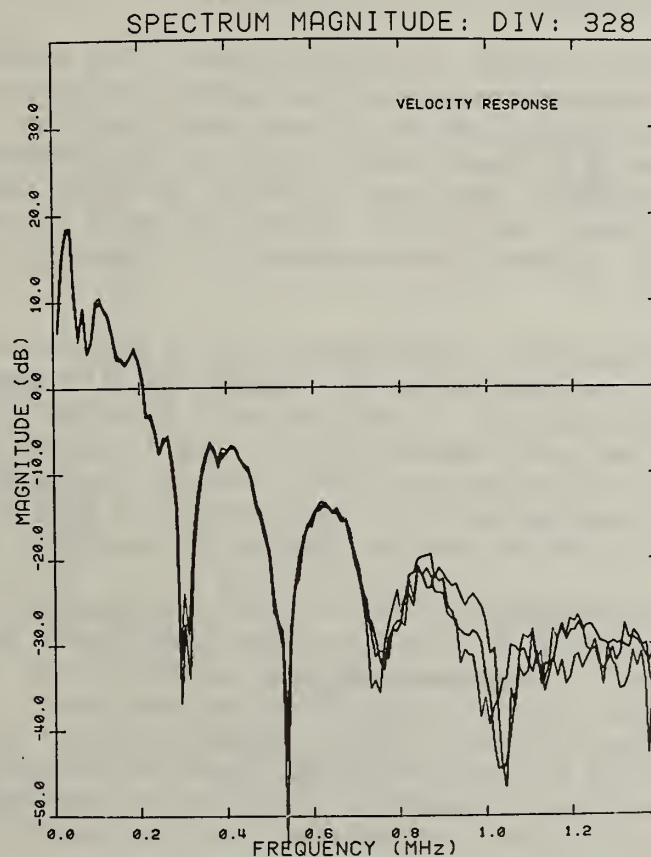


Fig. 3. Demonstration of calibration repeatability; three separate calibrations of a commercial sensor.

The transducer frequency response curves in Fig. 3 also exhibit the aperture effect which results in nulls in sensitivity. The locations of these nulls are reasonably predicted by the theory for a wave train crossing a circular aperture. The phase response for this transducer (not shown) has phase jumps at the null locations which are also predicted theoretically.

We have also developed an electronic pulse whose waveform is very similar to the surface-pulse waveform. This electronic pulse is used as a quality control tool to verify that the electrical and signal processing parts of the calibration facility have the proper characteristics and have not degraded.

Calibration Intercomparison

The Nippon Steel Corporation (NSC) offers a calibration service for acoustic emission transducers, in addition to the public calibration service offered by NBS. Both services provide measurement of the amplitude of response as a function of frequency for a transducer subject to predominantly Rayleigh waves on the surface of a steel block (the NBS service also retains the phase information). The methods used are, however, very different and it was decided that a comparison of results would be important to the AE community.

The NBS calibration method is outlined above. The method used by NSC is a reciprocity method in which transducers are calibrated in sets of three. Two transducers at a time are mounted on a large steel transfer block; one of the transducers is driven by a slowly varying gated continuous wave and the output from the other transducer is measured. Each of the three possible pairs is measured in the same way. Using this information and a theoretical reciprocity parameter the amplitude response of all three transducers can be determined.

For this comparison three transducers each of two different types were selected; one type is representative of transducers with complex behavior and the other type is representative of transducers with relatively simple response curves. Both types are sold commercially for use in acoustic emission work. The six transducers were calibrated, each three times by the surface-pulse method of NBS and each three times by the reciprocity method of NSC. They were then recalibrated at NBS to assure that no changes had occurred.

Typical results are shown in Fig. 4 for one type of transducer and in Fig. 5 for the other type of transducer. In each figure the average of the three NBS calibrations is compared with the average of the three NSC calibrations. Reference (6) describes the intercomparison in more detail. The two methods of calibration obviously yield very similar response curves; the details are in good agreement. The average of the correlation coefficients relating the two calibrations for one type of transducer was 0.76 and for the other type was 0.995; the lower correlation is associated with the type transducer with the more complex response.

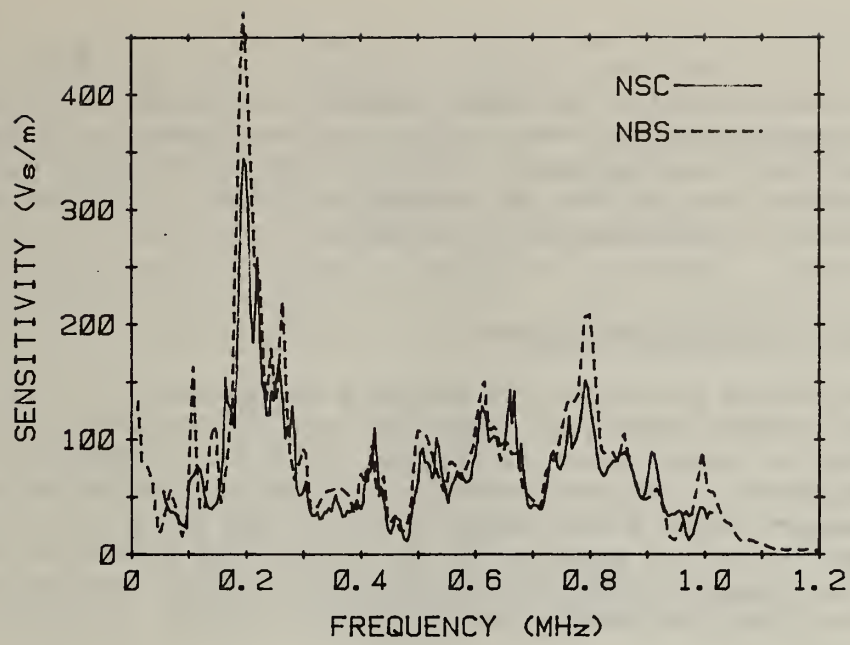


Fig. 4 . Average of NBS and of NSC calibrations of an AE transducer with more complex response.

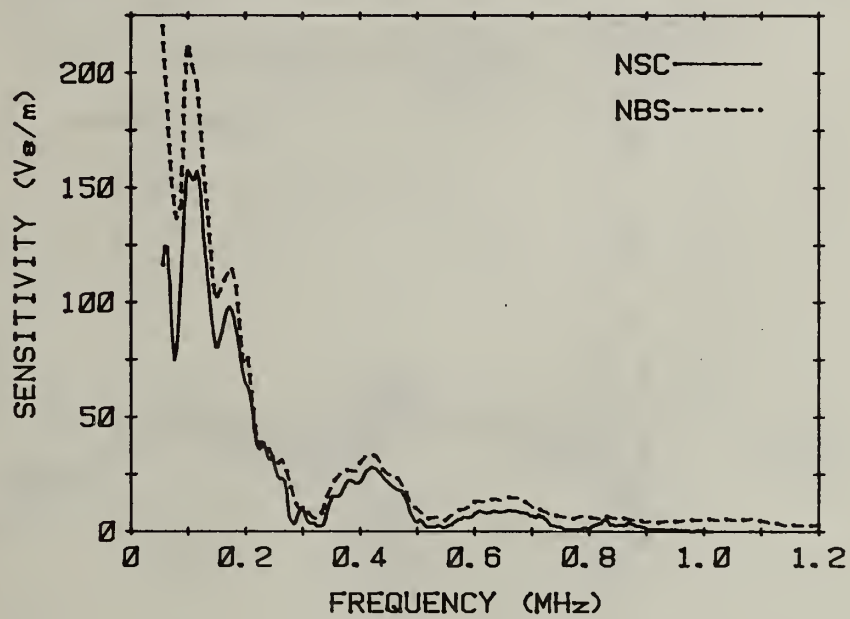


Fig. 5 . Average of NBS and of NSC calibrations of an AE transducer with simpler response.

While the qualitative agreement between the methods is quite good, the reciprocity method yields sensitivities that are lower than those by the surface-pulse method by an average amount of 16%. Efforts have been made to account for this difference, but, so far, no explanation exists. Further work is planned to try and narrow the gap between the methods.

Through-Pulse Calibration System

The technique of placing the standard transducer at a location symmetrical to that of the unknown transducer cannot be used for the through-pulse calibration method since the input source is located at the top surface of the block and the unknown transducer is located directly below on the bottom surface (epicenter). We may, however, compare the output waveform from the unknown transducer against the theoretical waveform of the thick-plate epicenter solution. The software for producing this solution has been written, and is available for incorporation into the calibration system.

Several through-pulse calibrations have been performed on the NBS Conical Transducer described on page 20 and the results compared with those from surface-pulse calibrations of the same transducer. For such a transducer, which has a small aperture, the results should be comparable. One such comparison is shown in Fig. 6. It is apparent from the figure that there is substantial

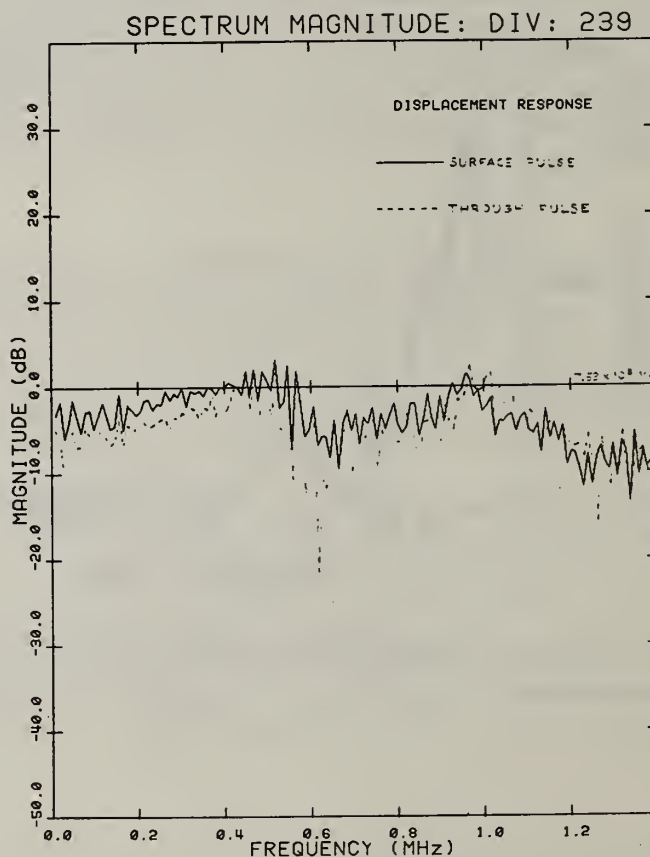


Fig. 6 . Calibration curve for the NBS Conical Transducer by the surface-pulse method and by the through-pulse method.

agreement between the methods, but that the absolute sensitivity indicated by the two calibrations differs by 1 dB. Recently, results have been obtained using a quasi-through-pulse configuration as shown in Fig. 7. In this case, both the standard transducer and transducer under test are located near to and equidistant from the epicenter. Using this quasi-epicenter configuration the output of the transducer under test can be compared to the output of the standard transducer. Measurements on the NBS conical transducer using this configuration, compare very well with the surface-pulse calibration of the same transducer. No appreciable differences result when these results are compared. More experiments of this type will be required before we can implement a through-pulse calibration service.

QUASI THROUGH-PULSE CALIBRATION

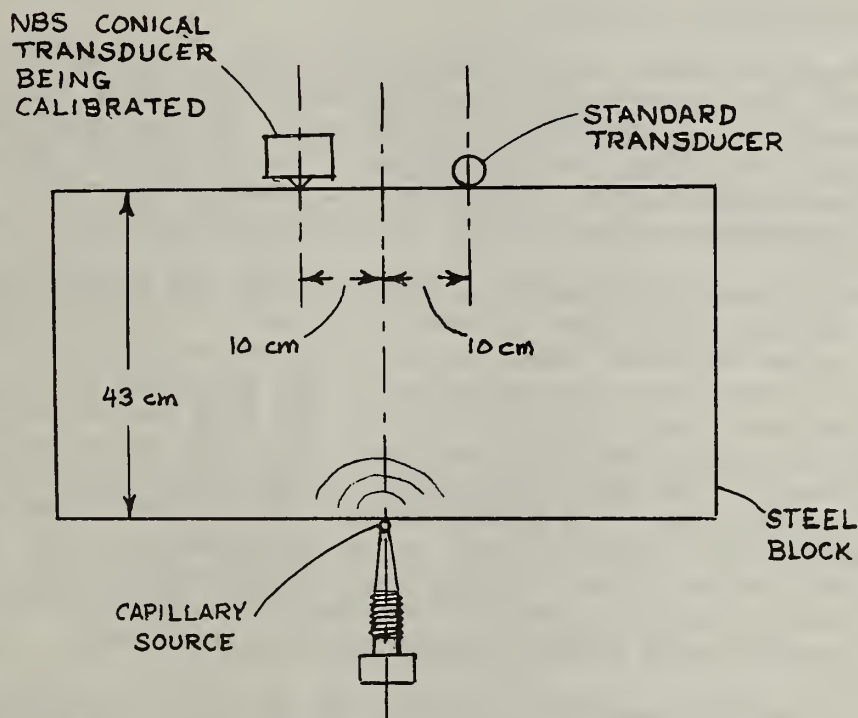


Fig. 7 . Schematic of quasi through-pulse configuration.

AE SOURCE CHARACTERIZATION

This part of our AE program is directed to the deconvolution of the AE source to determine its character and also to improved system calibration and improved defect location. The goal of source deconvolution is to remove the effects of the propagating structure and the receiving transducer on the evolved signal from the captured voltage-time waveform thus revealing the source characteristics using causal analysis. In (7) we have shown that for a plate and a capacitive transducer we can determine the actual source from the received signal using the inverse transform function. In order to do this source determination in more complex structures, we must experimentally determine the transfer function and develop general inversion techniques. To carry this out, we must generate a repeatable known source which can be used to determine the impulse response of complex structures. We also must develop a computational algorithm for inverting the impulse response to obtain the operator which deconvolves the source waveform. This work also provides a basis for system calibration and for minimizing flaw location uncertainty.

Repetitive Short Duration Source

Comparisons have been made between electrical spark impact sources and pulsed laser sources. The laser source is effective but the spark source has advantages including portability, simplicity, and low cost. We have perfected the charging, switching, and triggering circuits so that a few nanosecond, high-voltage current pulse with very low jitter can be discharged between electrodes. The resulting simulated AE waveforms in a structure are essentially identical one to another.

The mode of the spark source is controlled by the configuration of the electrodes. We have emphasized the configuration in which the plate (or structure) is one electrode and a second electrode is just above the plate surface. The stress wave thus generated in the structure can be modeled as evolving from local surface plasma heating, the same mechanism as when using a pulsed laser source for radiation heating. From such experiments we conclude that: the source is extremely reproducible, the detected signals agree well with theoretical predictions for a dipole source, the surface normal motion has a well defined negative pulse whose arrival is easily detected (a fact that could be exploited for precise ultrasonic wave speed measurements), and the rise time for the stress wave is less than one-half microsecond. Although the source generates EM signals, these can be easily isolated in the time domain.

This source also generates a shock wave in the air and so current experiments in a partial vacuum are being carried out to decompose the shock wave and the thermal effects. We are also beginning to investigate the use of a new commercial laser diode as a potential source. In order to increase the signal-to-noise ratio of such measurements, a computer program has been completed which permits signal averaging of 100 repeated source events in less than 10 seconds.

Signal Processing Techniques for Source Characterization

Substantial effort has gone into writing signal processing subroutines for the dedicated minicomputer based AE signal acquisition and processing system. These subroutines will be used to deconvolve the AE source function from the received signal in "complex" structures. These signal processing packages include:

- A fast convolution program with one time series in core memory and one time series on disk.
- A direct, exact time-domain deconvolution program based on error free matrix inversion.
- A program, based on least-squares fit, for finding the coefficient of the inverse filter by solving the Toeplitz normal equations.
- A program for power spectra estimation based upon the maximum entropy method developed by J. P. Burg.

We have also worked on the deconvolution of the digitized signals in the time domain. In order to evaluate the various approximation techniques, the epicenter impulse response function and its exact inverse have been used for comparison (7). Results using a least-square approximate deconvolution are rather disappointing. While an approximate inverse function is a reasonably "good" approximation of an exact inverse function, the deconvolved displacement is sometimes far from the input. Further examination by convolving the impulse response and the approximate inverse reveals that a 10% error is present in the result which accumulates for a step-function source. We have shown that the accuracy of the approximate deconvolution is signal dependent. It is expected that if the source signal is cyclic, then the deconvolved result will be much better than for the step-function source. Similar comparisons have been made for other types of sources for the epicenter configuration.

Our current conclusions on deconvolution are:

- For the epicenter case one can do an excellent job deconvolving to obtain an accurate characterization of the source.
- For the source and receiver on the same surface of "a half space," again an excellent deconvolution is possible.
- For other cases it appears that an approximate solution must be sought (e.g., least-squares) and one should make use of a priori knowledge about the source. This can result in an accurate characterization of some sources but not necessarily all sources.

A sequence of controlled experiments have also been designed and started to determine the significance of information content in the detected signal. The control variables include different "AE" sources, different source-detector configurations, and different detectors. Preliminary results show that with a

high-fidelity transducer such as the NBS Conical Transducer described on page 20, the detected signals from different sources are qualitatively different. However, with commercial resonant transducers, the detected signals appear qualitatively the same even though the frequency content of the sources are completely different.

Further work is planned on analysis of information in the detected signal and several additional processing schemes will be attempted after the new data acquisition system is complete.

Data Acquisition System

The new data acquisition system is nearing completion (planned for September 1982). It is centered on a new generation, very high speed mini-computer. Some of the special features of the system include:

- CAMAC module transient capture, permitting high sample rate (20 MHz), long duration (128K word record length), transient recording capability for subsequent processing of an entire AE event.
- Double precision capability, especially needed for theoretical calculations such as those of the plate solution.
- NBS Bus (and CAMAC interface) for easy flexible interfacing of a wide range of instruments.
- "High-power" mini-computer, featuring 32 bit words and a 1M core.

While the data acquisition system is essentially complete some additional software is needed to complete the processing packages.

MATERIALS EFFECTS AND CRACK CHARACTERIZATION IN STEEL PLATES

The milestones of repeatedly producing AE in A533 steel plates and of developing a multichannel source characterization facility for quantitative measurements of AE sources have been completed. With the exception of checking the reproducibility, which is best done with a multichannel system, the goal of reliably producing AE in A533B steel is complete. The development of a multichannel source characterization facility is also complete. The system has been used to investigate a high-power pulsed laser source. Activities in this task were terminated January 1982.

Reproducible AE in A533B Steel Plates

The generation of reproducible AE in A533B steel plate has been studied using the indentation technique described previously (8). This steel is typical of nuclear reactor pressure vessels and a method of producing repeatable AE in this material would be very helpful in studying the significance of AE sources. The as-received A533B steel plate is quite ductile and thus does not readily produce local stress concentrations which could generate AE through rapid, localized load drops. Therefore, a systematic study was performed on the effects in A533B nuclear grade pressure vessel steel of temper embrittlement augmented by hydrogen charging. The temper-embrittled condition is one which could occur to some extent in an A533 weld region in the field. Hydrogen is a fission product.

It was found that this method worked quite well and that a combination of grain coarsening at 1100 °C, aging at 500 °C up to 20 days, and hydrogen charging produced a substantial increase in AE activity (9). Our results demonstrate that by controlling the heat treatment and charging with hydrogen, the relatively quiet as-received A533B can be converted to a highly emissive material.

Understanding of this phenomenon is further enhanced by a stress analysis of the indentation. There is a compressive zone immediately under the indenter during loading which produces a hemispherical region of triaxial tension at one or more diameters away from the indentation. Microcracks nucleate during indentation up to 200 kg in temper-embrittled A533B. Micrographs indicate that debonding occurs at the Mn inclusion interface. No larger microcracks were found so that this is the source of emission in the uncharged material.

In hydrogen-charged material, macroscopic (200 microns) cracks were found. In addition, there is a region of enhanced hydrogen concentration near the surface which we propose is responsible for microcracks in hydrogen-charged material being generally either surface-connected or shallow subsurface types. This leads to the occurrence of cracks at the side, rather than under the indenter as was found previously for tool steels that were not hydrogen charged (9). These appear to nucleate at MnS inclusion. Although the crack is on the order of 200 microns in size, this is acoustically small relative to the shortest wavelength examined, here about 2400 microns, so that a crack will appear to be a "point source".

To summarize, a method has been found which is useful for producing AE in A533B steel plates. Through controlling the heat treatment and through additional methods of modifying the material condition, the amount of AE can be controlled while still keeping the material relevant to conditions in the weld region. This method is now applicable for use on larger plates of A533B steel, where signal reproducibility could be checked with the multichannel system.

Multichannel Analysis System

Another unique approach being taken in our AE research program is the development of a multi-channel AE signal acquisition and processing system to permit more complete deconvolution of the AE stress drop source. This approach, which originated at NBS (10), is also being implemented at AERE Harwell and at other laboratories. The multichannel system is complete and ready for testing. Two octagonal steel plates, 18 inches across, have been obtained. An O2 tool steel plate has been hardened by austenitizing and water quenching. Preliminary tests using such a procedure show that multiple, reproducible AE signals can be obtained during indentation. A second plate of A533B steel has been machined prior to heat treatment. The indentation system consists of a pneumatic loading indenter, a Faraday cage to minimize RF noise, and an XY translation table for positioning the plate specimen.

For the multichannel system a set of six wideband transducers (the new NBS Conical Transducer design) has been fabricated; also, there are at least six channels of preamplification, anti-aliasing filters, and amplification up to 100 dB with a bandwidth in excess of 10 MHz available for the system. Computer codes

for the dynamic plate response have been extended to include all surface dipoles, and extensive calculation have been made of emission signals on a stainless steel plate which will be used for additional tests on the wideband transducers. Computer codes for deconvolution and comprehensive driver programs for our high-speed interface are being prepared on our minicomputer system which, in turn, is being extensively expanded to carry out novel data processing methods. The computer interface is now operational with some noise problems being solved. This completes the current generation multichannel system.

Laser Generated AE

We have begun evaluating the multichannel system and the multichannel deconvolution approach to determining AE source functions using simulated AE which has been laser generated. A Nd:YAG laser has been used to produce predictable, reproducible, thermoelastic dipole sources that generate elastic waves in a large plate. The elastic displacements due to elementary force dipoles and a force dipole combination representing the thermal expansion for a laser source have been calculated for an isotropic elastic plate at epicenter and at one and five plate thicknesses on both plate surfaces. Experimental results show close agreement with the calculated waveforms.

The elastic waves generated on the surface on which the source is located (Figs. 8 & 9) are dominated by a Rayleigh wave whose velocity was $2.89 \text{ mm} \cdot \mu\text{s}^{-1}$ for 302 stainless steel. Careful measurements of this velocity could provide a useful non-contacting method of deducing the surface elastic properties. This method could also be used during metals processing to detect the occurrence of surface cracking for NDE applications: the time of the Rayleigh wave arrival at several transducers would give a very precise location of the source.

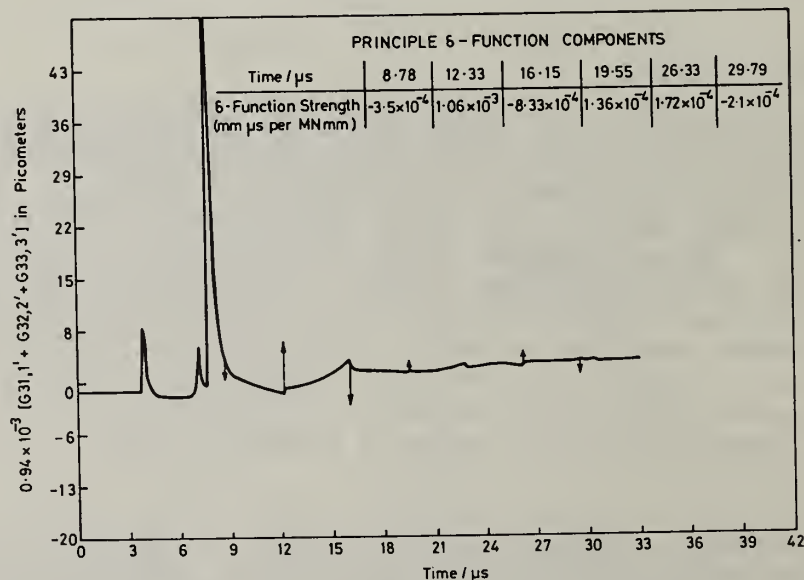


Fig. 8 . Predicted displacement waveform at one plate thickness from the source for a $2.55 \times 10^{10} \text{ Wm}^{-2}$ flux density source.

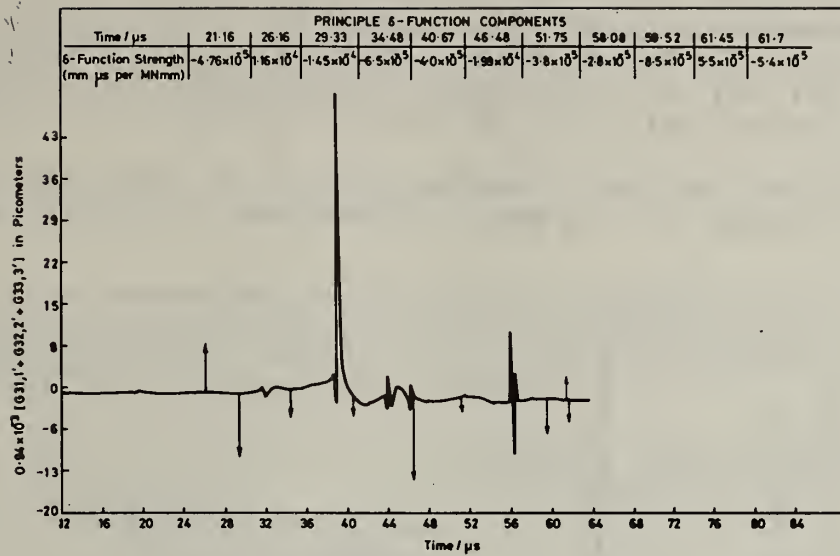


Fig. 9 . Predicted displacement waveform at five plate thicknesses from the source.

On the opposite surface, at the epicenter (Fig.10), clear longitudinal and transverse wave arrivals can be seen thereby suggesting the possibility of bulk microstructure characterization. Away from the epicenter (Figs.11&12), the waveforms for moderate duration sources are dominated by head wave arrivals.

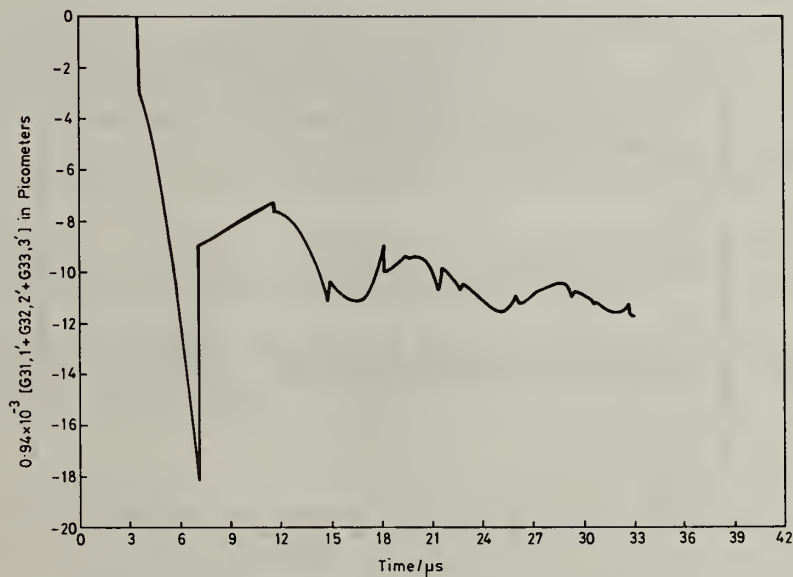


Fig.10 . Predicted epicenter displacement for a $2.55 \times 10^{10} \text{ Wm}^{-2}$ flux density laser source.

Great care has to be exercised with these from an acoustic emission point of view if source location is attempted because they do not have a well defined wavespeed. For example, the dominant head wave one plate thickness from epicenter had an apparent velocity of $2.89 \text{ mm} \cdot \mu\text{s}^{-1}$ while that at five plate thicknesses was $5.74 \text{ mm} \cdot \mu\text{s}^{-1}$. This may be a major reason for inaccurate source location in thick plates in many current applications of acoustic emission.

The results obtained form a starting point for AE source characterization studies and this aspect could be more fully developed in following work.

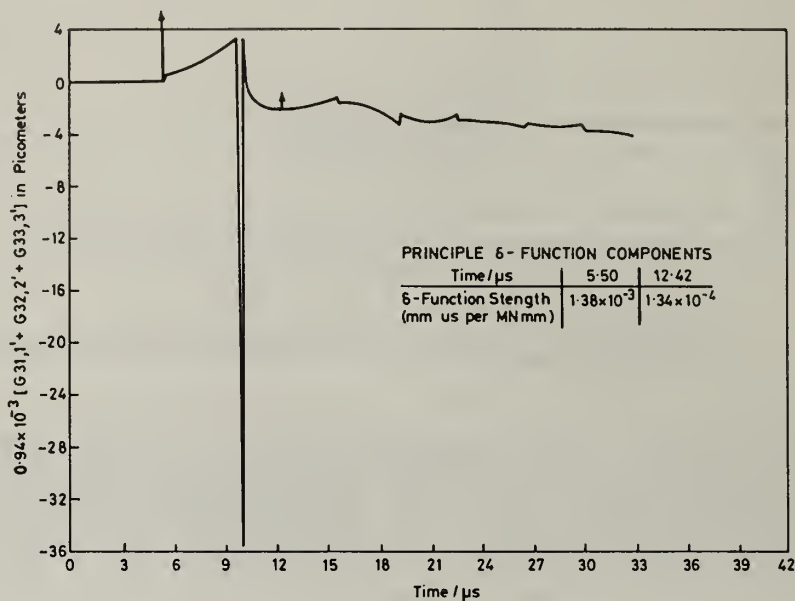


Fig. 11. Predicted displacement one plate thickness from epicenter for a $2.55 \times 10^{10} \text{ Wm}^{-2}$ flux density source.

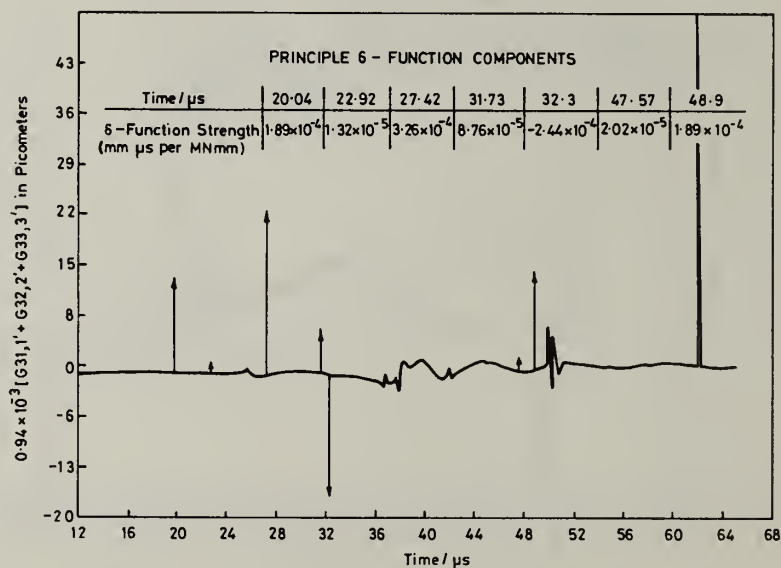


Fig. 12. Predicted displacement five plate thicknesses from epicenter for a $2.55 \times 10^{10} \text{ Wm}^{-2}$ flux density source.

ACKNOWLEDGMENT

Much of this work is part of the Electric Power Research Institute/National Bureau of Standards Joint Program on Acoustic Emission (RP 608). Some of the work is partially supported by the Office of Naval Research.

REFERENCES

1. D.G. Eitzen, F.R. Breckenridge, R.B. Clough, E.R. Fuller, N.N. Hsu, and J.A. Simmons. Summary of Fundamental Developments for Quantitative Acoustic Emission Measurements. EPRI Report NP-1877, June 1981. (An EPRI Report which more fully describes this program is in press).
2. F.R. Breckenridge, C.E. Tschiegg, and M. Greenspan. Acoustic Emission: Some Applications of Lamb's Problem. Journal of the Acoustical Society of America, 576, 1975, pp. 626-631.
3. N.N. Hsu and F.R. Breckenridge. Characterization and Calibration of Acoustic Emission Sensors. Materials Evaluation, 39, 1981, pp. 60-68.
4. F.R. Breckenridge. Transducer Calibration by Means of the Seismic Surface Pulse. Journal of Acoustic Emission, Vol. 1, No. 2, April 1982.
5. F.R. Breckenridge. Surface-Wave Displacement: Absolute Measurements Using a Capacitive Transducer. Journal of the Acoustical Society of America, 69, pp. 1177-1185.
6. F.R. Breckenridge, T. Watanabe, and H. Hateno. Calibration of Acoustic Emission Transducers: Comparison of Two Methods. Proceedings of the Sixth International Acoustic Emission Symposium, Japan, Oct. 31-Nov. 3, 1982.
7. N.N. Hsu and D.G. Eitzen. The Inverse Problem of Acoustic Emission--Explicit Determination of the AE Source Time-Function. Presented at the AF/DARPA Review of Quantitative NDE, August 1981, Boulder, CO.
8. R.B. Clough and J.A. Simmons. Reproducible Acoustic Emission Signatures by Indentation in Steels. Materials Evaluation, October 1981.
9. R.B. Clough and H.N.G. Wadley. Indentation Acoustic Emission Studies of Temper Embrittlement in A533B Pressure Vessel Steel. In preparation.
10. J.A. Simmons and R.B. Clough. Theory of Acoustic Emission. Dislocation Modelling of Physical Systems. M. Ashby and J. Hirth, eds. Pergamon Press, Oxford, 1981, pp. 464-467.

FURTHER DEVELOPMENT OF THE NBS CONICAL TRANSDUCER

Thomas M. Proctor

Mechanical Production Metrology Division

Center for Mechanical Engineering

Figure 13 shows a schematic of one of the configurations of the new NBS Conical Transducer for acoustic emission (1,2). The transducer measures dynamic normal surface displacements nearly as faithfully as the standard capacitive transducer used in the NBS AE calibration facility but is more rugged and is one to two orders of magnitude more sensitive --about as sensitive as commercial AE transducers. It consists of a small conical piezoelectric element and a large backing, usually of brass.

By design, this transducer has an area of contact which is small relative to Rayleigh wavelengths in the working range (nominally 0.1-1 MHz) thus eliminating the aperture effect which plagues most AE transducers. The brass backing block is so large and so lossy that waves entering it via the conical element are largely dissipated by the time they reflect back to the element. Thus the backing block may be approximated as an elastic solid half-space. On this basis, it can be shown that, for low frequencies, the transducer functions as a displacement sensor.

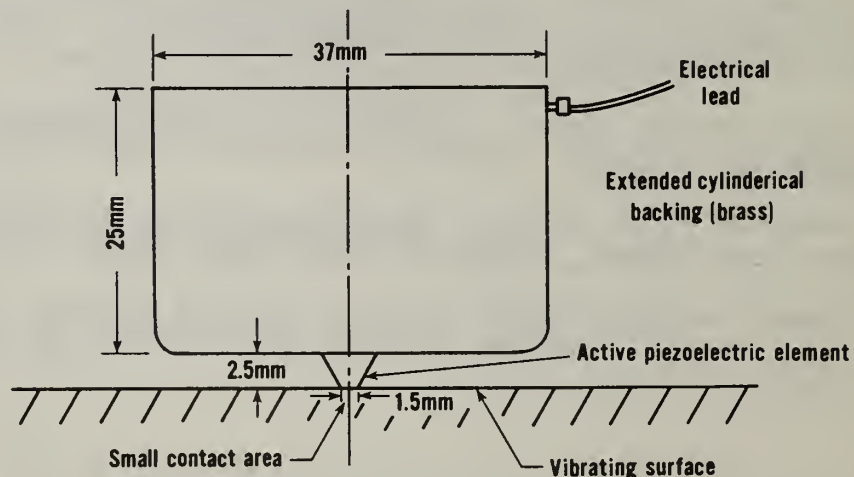


Fig. 13. Schematic of one version of the NBS Conical Transducer.

Shown in Fig. 14 are two views of the transducer producing the flattest response so far. The idea behind the rather complicated backing is to have all reflecting surfaces at different angles and distances to the piezoelectric cone element so that reflecting waves are not coherent. The response of this transducer is shown in Fig. 15 and compares very favorably with the theoretical waveform and with the capacitive transducer response shown in Fig. 1 a, and b. Its response is much more accurate compared to the response of a typical commercial transducer (shown in Fig. 16).

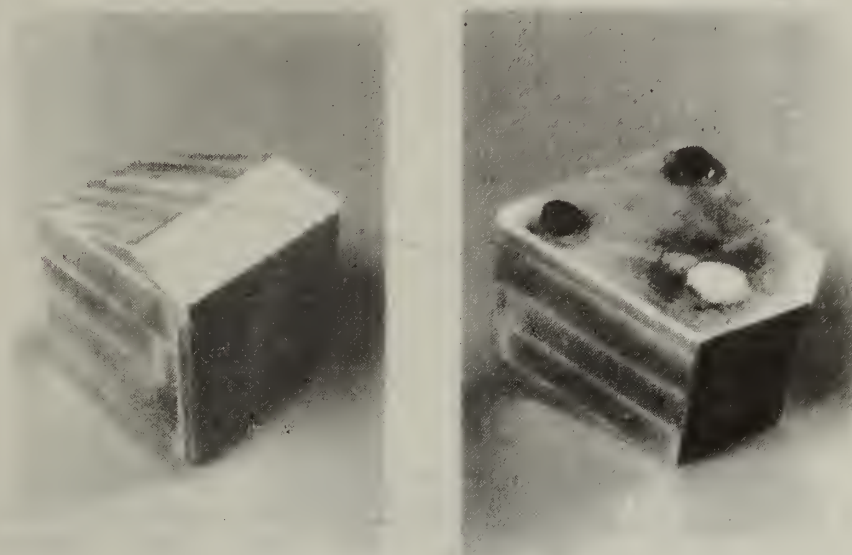


Fig.14 . Two views of best behaved piezoelectric transducer thus far produced.

Additional evidence of the new transducer's ability to measure dynamic displacement is presented in Fig.17 . The inset curve gives the theoretically predicted normal displacement of a plate for a sensor located two thicknesses away from and on the same side of a plate as a point-force step function input. The lower curve is the displacement measured by the NBS Conical Transducer on a 3 cm thick glass plate with the NBS transducer located 6 cm away from a breaking glass capillary. The theoretical curve is from Pao et al. of Cornell and was independently calculated by Simmons, Hsu, and Willis at NBS.

When the transducer was first developed, a satisfactory theory to describe its function was not available. In order to determine the importance of various features of the transducer several series of experiments were performed. One series of response measurements was made as the large backing was reduced in size in a systematic fashion. The importance of the aperture was investigated by another series in which the front contact electrode area was reduced in successive steps. The effects of variation in backing symmetry have been investigated in a similar fashion. This empirical approach has helped us understand the operation of the transducer. As a result, we have found that backing size and geometry, small aperture size and conically shaped active element are all important features of this design.

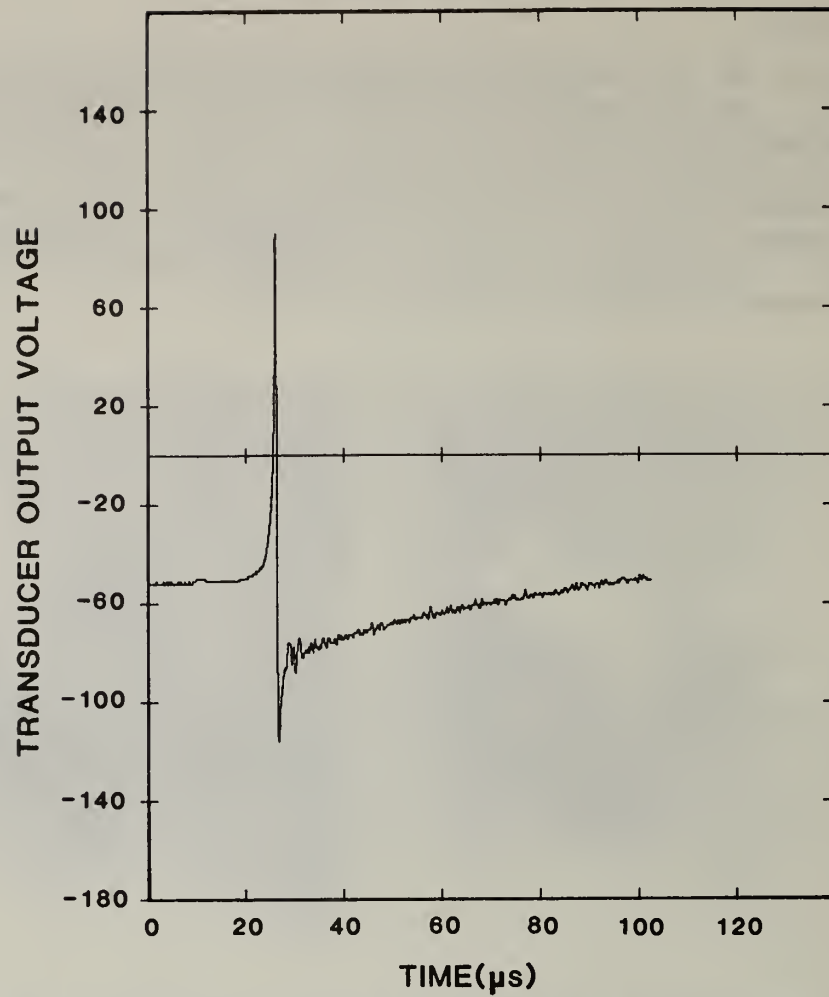


Fig.15 . Measurement of surface pulse using the transducer shown in Fig.13 .

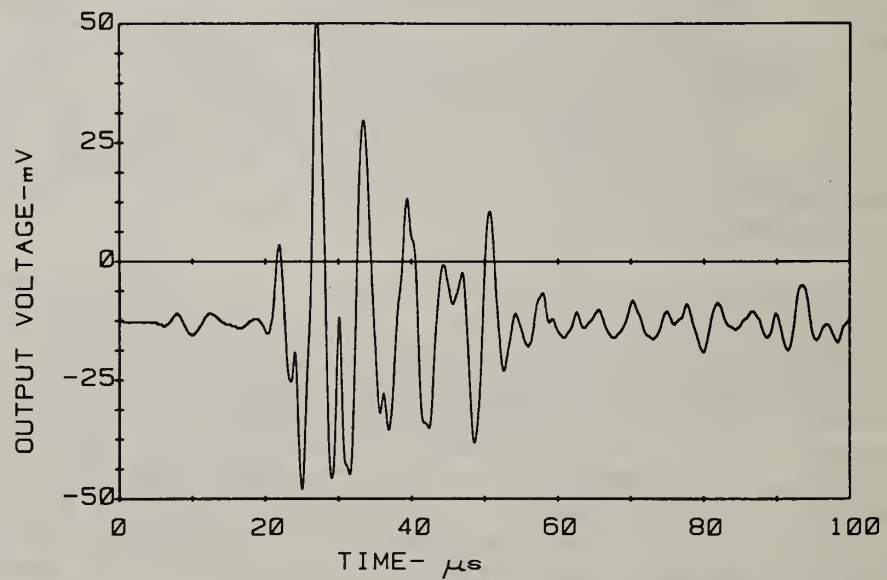


Fig. 16. Detection of surface pulse using a typical commercial transducer.

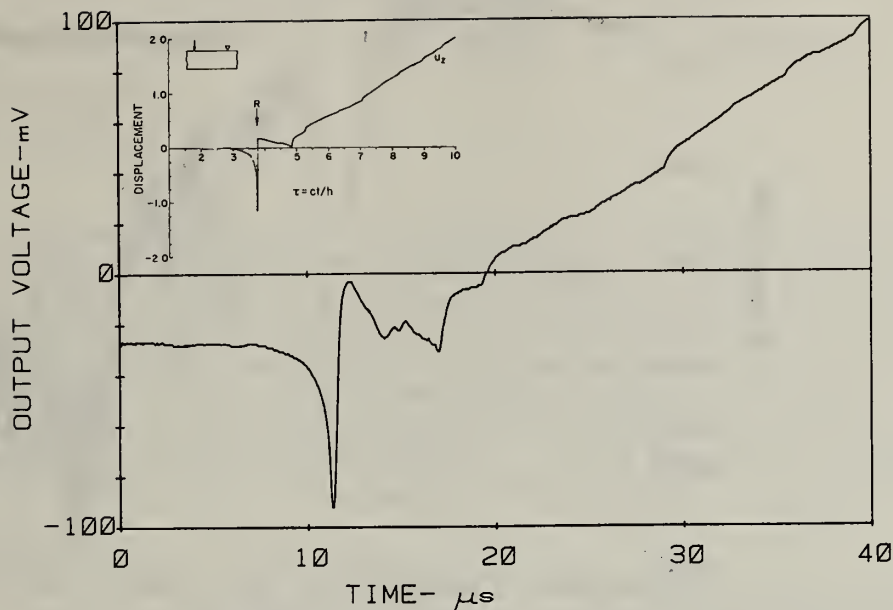


Fig.17 . Comparison of theory and measurement using the NBS Conical Transducer located two thicknesses away from and on the same side of a plate as the source.

A preliminary theory of operation was recently developed for the NBS Conical Transducer. It takes into consideration the mechanical impedance properties of the three parts of the system, namely the driving block (steel half-space as viewed by the circular area of the contact face), the conical element (treated as a conical horn), and the backing block (brass half-space as viewed by the circular area of the cone's base). This theory has had some success in predicting the response of several transducers which were variations of the NBS Conical Transducer. Figure 18 shows a comparison of the theoretically predicted and the measured sensitivity of a transducer constructed with a cylindrical piezoelectric element (for the purpose of this comparison). This cylindrical element permits a simplified calculation but should be a reasonable check of the modeling approach. While the results show the approximate theory is good, an improved theory is being developed. It is hoped that this theory may aid in optimizing the parameters of transducers of this type and contribute generally to understanding of AE and ultrasonic transducers coupled to an elastic medium.

As a participant in the DARPA/Naval Air Development Center/Battelle Program on In Flight AE Monitoring of Aircraft, we have developed a transducer assembly which uses the regular cylindrical brass backing type transducer but also has an internally contained preamplifier, front electrode protection, and a ground shield. With the older type backings, the final shielded unit is 2 inches in diameter and about 2 inches in length.

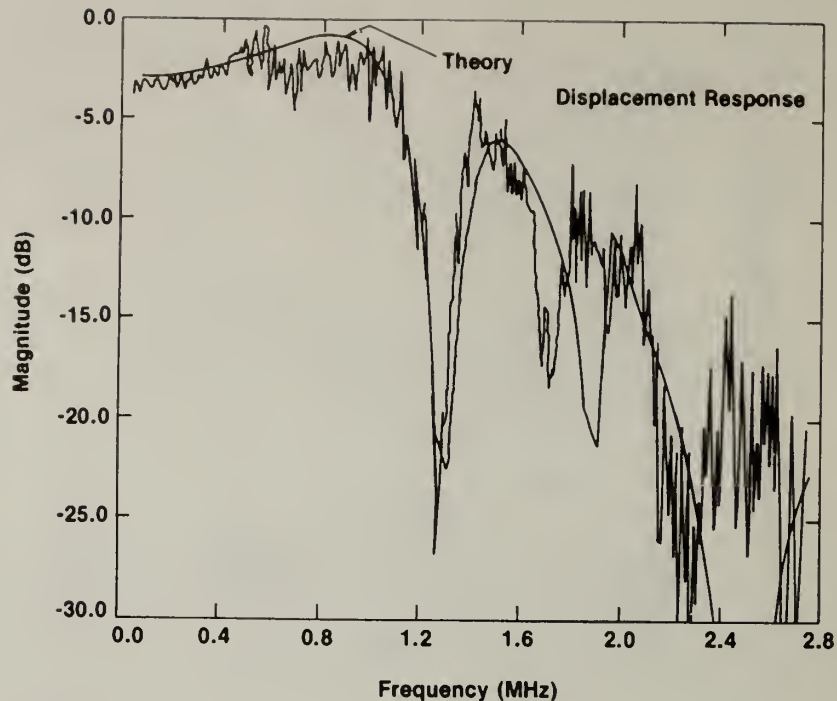


Fig.18 . Theory and measurement of NBS-type transducer with cylindrical element.

We are also working on special backing materials to permit a smaller transducer design. We have constructed transducers with 1/4 the volume of earlier models but with the same fidelity of response. This new "down-sized" transducer is one-inch in diameter and only 5/8 of an inch long, which makes it comparable in size to most conventional transducers.

Our future plans include optimization of the design using a new theoretical model of the transducer. Parameters subject to optimization include material properties of the backing and piezoelectric element and shape of the element. Plans also are underway to develop a "high-fidelity" displacement transducer for tangential surface motion.

REFERENCES

1. T.M. Proctor. Improved Piezoelectric Transducers for Acoustic Emission Signal Reception. J. Acoust. Soc. Am. Suppl. 1, Vol. 68, Fall '80, p. 568.
2. T.M. Proctor. An Improved Piezoelectric Acoustic Emission Transducer. J. Acoust. Soc. Am. 71 (5) May 1982, pp. 1163-1168.

ACOUSTIC EMISSION FOR NDE SURVEILLANCE AND QUALITY CONTROL

J. A. Simmons, R. B. Clough, H. N. G. Wadley, and R. Mehrabian
Metallurgy Division
Center for Materials Science

Acoustic emission (AE) refers to a technique for the measurement of elastic stress waves emitted by rapid dynamic changes of state in materials. AE can be used to detect, monitor and measure the occurrence of plasticity, cracking, phase transitions and corrosion where they are accompanied by rapid stress changes. Consequently, AE has unique potential as a passive surveillance tool for the control of microstructure during materials processing, monitoring, fabrication of components and detecting, locating and characterizing flaw growth in structures. It also promises to provide a new tool for the quantitative measurement of the dynamics of material changes of state.

The structure of the stress waves emitted during acoustic emission is complex. Until recently, the general formalism establishing the relationships between stress change sources, the amplitude and temporal character of the emission they provide was only poorly understood. Recent work at NBS has addressed these problems. This work demonstrated:

- Existing measurement methodologies that have evolved to date make use of only a small fraction of the potential information contained in acoustic emission signals.
- The character of the emission is controlled by synergistic interactions between metallurgical variables and the stress state.

Nevertheless, the technique is finding increasingly successful application for monitoring cracking and predicting failure in ceramics, composites and metal weldments. However, it also has the potential to make a great contribution to the monitoring of metals processing where it could provide essential data for feedback control improving quality and productivity, but this has received scant study in the past.

At NBS a unique approach to the measurement of acoustic emission is being developed, which has as its objective the reconstruction of the source dynamics. This technique, which is similar to that currently revolutionizing the field of seismology, utilizes simultaneous high speed measurements (at different locations) of the initial wavefronts from individual emissions to allow quantitative reconstruction of the source stress drop. At least six observation channels are necessary for reconstruction of the six stress drop components as a function of time. To implement this approach the

following steps have been taken:

- A computer based multichannel AE system has been constructed.
- New experimental methods for controlled generation of AE sources developed.
- New theoretical techniques for forward modelling and inverse filtering have been devised for signal analysis.
- Critical experiments have been planned and preliminary studies completed for verification of multichannel AE analysis using Nd:YAG laser and plate geometry.
- Plans and preliminary studies made to correlate AE signals, microstructural analysis and thermodynamic parameters of rapidly solidified electron beam source in aluminum and an aluminum alloy.
- A set of critical experiments designed to establish the validity of these new measurements methods.

Parallel studies drawing upon the above techniques, have examined flaw growth as part of the joint NBS/EPRI program in AE and explored the use of AE for monitoring rapid solidification as part of the DARPA/NBS project in Rapid Solidification and NDE.

Our program during the past year can be broken down into four categories:

- (1) Theoretical advances.
- (2) Source characterization developmetns.
- (3) Experimental methods for the controlled generation of AE in A533B pressure vessel steel.
- (4) AE studies of rapid solidification.

(1) Theory advances

The theoretical framework for acoustic emission sources rests upon a Green's function formalism for stress waves generated by changes in internal stress induced when a source responds inelastically to structural loads. The forward formulation, in which the emission from a source of known character is deduced, has been published (1). There the representation of an AE source event was first given in multipolar expansion form and then restricted by two assumptions, to avoid the technological difficulties associated with high moment components, namely, the source is infinitesimal in size and all its components have the same time history. The key restriction for validating these assumptions is a band limiting process to restrict the frequencies to a region called the Informative Band. Estimates of the limiting frequency for the band were given as a function of defect size and

shape. Within the information bandwidth one can develop a transfer function formalism which allows one to consider transmission of the information frequency by frequency from the source through the structure to the detector: outside this band specific models of the details of the AE mechanism are required to deduce AE signals.

The general formulation of acoustic emission from plasticity, cracks, and phase transformations was then developed within the pseudopoint approximation using the concept of retarded dipole density to deal with the problem of time delays of the emission from propagating cracks and phase change regions. The radiation patterns for defect sources are highly directional and depend on source type and orientation (see Figures 19-21). Finally, the concepts of stress controlled and materials controlled acoustic emission were introduced and the synergistic relation between the ambient stress field and microstructural constraints were discussed.

Subsequent work has concentrated on the inverse problem for deducing the character of the stress drop components from measured acoustic emission signals. This is one of a class of "remote sensing" problems in which small amounts of measurement error or noise can obscure the information about the source signal. Sophisticated signal processing techniques are demanded.

The transfer function formalism leads to simultaneous convolution equations describing the acoustic emission signals in terms of the source stress drop components, the structure response, and the transducer characteristics. These simultaneous equations can be reduced to a deconvolution equation which is, in general, even more ill-conditioned than deconvolution problems encountered in time series applications.

A singular valued decomposition (SVD) algorithm developed in conjunction with D. O'Leary (Division 711) (2), has been applied to such signals. Since the full SVD algorithm is prohibitively demanding of computer resources for problems of the type required in acoustic emission, the above procedure uses a reduced dimension representation similar to the Rayleigh-Ritz procedure. The SVD algorithm both inverts and filters to produce a number of candidate solutions to the inverse problem. The results obtained, while promising, suffer from the difficulty that it is difficult to select the "best" approximation from among the candidate solutions.

To help deal with this problem and to examine the possibility for new pattern recognition techniques for source signatures, an alternate approach is being studied. This approach uses a modification of the Z transform of the time series which is to be inverted, which allows powerful complex variable techniques to be combined with linear algebraic methods for inverse filtering. In this approach the Z transform of the time series becomes a polynomial of high degree

(typically 512 or higher). An entirely new set of algorithms has been developed which finds all the zeroes of such high degree polynomials and uses these for both pattern recognition purposes and to develop new noise filters. These are supplemental to those obtained in the SVD approach and can be used to greatly reduce solution noise while allowing "a priori" information about the frequency content of the solution to be factored in.

These new algorithms, which must be applied to time series of great length to be usable in acoustic emission inversion, are currently being employed to find robust procedures for deconvolution. An example of the types of candidate solutions obtained in carrying out deconvolution (in this case of a 43 point time series based on the surface-to-surface Green's function for a half-space) is illustrated in Figures 22-28.

(2) Experimental verification of source characterization

The objective of source characterization is the measurement of the magnitude, orientation and time dependence of the stress drop tensor of acoustic emission sources. The stress tensor provides the basic information required for defect severity assessment in NDE and, in the laboratory, promises to provide dynamic information that would greatly advance our understanding of the dynamics of metal deformation and phase transformation processes.

A formalism based upon dynamic elasticity has been developed which, in principle, provides us with a framework for deducing the stress drop tensor. Instrumentation to implement this approach has also been developed. A critical series of experiments are underway in which the stress drop tensor is to be measured using acoustic emission techniques and compared with that deduced by independent measurement or predicted from well developed theory.

The problem is that there are no available techniques for the measurement of stress drops when they occur at velocities close to that of the speed of sound. One possible approach we are following is to use reproducible cracking under indentation loading which is discussed below. However, another possible approach is the use of a simulated reproducible acoustic emission.

The ideal simulated source should be composed of dipole forces of similar magnitude and orientation to those of natural AE and have a time duration between 10 ns and 10 μ s (the range of the majority of natural emissions). These properties should be predictable and/or independently measureable. We have set up a laser generated thermoelastic simulated acoustic emission source for critically evaluating the performance of multichannel source characterization.

The thermoelastic dilatational strain accompanying absorption of pulsed laser radiation has been modelled as a combination of force dipoles

whose strengths were calculated using thermal diffusion theory. The temporal behavior of the elastic displacements due to each dipole component were then evaluated from the dynamic elastic Green's tensor for an isotropic infinite plate. The displacement waveform for the complete source was then obtained by linear superposition of the individual dipole responses.

The thermoelastic source generates longitudinal, transverse and surface waves. When calculations of displacement are performed on the same surface as the source, the waveforms are dominated by surface waves, particularly at large source to receiver distances. When calculations are made on the surface of the plate opposite the source, the transient displacement waveforms are dominated by head waves (critically reflected bulk waves). These latter waves have a non-unique ray speed and would lead to ambiguous source locations in acoustic emission monitoring.

A wide bandwidth system has been designed and constructed that can measure displacement with a sensitivity of $\sim 10^{-14}$ m over a 2.5 MHz bandwidth. This has been used to measure the displacement waveforms from the thermoelastic expansion accompanying the absorption of Nd:YAG laser pulses of 25 ns duration.

The measured waveforms contain the features predicted by theory and the dipole magnitudes are, within experimental error, in agreement with those predicted. From this encouraging basis we are proceeding to apply the deconvolution procedures developed above to deduce the full tensor description of the source stress change.

(3) Experimental method for the controlled generation of AE in A533B pressure vessel steel

An objective for the nuclear power industry has been the development of an experimental technique for localized production of reproducible AE signals (by indentation) in A533B pressure vessel steel and the correlation of these signals with the defects and microstructure at that location. These steels, while in the normalized condition are nonemissive, can become embrittled and emissive during fabrication into nuclear reactor pressure vessels by improper welding and heat treating practices (temper embrittlement) and can be further embrittled during service due to hydrogen, which is a fission product. Recently the NRC announced that eight of these vessels in service are becoming embrittled at a much faster rate than the original estimate and an expected 40 year lifetime will be reduced to a few years. It would seem that the above effects could contribute synergistically with the normally present radiation embrittlement and stress corrosion to reduce lifetimes.

By controlling the tempering and hydrogen charging in A533B we

succeeded in producing AE in the range from virtually none in the normalized condition up to an activity as high as that of borosilicate glass in the fully embrittled condition. We were further able to identify the sources of emission as microcrack nucleation (~ 5 micron) at MnS inclusions (Fig. 29) in the temper embrittled state and growth to larger grain boundary cracks (~ 250 micron) with the addition of hydrogen. A very significant result was the unexpectedly prominent role played by the MnS inclusions in the temper embrittlement process, as opposed to the usual attention given to segregated grain boundaries. This aspect is being followed up by work at Harwell.

(4) AE studies of rapid solidification

Rapid solidification is a new technique used for producing metallic glasses which provide low loss transformer core material. It is also used to produce superior surface coatings and long wearing bearing surfaces. AE can be used to monitor rapid solidification surface modification to detect flaws produced during processing. It also promises to provide dynamic information on the solidification process itself since a typical solidification time for a surface melt is on the order of 100 ms and stress waves can be monitored over considerable shorter times (~ 100 μ s). Very little work has been done in this area. However, due to the potential of AE to shed light on this subject, NBS and DARPA are sponsoring research on AE monitoring of rapid solidification processing.

Because of its commercial applications in welding and surface modification, the electron beam was used as a directed energy source for melting. A new technique has been developed for studying solidification of such melts. First it was verified that the signals were not electrical noise but were caused by material changes during solidification. The experimental approach consists in irradiating a spot on a plate, producing a steady state melt at 2×10^5 Wm^{-2} for qa (where q is the energy intensity and a is the source radius), switching off the electron beam to eliminate it as an AE source, then monitoring the amount of energy produced by AE during solidification.

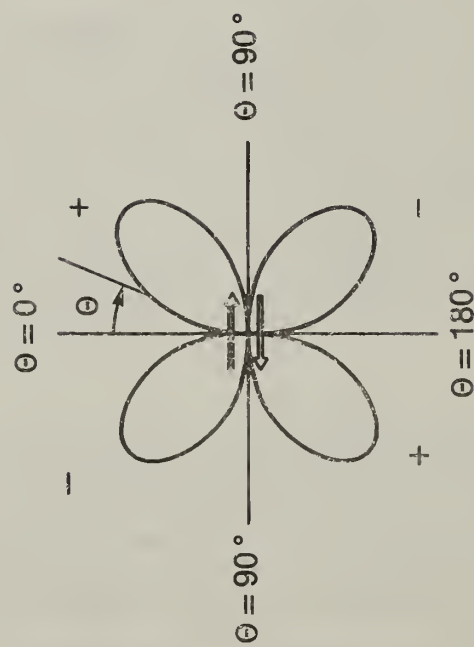
Our first results show the effects of alloying on resolidification AE. The resolidified melts in the 2219 aluminum alloy contained numerous cracks which indicate that hot tearing during solidification is the cause of the AE in the 2219 alloy (Fig. 30). In contrast, the 1100 aluminum resolidified melts had virtually no cracks (Fig. 31). This is reflected also in the amount of energy emitted acoustically during resolidification for the two materials (Fig. 32 and 33).

Results of this type are of great interest to the rapid solidification field. Once the sources of AE in rapid solidification are more fully ascertained, steps can be made to implement AE monitoring of surface

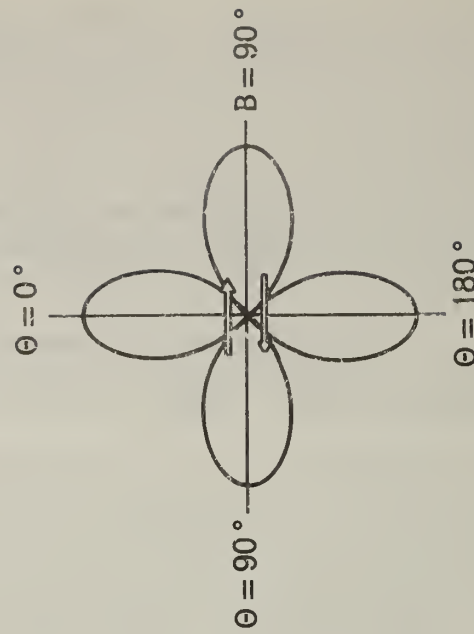
modification processes, and to dynamically observe the solidification process and its kinetics.

REFERENCES

- (1) J. A. Simmons and R. B. Clough, "Theory of Acoustic Emission," Dislocation Modelling of Physical Systems." Pergamon Press, 1981, p. 464.
- (2) J. Simmons and D. O'Leary, "A Bidiagonalization Regularization Procedure for Large Scale Discretizations of Ill-Posed Problems," SIAM J. Statistics and Computing, Dec. 1981.



(a) Longitudinal Component



(b) Transverse Component

Figure 20 Transverse component radiation pattern for a dislocation source.

Figure 19 Longitudinal component radiation pattern for a dislocation source.

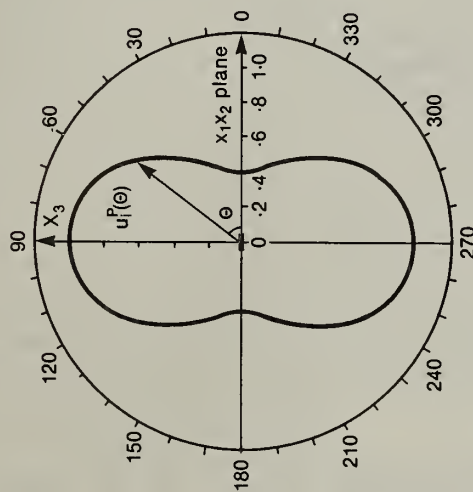


Figure 21 Longitudinal component radiation pattern for a microcrack source.

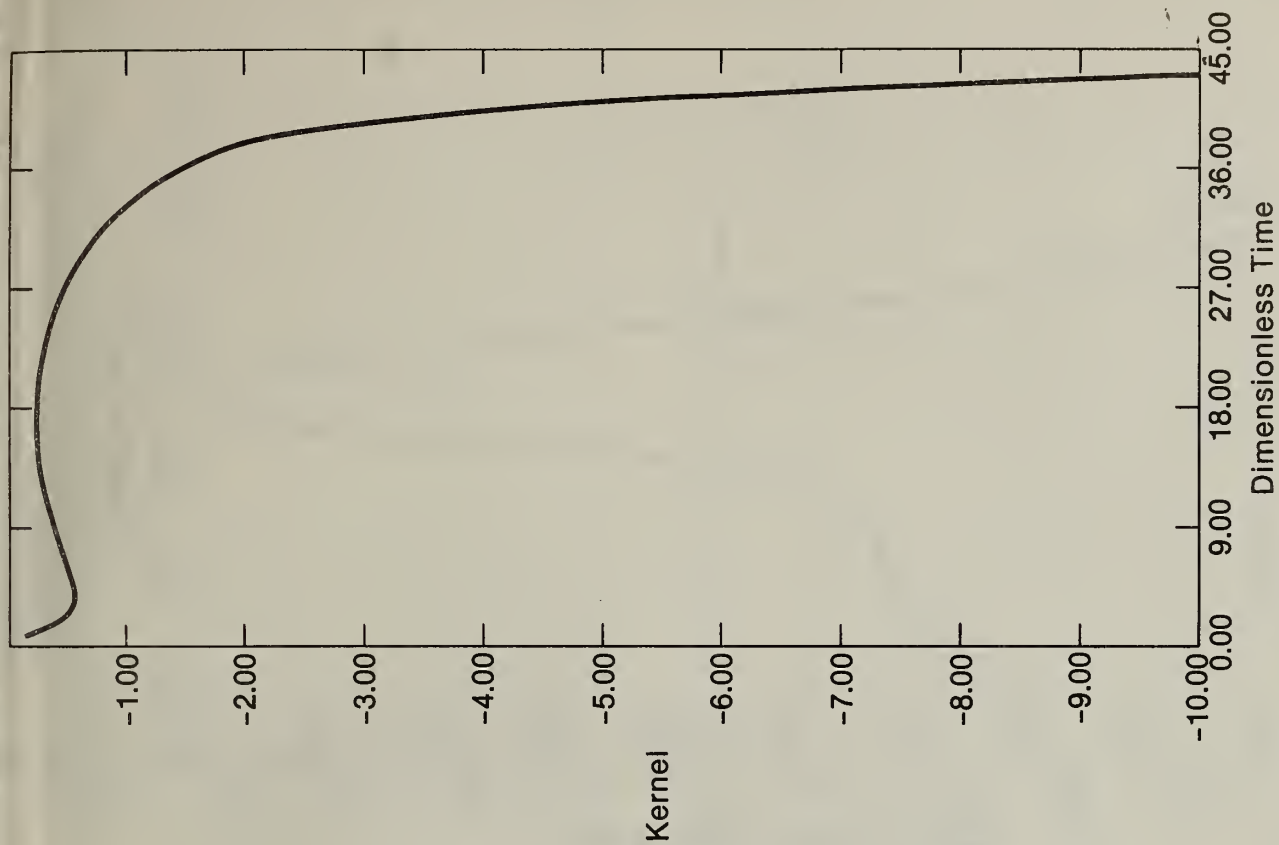


Figure 22 The beginning of the vertical response to a vertical force in a half-space with horizontal planar surface. This time series can be thought of as the kernel to be deconvolved out. This particular kernel is very ill-conditioned rendering deconvolution particularly difficult.

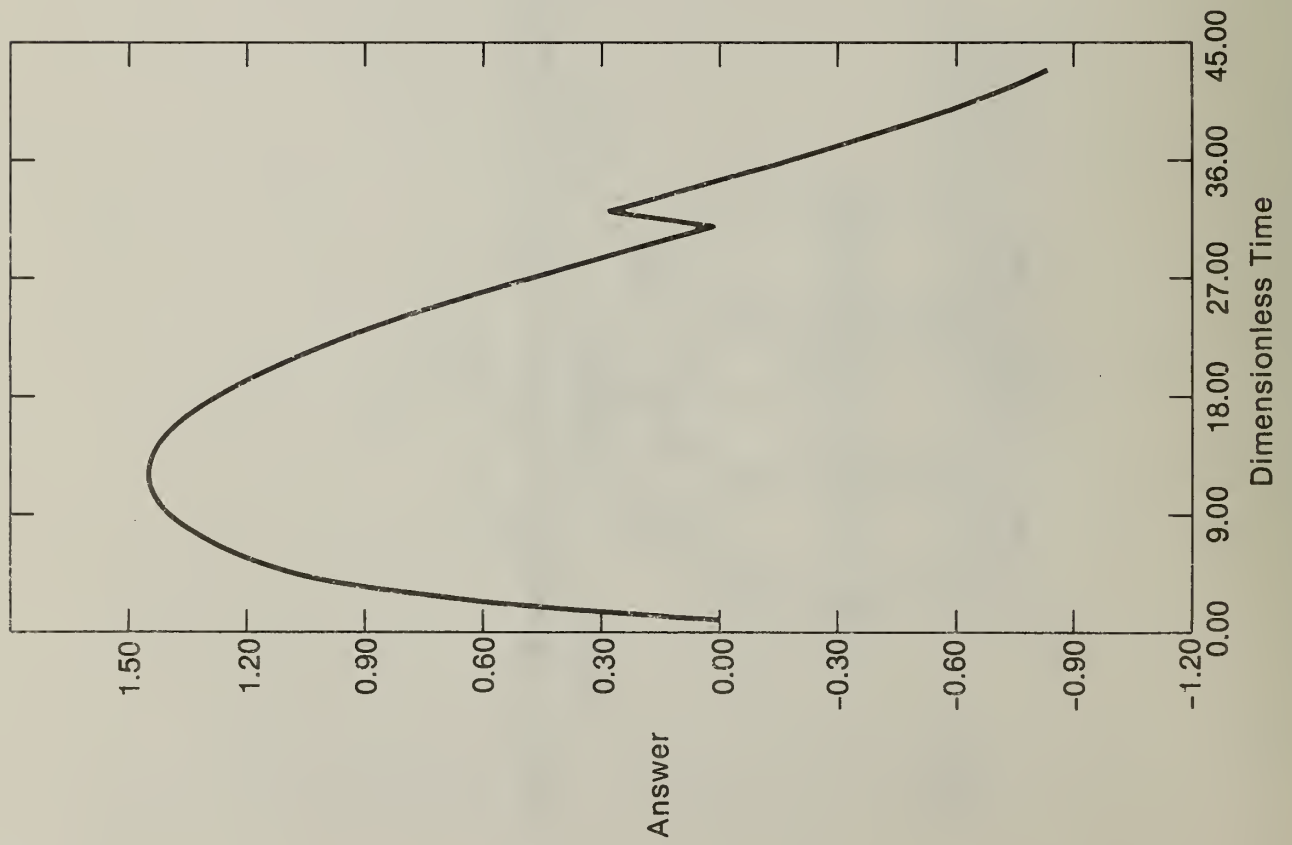


Figure 23. A hypothetical source curve. The 'answer' to be found.

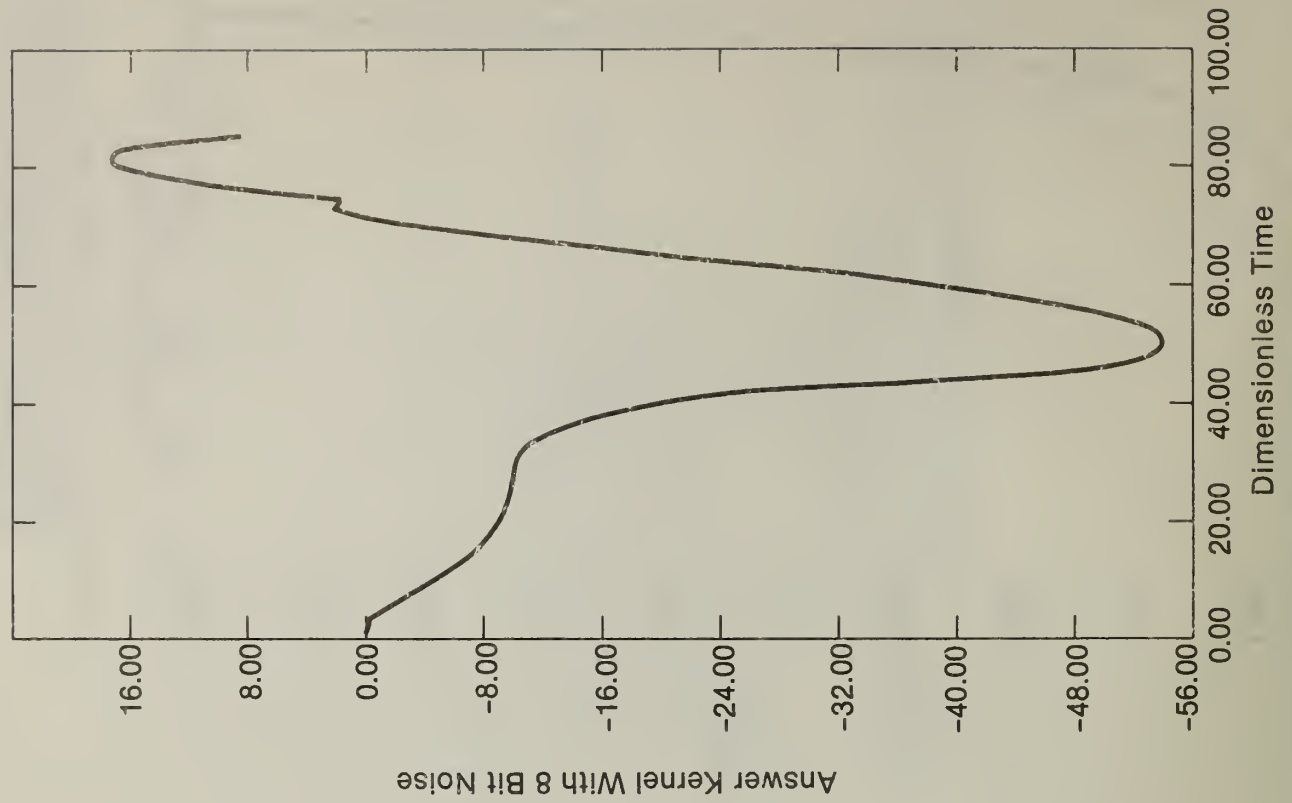


Figure 24. A hypothetical resulting output signal obtained from the convolution of the first two curves with 8 bit noise ($\pm 0.2\%$) added.

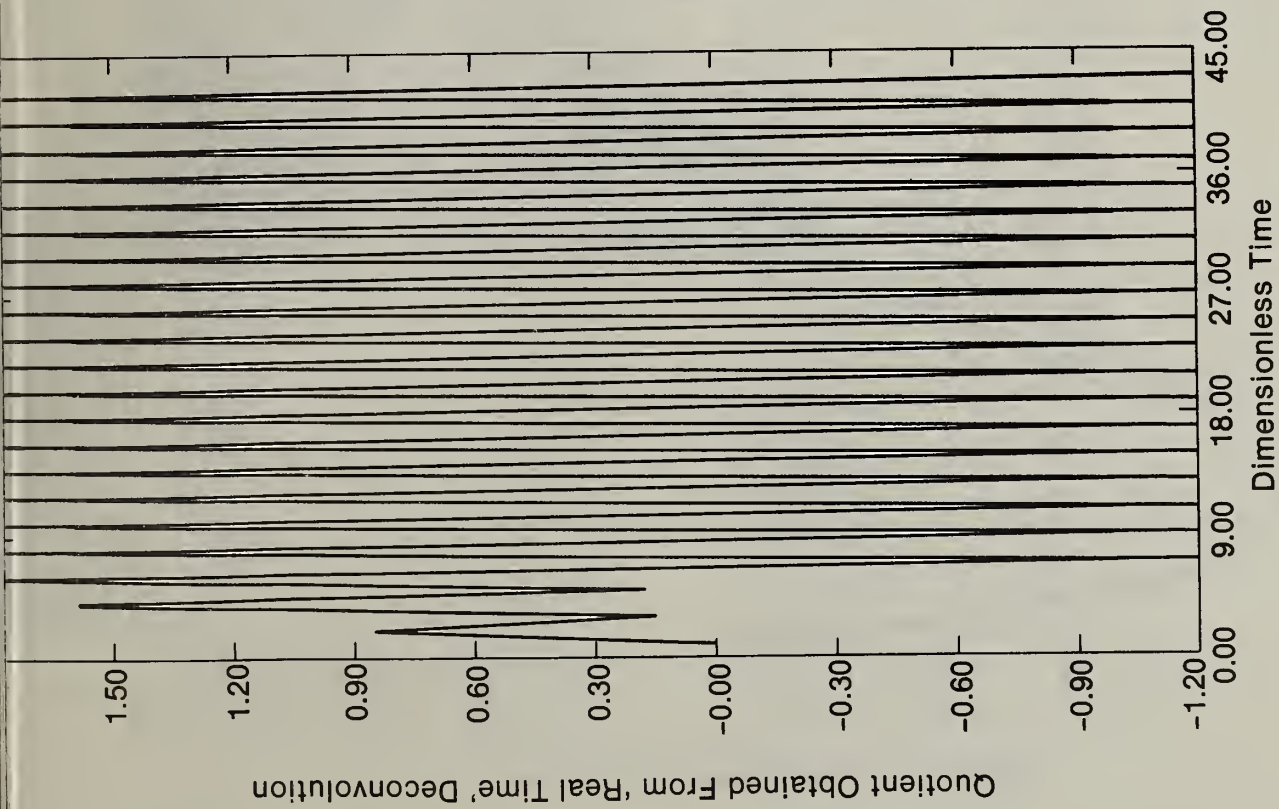


Figure 25. The approximation to the solution using 'real time' deconvolution which is simply the routine inversion of the convolution matrix as a lower diagonal matrix (compare with figure 23). Note: This curve oscillates between $\pm 10^5$.

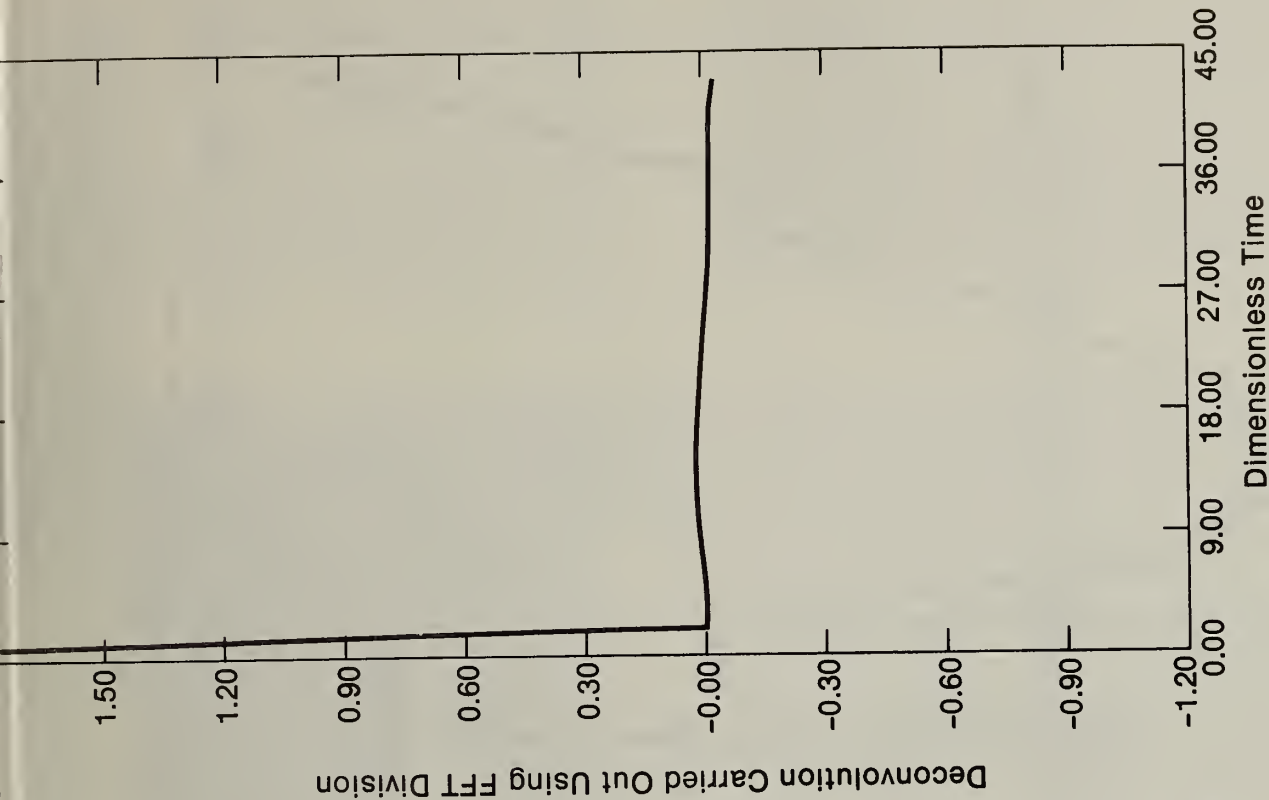


Figure 26. The approximation to the solution using division of the FFT of the output signal by the FFT of the kernel with 43 points of zero padding added to remove an obvious time aliasing error (compare with figure 23).

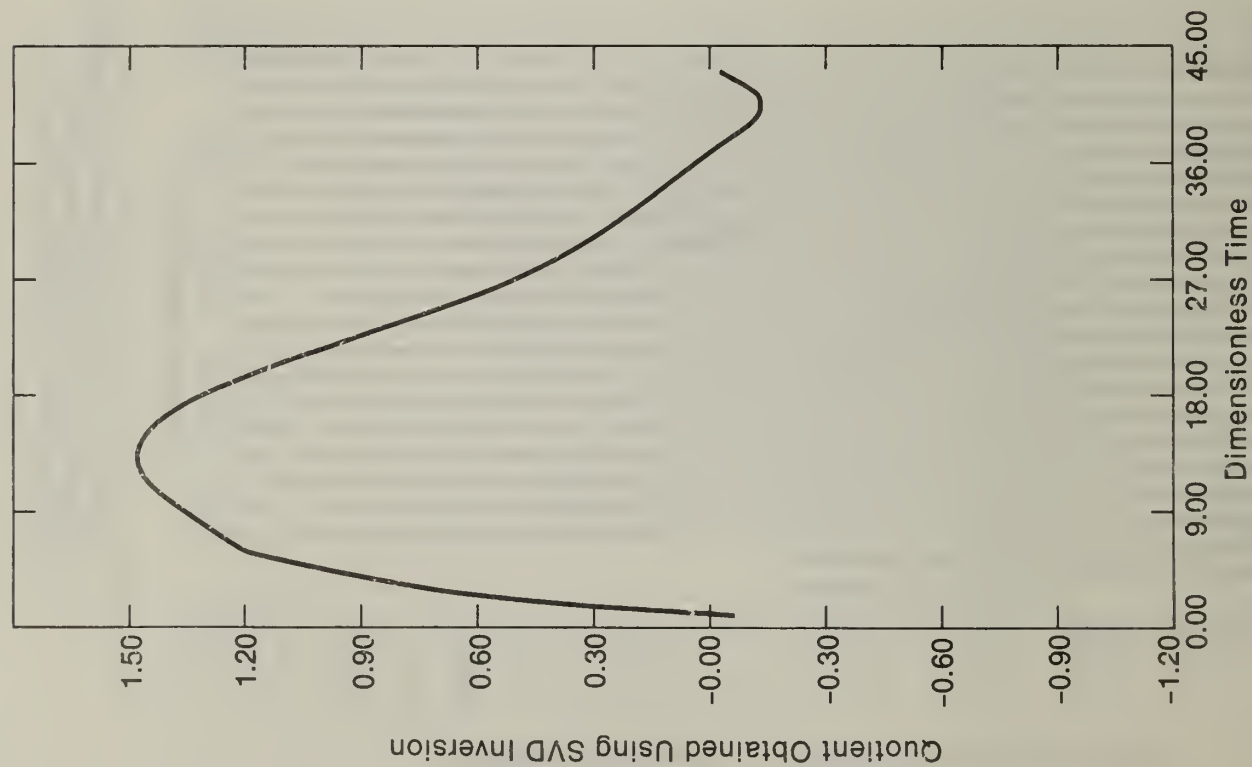


Figure 27. The 'best' approximation (in the sense of minimum error in the time domain) obtained from the SVD procedure (compare with figure 23). While obviously orders of magnitude better than the previous approximations, this approximation is in considerable error throughout the frequency domain.

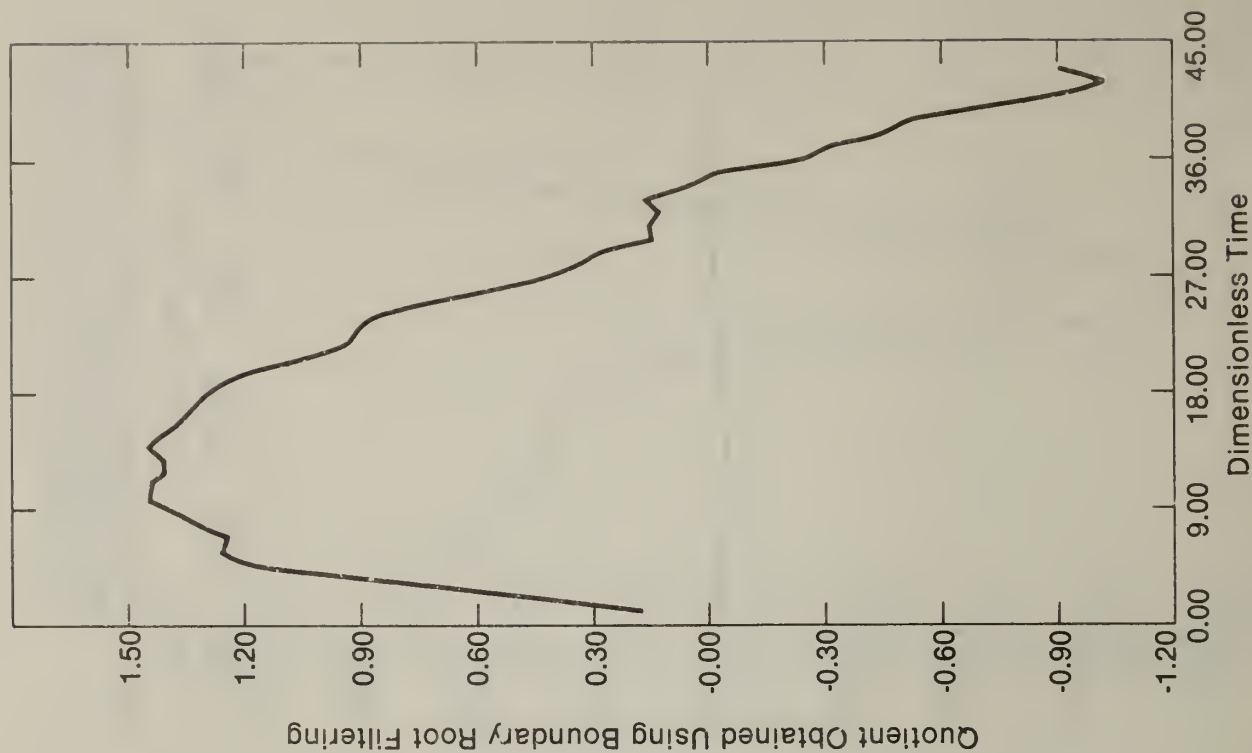


Figure 28. An approximation obtained using boundary-root filtering and radiused FFT deconvolution methods. This solution while appearing more 'jittery' than the preceding is actually more accurate in the frequency domain as well as giving a good approximation in the time domain (compare with figure 23).



Figure 29. Debonding of MnS inclusion due to indentation of uncharged, temper embrittled A533B.



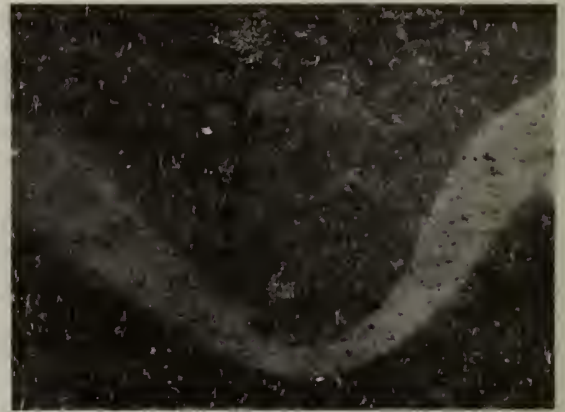
(a) $1.9 \times 10^5 \text{ Wm}^{-1}$



(b) $2.7 \times 10^5 \text{ ms}^{-1}$



(c) $3.3 \times 10^5 \text{ Wm}^{-1}$



(d) $4.1 \times 10^5 \text{ Wm}^{-1}$



(e) $5.7 \times 10^5 \text{ Wm}^{-1}$



(f) $6.4 \times 10^5 \text{ Wm}^{-1}$

0.5 mm

Figure 30. The effect of q_a upon melt profile and solidification microstructure of 2219 aluminum.



(a) $1.9 \times 10^5 \text{ Wm}^{-1}$



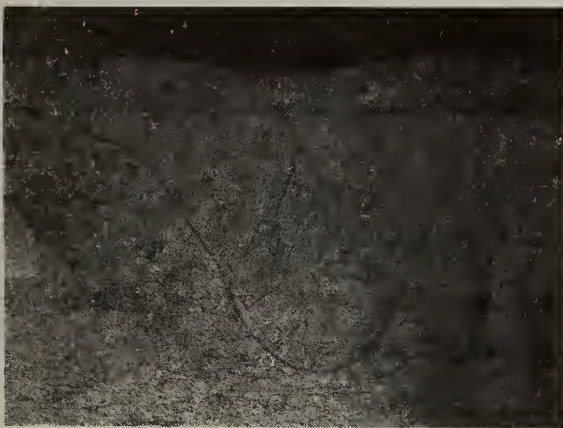
(b) $2.7 \times 10^5 \text{ ms}^{-1}$



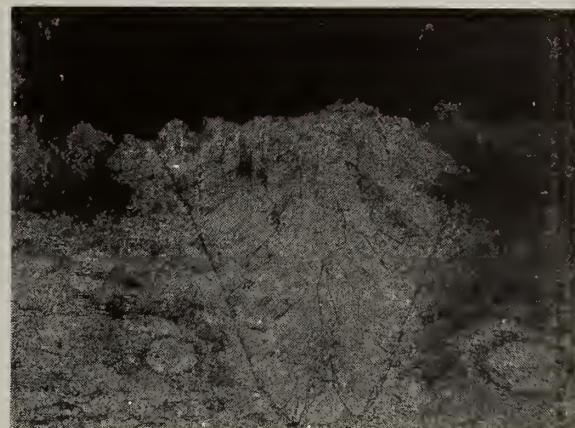
(c) $3.3 \times 10^5 \text{ Wm}^{-1}$



(d) $4.1 \times 10^5 \text{ Wm}^{-1}$



(e) $5.7 \times 10^5 \text{ Wm}^{-1}$



(f) $6.3 \times 10^5 \text{ Wm}^{-1}$

0.5 mm

Figure 31. The effect of q_a upon melt profile and solidification microstructure of 1100 aluminum.

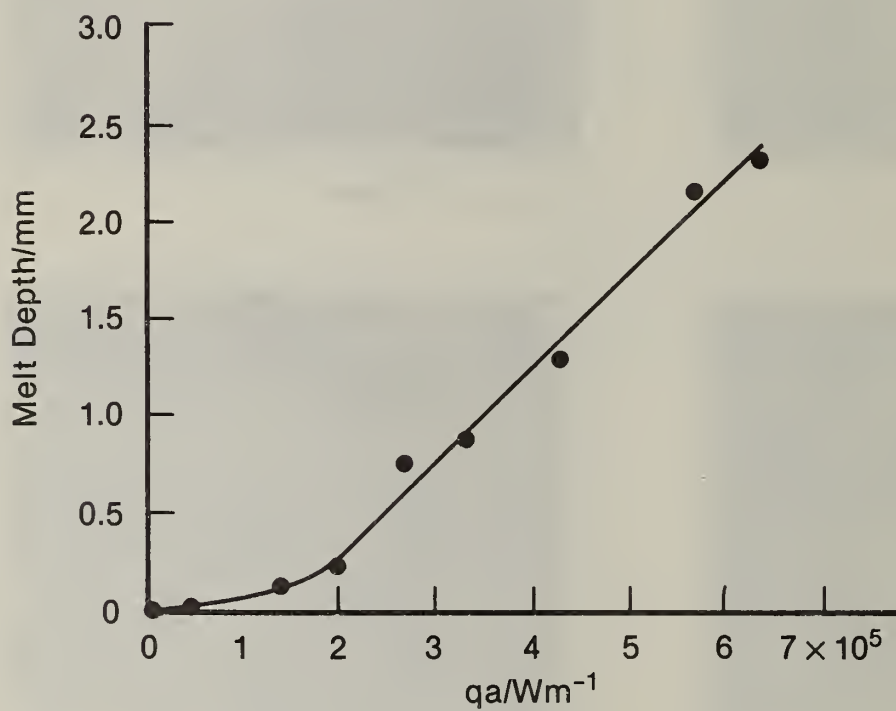
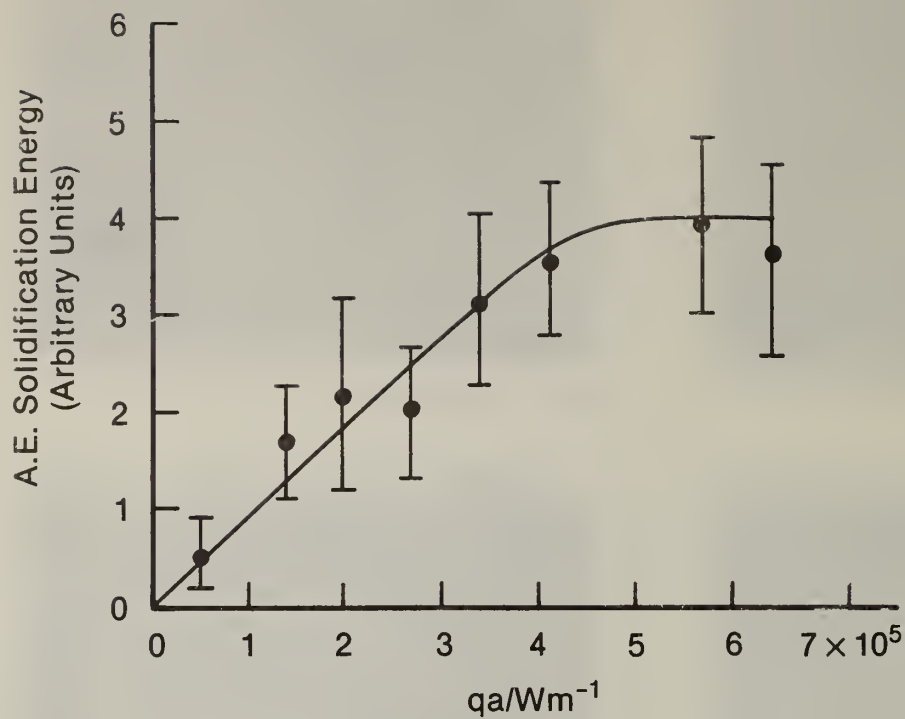


Figure 32. a) Acoustic emission energy emitted during solidification (energy has same arbitrary units as Figure 33a) and
b) Melt depth versus qa for 2219 aluminum.

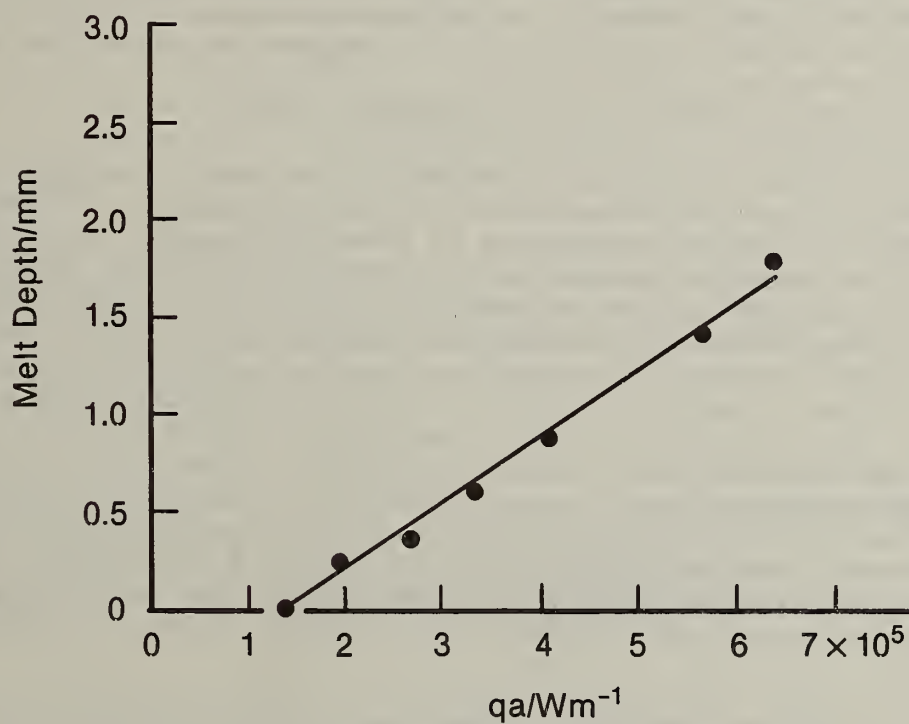
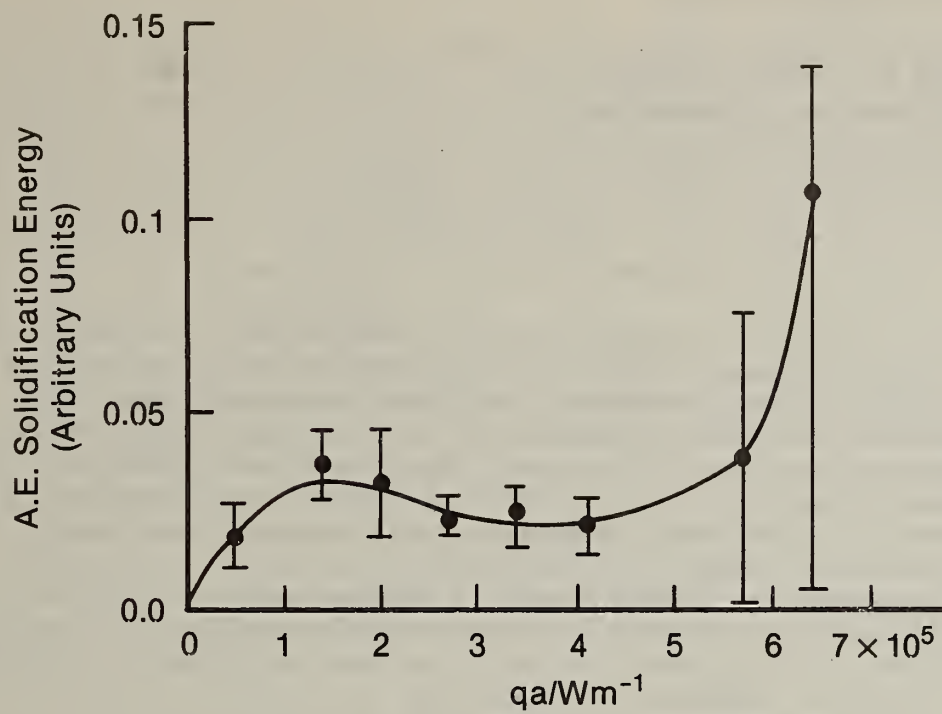


Figure 33. a) Acoustic emission energy emitted during solidification (energy has same arbitrary units as Figure 32a) and
b) Melt depth versus qa for 1100 aluminum.

ULTRASONIC TECHNIQUES FOR NDE

Melvin Linzer and Stephen Norton
Fracture and Deformation Division
Center for Materials Science

Introduction

Our work in the past year has emphasized the theoretical development of new ultrasonic imaging techniques: (1) A perturbation method to correct for ray refraction in velocity and attenuation tomography has been devised [1]. This work will allow the practical generation of more accurate images of ultrasonic parameters and hence better characterization of material properties; (2) A new imaging concept based on an annular aperture has also been developed [2]. Our approach provides a reflectivity image with resolving power equivalent to that of a full circular aperture twice the diameter of the annulus. This in turn permits more economical and rapid imaging over a smaller area of a material surface; (3) The first comprehensive and critical examination of techniques for measuring ultrasonic attenuation, velocity and scattering has been published [3]; (4) Our earlier work on a new sonic technique for detecting interrupted cutting during automated machining has been prepared and accepted for publication [4]; (5) Finally, a program has been initiated on the development of techniques to improve the sensitivity and accuracy of acoustic emission measurements. In the account that follows, we shall review the perturbation techniques for refraction corrections.

Review of Perturbation Technique for Refraction Corrections

The problem of reconstructing ultrasonic refractive index or attenuation images from ultrasonic transmission measurements is complicated by diffraction and refraction effects which are nonexistent in x-ray tomography. In ultrasonic "line-of-sight" or transmission tomography, a number of simplifying assumptions are customarily made for the sake of tractability. First, diffraction effects are ignored; this is equivalent to assuming that all but a negligible fraction of the propagating acoustic energy is confined to a ray connecting the transmitter and receiver. A second assumption is that this ray is a straight line, i.e., no refraction occurs. Under these conditions, the problem reduces to that of reconstructing an unknown function (e.g., refractive index or attenuation) from its path integrals over straight lines, for which numerous reconstruction algorithms may be applied. The failure to take into account diffraction (or scattering) and refraction effects will inevitably degrade the quality of a reconstructed image to an extent depending upon the properties of the medium under study, such as the characteristic scale (correlation distance) and magnitude of the inhomogeneities that compose it.

In the case of velocity tomography, techniques have been proposed for taking ray bending into account in an attempt to improve image quality. To date, all of these have been iterative in nature. A "first-order" reconstruction of a velocity (or refractive index) map is first obtained under the initial assumption that the propagation paths are straight lines. An approximation to the actual, or refracted, path is then computed from this map by numerically integrating the ray equation. At this stage, one strategy is to use a generalized algebraic reconstruction technique (ART) in which the path integrals of the parameter of interest (refractive index or absorption coefficient) are recomputed over the calculated ray trajectories. Then,

for a given path, the difference between the actual (measured) path integral and the computed path integral is uniformly distributed back over the ray path in the fashion of conventional ART (where of course the paths are straight). This process is performed for all ray paths, and the entire procedure iterated several times before convergence to an acceptable image results. If desired, further ray tracing can be carried out on the new image, and the entire process repeated using the latest estimate of the calculated ray paths. As in conventional ART, the ultimate objective of this approach is to force the computed path integrals to conform eventually to the measurements.

Although the above technique may be intuitively appealing, the computational times required may be unreasonably long because of its iterative nature and the need to compute a large number of ray trajectories at each iteration. Another approach to the ray-bending problem, due to McKinnon and Bates [5], exploits an iterative technique based on a simple rearrangement of the eikonal equation. This approach, which does not require numerical ray tracing, promises to be more efficient computationally than techniques that depend on integrating the ray equation at each iteration. However, many questions regarding the convergence of the various iterative schemes, including that proposed by McKinnon and Bates, remain largely unresolved and deserve further study.

The perturbation approach to the ray-bending problem, which we have developed in the past year, does not require iteration and also avoids the considerable computational cost of numerical ray tracing. As in the case of the other techniques, the perturbation approach begins with a first approximation to the velocity distribution obtained by reconstructing a refractive index map under the initial assumption that the rays are straight. The perturbation corrections are then derived on the basis of this first map. Our general approach may be described as follows. Suppose that the index of refraction deviates from its average value (normalized to one for convenience) by an amount on the order of ϵ , where $\epsilon \ll 1$. Using the initial estimate of the refractive index, we derive an expression for the ray path whose departure from the straight line joining the transmitter and receiver is first order in the small quantity ϵ . This "first-order" path (or ray) closely approximates the true path when ϵ is small. The expression for this path is then used to obtain a number of useful perturbation corrections applicable to both velocity (or refractive index) and attenuation tomography.

In all methods that correct for refraction, the ray path must be computed to begin at the transmitter and end at the receiver. The perturbation approach has the significant advantage of solving this boundary value problem automatically. For techniques that rely on numerical ray tracing, the integration of the ray equation is inherently an initial value problem, i.e., the initial direction of the ray path at the source must be specified to get the ray tracing process underway. The initial conditions--the source location and the initial ray direction--define a unique path that may or may not intercept the desired receive point. This problem is typically solved by iteratively adjusting the starting direction of the ray in an attempt to make the ray intercept the receiver. In the perturbation approach, the ray trajectory is defined once the source and receive points, rather than the source point and the initial ray direction, are specified. This feature avoids the exceedingly time-consuming process of computing multiple rays with different initial conditions in an attempt to find one that coincides with the desired boundary

conditions.

The first correction we have considered is the time-delay error that results when refraction is ignored in a time-of-flight measurement. It is shown that variations in the time-of-flight over a straight (unrefracted) path between two points are first order in ϵ . In other words, the time delay of a pulse propagating along a straight line may be regarded as a simple retardation, or "longitudinal" delay, along the path; variations in this "straight-line" delay are first order in ϵ . If the ray is now permitted to deviate from the straight line due to refraction, but is constrained to pass through the same transmit-receive points, the original (straight-line) time-of-flight value will change by an amount of order ϵ^2 due to ray refraction. An explicit formula for this second-order correction, as well as for the first-order ray path, has been derived.

The time-delay correction that arises due to ray bending can be used to modify time-of-flight data over refracted paths as follows. For a given path-integral measurement over a refracted ray, the computed correction term is subtracted from this value to yield a modified value that is more nearly equal to the path integral of the unknown refractive index over the straight line joining the transmitter and receiver. After all of the measurements are modified in this manner, the resulting "corrected data" are submitted to a conventional straight-line reconstruction algorithm. The result is a reconstruction less degraded by time-delay errors arising from refraction.

The first-order ray path and the time-delay correction were derived for both two and three dimensional refraction. In conventional ray-tracing methods, the computer time required to calculate large numbers of ray paths in three dimensions may be so great as to render such schemes computationally impractical, at least in an industrial setting.

Different types of measurement uncertainties that result from using transducers of finite size have also been analyzed. In a time-of-flight measurement, a finite-aperture receiver or transmitter introduces an uncertainty in the arrival time. In addition, an attenuation measurement employing an extended, phase-sensitive receiver is subject to errors because of phase cancellation and beam displacement. Using the first-order ray path which we have derived, an estimate of the maximum value of the arrival-time is also computed. Estimates of the attenuation errors are also obtained, which, in principle, may be exploited to correct for phase-cancellation and beam-displacement effects. Computer-simulated reconstructions were obtained with and without the time-delay correction. The simulations show clearly an improvement, at least for the simple examples considered.

Conclusion

The perturbation technique described above is a continuation of our efforts over the past few years to solve some of the fundamental theoretical problems in ultrasonic imaging. Previous work in this program includes a comprehensive analysis of backprojection techniques for reflectivity imaging [6,7] and the first inverse scattering solution of the wideband pulse-echo imaging problem [8]. Future work will extend our results on backprojection and inverse scattering approaches in ultrasound to the acoustic emission area.

References

- (1) Stephen J. Norton and Melvin Linzer, "Correcting for Ray Refraction in Velocity and Attenuation Tomography: A Perturbation Approach, " Ultrasonic Imaging 4, 201-233 (1982).
- (2) Stephen J. Norton, "Acoustical Holography with an Annular Aperture," J. Acoust. Soc. Am. 71, 1169-1178 (1982).
- (3) Melvin Linzer and Stephen J. Norton, "Ultrasonic Tissue Characterization," Ann. Rev. Biophys. Bioeng. 11, 303-329 (1982).
- (4) F. P. Higgins and M. Linzer, "Sonic Technique for Detecting Interrupted Cutting During Automated Machining," J. Eng. Ind. (submitted).
- (5) G. C. McKinnon and R. H. T. Bates, "A Limitation on Ultrasonic Transmission Tomography," Ultrasonic Imaging 2, 48-54 (1980).
- (6) Stephen J. Norton and Melvin Linzer, "Ultrasonic Reflectivity Tomography: Reconstruction with Circular Transducer Arrays," Ultrasonic Imaging 1, 154-184 (1979).
- (7) Stephen J. Norton and Melvin Linzer, "Ultrasonic Reflectivity Imaging in Three Dimensions: Reconstruction with Spherical Transducer Arrays," Ultrasonic Imaging 1, 210-231 (1979).
- (8) Stephen J. Norton and Melvin Linzer, "Ultrasonic Reflectivity Imaging in Three Dimensions: Exact Inverse Scattering Solutions for Plane, Cylindrical, and Spherical Apertures," IEEE Trans. Biomed. Eng. BME-28, 202-220 (1981).

TRANSFER STANDARDS FOR ULTRASONIC POWER MEASUREMENTS

Frank Breckenridge, Steve Fick and Carl Tschiegg
Mechanical Production Metrology Division
Center for Manufacturing Engineering

The rapid growth in medical applications of ultrasound has fostered an increased demand for means by which the total radiated power of medical ultrasonic transducers can be accurately determined. In addition to its calibration service for user-supplied transducers, NBS has for some time offered the loan of custom-built transfer standard transducers. A new type of transducer has been designed both to improve overall performance and to preclude certain difficulties now known to be commonplace in field use. This unit will soon be available for purchase through the Office of Standard Reference Materials.

The newly-designed standard source is used as a transfer standard for measurements of the total radiated power sources operating into liquid media at power levels from 0.1 mW to 1 W in the frequency range of 1-10 MHz. It utilizes a compliantly-mounted piezoelectric crystal in a cylindrical stainless-steel housing which also contains circuitry to sample the applied rf voltage. An impedance matching network provided with each transducer relieves drive requirements by allowing the use of a 50 ohm rf source. Embodied in the matching network is the additional circuitry necessary to allow the accurate measurement of rf voltage independent of cable effects which have been found to significantly degrade the accuracy of such measurements in the field. Based on preliminary tests, the use of compliant adhesives to mount the piezoelectric element will offer improved performance by providing greater acoustical isolation, reducing mechanical stresses, and promoting long-term stability of the transducer radiation pattern. Research involving the new standard source now includes a study of the feasibility of a "universal source" capable of useful operation at high-order overtones. Initial results indicate that the successful implementation of such a transducer is likely.

IMPROVED ULTRASONIC REFERENCE BLOCKS

Gerald Blessing and Donald Eitzen
Mechanical Production Metrology Division
Center for Manufacturing Engineering

The National Bureau of Standards has been asked by the Army Mechanics and Materials Research Center of the Department of Defense to evaluate the present procedures for fabricating and testing aluminum alloy ultrasonic standard reference blocks, and to make recommendations for improving those procedures (1). These reference blocks, possessing flat-bottom-hole defect artifacts, are used both for calibration and as reference standards. Here we outline our recommendations for their improvement.

Many sets of aluminum ultrasonic reference blocks have been fabricated according to the specifications in the ASTM E 127 document, "Standard Practice For Fabricating and Checking Aluminum Alloy Ultrasonic Standard Reference Blocks". It is DoD's goal to reduce the present allowable tolerance of +2 and -3 dB criteria of E 127 to +1 dB, for its own applications. We note that recommending changes to the ASTM document is not part of this task; rather, that document serves as a baseline from which to work.

The +1 dB goal represents a substantial reduction in tolerance, and would impact on all phases of the manufacturing and calibration of reference blocks. The principal system variables affected may be categorized per reference (1) as follows:

1. Block Material
2. Transducer
3. Pulser/Receiver
4. Operator Judgment
5. Block Geometry

A +1 dB tolerance means that the net effect of these system variables be +12 percent or less.

Guided by these constraints, the following are judgments of the optimum tolerance for each system variable; these tolerances are considered feasible with present technology.

1. Block Material: The recommended approach is first to define a (arbitrary) level of material ultrasonic scattering that is typical of today's manufacturing process, and which also meets the requirements of E 127. Secondly, require that the variation in material scattering as determined by the echo amplitude on the largest block length, not exceed +5 percent. (A three-measurement average should be obtained for each block.) This may require that all bar material be taken from the same manufacturing lot and/or other restrictions be placed on its fabrication. Hopefully, an effective screening of acceptable material can be achieved by sampling. The figure of -5 percent represents an educated guess of present feasibility.

2. Transducer: The ability of manufacturers to fabricate like transducers or search units has been very limited. While the best results have been obtained using quartz, even these transducers show appreciable variation in performance. However, some success has been achieved in correcting their acoustical far-field profile variations, which is the region of significance in calibration work. Based on empirical results using correction factors, a figure of \pm percent variation in block response may be ascribed for quartz transducer variations.
3. Pulser/Receiver: Variations in tuned pulse width may significantly affect the echo amplitude from a given block. It is not clear how this variable should be controlled, except that it should at least be kept constant for a given system. Variations between like systems will certainly be minimized by using the same pulse width, and as much as possible, the same pulse shape (and therefore, spectral content). Receiver linearity of ± 2 percent or better may be realized with available solid state circuitry. This, combined with uncertain pulser variations, contributes approximately a ± 5 percent variation to the ultrasonic system.
4. Operator: By eliminating screen reading judgment errors with digital readout of signal amplitude, the principal operator-dependent variations would be limited to alignment errors. These should be kept within a ± 2 percent bound. The detection of bubbles, a potential source of large error, on the transducer and/or block surface is greatly facilitated by back-lighting an immersion tank constructed with transparent siding. Finally, to minimize operator-dependent errors, all reported amplitude values should be an average of three repeated measurements; and a difference of more than 2 percent within these three measurements should be investigated.
5. Block Geometry: So long as reference blocks are fabricated by hole drilling, possible variations of ± 3 percent in echo amplitude due to this process will have to be allowed for the smallest diameter - No. 3 size hole. Variations in the larger holes (No. 5 and No. 8) will be proportionally smaller.

Finally, there is a source of systematic or "system offset" error as E 127 is presently written. There is a discrepancy between metal ball diameters, used to set system sensitivity, and the hole size ratios. This discrepancy must be eliminated in order to use the same table of recommended echo amplitude values for all hole sizes.

In conclusion, we note that the net tolerance outlined above appreciably exceeds our ± 12 percent (or 1 dB) goal if we assume the worst case conditions. Eliminating this excess of tolerance would impose more stringent requirements on the material properties, the transducer, and the pulser. Both the use of correction factors and the establishment of a central calibration facility could serve to alleviate these additional requirements.

- (1) Blessing, G.V. and Eitzen, D.G., "Ultrasonic Standard Reference Blocks - What Future?" Summary Papers of the Spring and Fall, 1982 ASNT Conferences (to be published).

NDE TERMS AND DEFINITIONS: ULTRASONICS

Donald Eitzen and Marilyn Cadoff
Mechanical Production Metrology Division
Center for Manufacturing Engineering

The Army Materials and Mechanics Research Center has asked that NBS assist them in developing terms and definitions suitable for use in Mil Standards. The specific objectives of the current phase of this activity are to:

1. Develop appropriate terminology for the broad NDTI primary terms including: Nondestructive Testing, Nondestructive Inspection, Nondestructive Evaluation and Nondestructive Examination.
2. Develop appropriate terminology for some of the general terms associated with nondestructive methods including: Reference Standards, Calibration Standards, Reference Blocks, and Calibration Blocks. The metrological use and implications of these terms will be taken into account in this terminology.
3. Develop appropriate and precise terminology for ultrasonic test methods and procedures using resources such as ASNT, ASTM, ASME and military publications with definitions of ultrasonic terms. Also, identify terms that are necessary but not yet defined.
4. Develop additional general terms associated with nondestructive methods. The metrological use and implications of these terms will be taken into account. Also, develop precise terminology for those specific terms for ultrasonic methods identified earlier as needing definition.

In carrying out these tasks well over 30 draft or published documents were reviewed and competing terms and definitions were organized. A number of internal workshops were conducted with NBS experts on metrology and on NDE. As a result, four terms were proposed for the broad NDE primary terminology such as "Nondestructive Testing". General terms such as "reference standards" were studied and, as a result, 28 general terms were proposed. Also 115 terms were proposed for ultrasonic test methods. This phase of the project is essentially complete; however, additional editing of some terms will be undertaken in order to maintain consistency between this effort and some recent NBS comments on proposed MIL-STD-1309C, "Definition of Terms for Test, Measurement and Diagnostic Equipment".

CONTACTLESS LASER GENERATION AND OPTICAL INTERFEROMETRIC
DETECTION OF ULTRASONIC WAVES

M. Rosen, S. Fick, F. Nadeau and R. Mehrabian

Metallurgy Division

Center for Materials Science

Transient loads applied by rapid energy transfer from a single-pulse Q-switched high-energy laser generate compressive stress waves that propagate in a material. Propagation of ultrasonic waves in a medium cause surface displacements that can be measured optically by exploiting the phase shift of an optical beam reflected from the surface of the material. When the reflected beam is approximately combined with a reference optical beam, from a helium-neon laser, phase changes are converted into amplitude changes, detectable by a suitable photodiode. These amplitude changes are proportional to the surface displacements on the specimen. Potential problems arising from the fact that phase changes also result from relative motion among the optical components of the system and even from fluctuations of the ambient air, are avoided by appropriate features in the mechanical design of an interferometer. An arrangement due to Fizeau is inherently compact and mechanically stable, and thus well-suited to the present application. Two such Fizeau interferometers can readily be combined so that the two optical probes may be separated by a convenient distance to allow accurate measurement of the travel time of an ultrasonic wave in the specimen over a well-defined distance. Furthermore, the variation in magnitude of the surface displacements detected by the two Fizeau interferometers determines the ultrasonic attenuation in the specimen. This specific system with dual Fizeau interferometers allows the simultaneous determination of both elastic-wave velocity and ultrasonic attenuation.

Compared with other sensors, interferometers offer several advantages. The sensitive area is definite, and can be made as small as a few microns in diameter for highly localized measurements. A known quantity, displacement, is measured; independent methods of absolute calibration are applicable which give small overall errors. Bandwidth, determining the fidelity of reproduction of signal waveshapes, is limited not by the physical nature of the transduction process but by its associated electronics. In this respect, performance can exceed that of conventional piezoelectric transducers. Small signal resolution and bandwidth are related; displacements of a few Å are detectable at 7 MHz bandwidth. Laser loading produces a stress pulse of high amplitude and short duration so that investigation of highly attenuating, or very thin, specimens is possible. The noncontact feature of both generation and detection of ultrasonic waves is advantageous in situations requiring physical separation between the measuring system and the specimen. Furthermore, the noncontact mode of generation and detection precludes interaction with, and modification of, the wave propagation under study.

The two-channel, quadrature dual-laser interferometer developed and constructed permits highly accurate sound wave velocity measurements of longitudinal, transverse and Rayleigh waves. From the absolute surface displacement measurements, it is possible to determine the values of the attenuation of these waves, as well as their frequency dependence.

The contactless method of generation and detection of ultrasonic waves permits dynamic measurements to be performed whereby the specimen is subjected to programmed heat treatments, or is positioned in a hostile atmosphere. The noncontact mode of generation and detection precludes interaction or modification of the wave propagation under investigation. This unique dual-channel laser interferometer is in the process of final adjustment and calibration.

EDDY CURRENT STANDARDS

A. J. McAlister

Metallurgy Division

Center for Materials Science

The eddy current method is widely used in both the ferrous and non-ferrous metals industries for nondestructive detection of flaws such as cracks, inclusions, and variations in composition and microstructure in metals and metal parts via local changes in electrical conductivity. Primary conductivity standards are needed for reliable execution of this work, but to date this need has been supplied by industry itself. The necessary range of conductivity for industrial testing is from 5.85 to 58.5 MSm^{-1} (1 to 100 percent IACS).

The properties desired in a primary conductivity standards are long term stability, durability, and low magnetic susceptibility. (In testing of high susceptibility steels, normal practice has been to apply a saturating magnetic field to reduce the differential permeability to a value near that of vacuum). Hence, elemental metals and alloys of equilibrium phase composition upon which stable nonconducting surface layers can be formed are desirable. The surface properties are important not only for durability, but for reproducible lift-off behavior as well.

Our overall aim is the selection of metals and alloys suitable for primary conductivity reference standards, and the preparation of specifications for their preparation and fabrication. Progress to date in this work is summarized in the following Table, in which target conductivity material,

Summary of Conductivity Testing

Target Conductivity (% IACS)	Material (w/o)	Status	Condition	Observed Conductivity and range (% IACS)
101	OFHC Cu	*	annealed	101.9 \pm 0.1
		*	unannealed	99.5 \pm 0.2
85	1.3 Zn + Cu	#	as cast	81.1 \pm 0.4
75	2.4 Zn + Cu	#	as cast	70.4 \pm 0.4
60	Al 1100F	+	complete	60.0 \pm 0.05
48	Al 2024-0	+	complete	47.0 \pm 0.1
41.5	Al 6061-T	+	complete	41.0 \pm 0.05
29	Al 2024-T-351	+	complete	30.0 \pm 0.1
23	21.5 Zn, 2.5 Al + Cu	#	as cast	20.5 \pm 0.3
17	7 Al + Cu	#	as cast	15.6 \pm 0.1
17	6 Ni + Cu	*	as received	17.7 \pm 0.1
12	1.5 Si + Cu	#	as cast	10.1 \pm 0.2
7	3 Si + Cu	#	as cast	7.5 \pm 0.2
7	23 Ni + Cu	*	as received	6.11 \pm 0.01
3.5	Ti, Grade 4	*	unannealed	1.95 \pm 0.05
3.5	45 Ni + Cu	*	as received	3.440 \pm 0.002
1.0	8 Al, 1 Mo, IV + Ti	*	unannealed	1.07 \pm 0.007
1.0	6 Al, 4 V + Ti	*	unannealed	0.86 \pm 0.012
				0.97 \pm 0.005

Status is indicated as:

+, finished, calibrated standards;

*, commercial products, faced and examined;

#, alloys cast in-house, faced and examined.

Production and calibration of the Al-based standards is complete.

condition of the material as examined, observed conductivity and its extreme variation over the sample faces, and status of the material are listed.

Apparent conductivity variation over the surfaces of commercial alloys appears random, and is taken to reflect the variation to be expected in as-received condition. The better uniformity of annealed vs. unannealed Cu is due to removal of cold work damage. Annealing did not improve Ti or the Ti-based alloys. The major part of the conductivity variation in the as cast Cu-based alloys is due to solute segregation upon solidification, and should be largely removed by homogenization.

The decision to focus on Cu-based alloys outside the Al and Ti ranges, and to prepare special melts, was not made lightly. As a practical matter, it is essential that the magnetic permeability of an eddy current conductivity standard be very close to the vacuum value. Only Cu-based alloys are potentially capable of meeting this criterion in the needed conductivity ranges. Special melts are indicated because current industrial practice is to add significant quantities of Fe, Co, and Mn (which can develop full magnetic moments or form magnetic precipitates in Cu) as grain refiners or to improve mechanical properties. Currently available Si-bronzes contain 0.8 w/o Fe; Cu pro-nickels, 1.0 w/o Fe; brasses, 0.05% Fe. Yet the brasses, for example, must contain less than 0.03% Fe if Fe precipitation is to be avoided during stress relief.

In view of the importance of the magnetic properties, we have assembled and tested equipment for the measurement of magnetic susceptibility by the Gouy method. We are currently acting to provide sets of 100 coupons each of OFHC Cu and Ti-6-4 alloy.

EDDY-CURRENT TESTING

George Free

Electrical Measurements and Standards Division

Center for Absolute Physical Quantities

The initial phase of the eddy-current project to make available to the general public electrical-conductivity Standards Reference Materials (SRM's) has been completed and three primary standards have been calibrated. The resistivities of four electrical-conductivity SRM's have been determined in terms of these three NBS primary standards. The four values of electrical conductivity cover range 30-60% International Annealed Copper Standard (IACS) and specifically include SRM's with conductivities of 31, 41, 47 and 61% IACS.

The experiment to determine the resistivity of the primary standard was discussed in the 1981 Annual Report. In an effort to lower the uncertainty of this measurement, two steps were taken during FY82. First, the length of the primary standards was reduced to approximately 48.5 cm. The reduction in length makes possible more accurate machining methods, thereby improving the accuracy and precision of the cross-sectional area determination. Second, the dc experiment was modified by constructing a new bar holder and a potential contact assembly. In the new system bar temperature was monitored more closely and the potential contacts were fixed with respect to each other with an approximate separation of 5.08 cm. Furthermore, the contacts can be moved across or along the bar to measure variations of resistance over the area of interest. At the time of writing, this experimental arrangement was still being tested for precision and accuracy. The dc bridge had also been improved by replacing all critical switches with low thermal switches. This has reduced the noise in the detector by a factor of 2.

The eddy-current bridge used for comparing the NBS primary standards with unknown samples was and still is being improved. The basic design is discussed in the 1981 Report but additional electronics have been developed for the grounding network in order to improve bridge accuracy and for reducing the time needed for measurements. The oil bath has been rebuilt and a secondary control bath has been added to improve temperature stability and make possible a controlled variable-temperature bath. Coil holders have been redesigned to minimize coil heating on metal. A new lift-off device has been designed and its components are being constructed. The new device will make possible more accurate measurements of coil-metal separation. This data will become part of the computer algorithm used to calculate conductivity from measurement data.

A scanner that moves across the test sample with only minor variations in lift-off was constructed for the eddy-current experiment. With this scanner, highly accurate measurements of conductivity variation in a given sample can be made.

During the year conductivity standards were calibrated for Kaiser Aluminum and for the Aluminum Association. These calibrations served as a trial run for the NBS calibration facility.

A paper entitled "Standards for Eddy-Current Nondestructive Testing," was coauthored with G. Birnbaum and H. Berger of NBS and V.V. Kljuev and Y. Fedosenko of the USSR and was presented at the 10th World Conference on Non-Destructive Testing. This paper discusses some ASTM Eddy-Current Standards and compares them with their Russian counterparts.

Several new activities are planned for FY83. Theoretical studies will be initiated on at least two problems related to the methodology presently used in the calibration of conductivity standards. First, a study of the shortest possible distance between point of entrance of the dc current and placement of the potential contacts will be made. The largest component of uncertainty in the primary reference bars is due to the determination of cross-sectional area. Shorter bars can be machined and measured more accurately. Thus, the minimum length for the reference standards is an important quantity. The second problem is to correlate coil impedance changes with sample geometry. More specifically, the relationship of coil impedance to coil distance from the sample edge is known only by experiment. A theoretical model of this problem would aid in the optimum design of coils.

During FY83 some modifications will be made to both the ac and dc measurement systems in an attempt to further reduce the uncertainty of the measurements. Various aluminum and brass bars will be tested for electrical uniformity in a continuing effort to improve the electrical characteristics of the NBS primary standards. A second set of 400 samples in the 30-60% IACS range will be purchased and calibrated as SRM's. Also samples with nominal values of 100 and 1% IACS may be obtained and calibrated as SRM's in FY83. The NBS measurement system will be documented and a technical note written discussing the entire experiment.

HIGH FREQUENCY, BROADBAND EDDY CURRENT PROBES FOR IMPROVED FLAW CHARACTERIZATION

C. M. Fortunko and S. A. Padget
Fracture and Deformation Division
Center for Materials Science

Recent theoretical developments have resulted in a better understanding of the roles of probe geometry, frequency of operation, and material resistivity in determining what information about a particular flaw type can be obtained from the experimental data. The present work was carried out in close collaboration with Dr. B. A. Auld of the W. L. Ginzton Laboratory at Stanford University and Dr. A. H. Kahn at the Fracture and Deformation Division, Center for Materials Science in Gaithersburg, MD. The work at Stanford has been mainly concentrated on very high frequency (microwave) eddy current probes and theoretical modeling of flaw responses as a function of the probe geometry, frequency of operation and material resistivity. Because many of the important theoretical predictions needed verification in a frequency range not covered by most conventional eddy current inspection systems (100 kHz-2 MHz) and well below the microwave frequencies, it was decided that a new broadband probe design was needed that could be used in the 100 kHz-25 MHz frequency range.

During FY82 the new probe design was developed and a large number of calibration specimens were prepared that were needed for verification of specific theoretical predictions. Because the preparation of calibration specimens involves well known techniques, the present report is focused on the design and operation of the new eddy current probe system, certain experimental highlights and a technique, developed by B. A. Auld, for removing unneeded signal components from the eddy current data.

In the past, it has been pointed out by A. H. Kahn, using an exact theory for two-dimensional surface cracks, that the phase of the eddy current signals experiences a significant roll-off in the region $1 < a/\delta < 20$, where a is the crack depth and δ is the electromagnetic skin depth (1). Later Auld showed that the phase of the signal in the roll-off region is primarily determined by the dimensions and shapes of the crack, and by the distribution of the electromagnetic field beneath the probe. It was then shown that the phase shift in the eddy current signals in the presence of a flaw can be used under certain circumstances for inversion of the eddy current data (2). The principal results of Auld are summarized in Fig. 34(3).

Figure 34 shows the phases of the signals associated with the flaw and lift-off signals as a function of the parameters a/δ , a/c , and \bar{r}/a . Here a is the depth of a flaw, and \bar{r} refers to the mean radius of the coil. It is seen from Fig. 34 that the maximum change in the flaw signal occurs in the range a/δ 5-50, for rectangular flaws with a unity aspect ratio ($a/c \sim 1$).

The electromagnetic skin depth δ is given by:

$$\delta = \sqrt{\frac{1}{\sigma \pi f \mu_0 \mu}} \quad \text{Eq. 1}$$

where σ is the electrical conductivity, f is the frequency, and μ is the permeability of the material under evaluation.

From Eq. 1, it follows that the electromagnetic skin depth for aluminum ($\rho = 2.655 \cdot 10^{-8}$ ohm-m) at 1 MHz is $8.2 \cdot 10^{-5}$ m (0.0032-in). Then, it follows that at 1 MHz the interesting region in a/δ corresponds to a range of flaw depths a from $4.1 \cdot 10^{-4}$ m (0.0161 in) to $41 \cdot 10^{-4}$ m (0.161-in). This range of flaw sizes can be easily obtained using electron-discharge and conventional machining techniques.

Since the operating frequency of most conventional eddy current test instruments does not permit reliable operation above the 1-2 MHz frequency range, it was decided to design a new probe system that would be operable at least over the 100 kHz-25MHz frequency range. Concurrently, special eddy current probes of spiral geometry (pancake) were designed with a mean radius \bar{r} of 1.25 mm (0.050 in).

Figure 35 shows a schematic diagram of the eddy current probe and Fig. 36 shows a block diagram of the experimental configuration. The key component of the eddy current probe is a high-frequency, four port hybrid, which functions as a Wheatstone bridge. The hybrid is normally driven from a 50 ohm signal source connected to the "sum" (Σ) port. The output of the hybrid is obtained from the "difference" (Δ) port. Two identical eddy current coils L_1 and L_2 are attached to the unbalanced, oppositely phased outputs of the hybrid. Because the eddy current coils exhibit very low impedances, broadband impedance matching transformers are used to step up the magnitudes of the coil impedances to the 10-50 ohm range. The hybrid and the impedance matching transformers are designed using bifilar winding (#32AWG) techniques to reduce leakage inductance and minimize interwinding capacitance effects. The winding convention is indicated by the customary "dots" (4,5,6). The two eddy current coils were made by winding 10 turns #30AWG copper wire in a tight spiral pattern.

Figure 36 shows two experimental set-ups that have been used to measure eddy current signals. The system used in the frequency range 100kHz to 1MHz is shown in Fig. 36a. An oscilloscope is used to measure the amplitude and phase of the eddy current probe. The input signals, serving as a reference, also appear on the oscilloscope display. Figure 36b shows the experimental set-up for the 1-25 MHz frequency range. In this case, a vector voltmeter is used to measure the amplitude and phase of the signals appearing at the Δ port relative to the signal applied to the Σ port. A 1MHz overlap region between the two set-ups can be used for comparative purposes. In both cases 1 volt (peak-to-peak) input signals were used. At 1 MHz, the voltage level at the output port (Δ) in the absence of a flaw and for balanced (0.025-mm) lift-off distance between the two probes (L_1 and L_2) was approximately 2 mV. At 20 MHz

this background signal (caused by the bridge being out of balance) was 4.4 mV. The above results indicate that high levels of common mode rejection (CMR) are possible using the probe design of Fig. 35.

The operation of the new eddy current probe was first demonstrated by scanning a tightly closed crack in an aluminum tension specimen. The results, for the case of a scan line bisecting the crack at 90° are shown in Figs. 37 and 38. The tightly closed crack was approximately 5-mm long and 2-mm deep. The phases of the probe output signals are plotted in Fig. 37 and the amplitudes are plotted in Fig. 38 as a function of probe position along the scan line. Data are given at the following frequencies: 200 kHz, 500 kHz, 1 MHz, 2 MHz, 5 MHz, 10 MHz and 20 MHz. It is evident from Fig. 37 that the phase excursion first becomes positive and then negative in relation to the phase of the background signals associated with bridge imbalance. The maximum positive excursion corresponds to the coincidence of the "in-phase" probe with the center of the crack, and the maximum negative excursion corresponds to the coincidence of the "out-of-phase" probe with the center of the crack. The spacing between the two probes (L_1 and L_2) was approximately 33 mm. The results of Fig. 37 and 38 clearly demonstrated the qualitative predictions of Fig. 34. To facilitate quantitative analysis, it is useful to plot the data in Fig. 37 using a vector-diagram presentation.

Figure 39 shows the outputs from the bridge with the "in-phase" probe located directly above the center of the crack (broken lines for flaws and bridge imbalance signals) and far away from the crack (solid lines for bridge imbalance signals). The data was taken from 200 kHz and 20 MHz, corresponding to a two-decade frequency range. The flaw signals are indicated by the solid line vectors drawn between the flaw and bridge imbalance signals (dotted, solid lines). It is seen from the construction in Fig. 39 that the phase of the flaw signal decreases monotonically with frequency. The rate of decrease is slow initially (from 200 kHz to 1 MHz), corresponding to an a/δ range of 11-25. However, the rate of increase is very fast in the frequency range 2-20 MHz, corresponding to the 34-112 range in a/δ . The total phase-shift is -42° , as shown by the construction in Fig. 39. The above observation is in a very good quantitative agreement with the theory of Fig. 34.

From the above results it can be concluded that the phase of the eddy current signals, after subtracting the background signal information, can be used to infer the depth of tightly-closed cracks. The experimental results in this report agree with the theory of B. A. Auld, which has been developed specifically to treat the case of a finite eddy-current coil above a closed crack of finite dimensions. In the future, it is planned to investigate the behavior of the background signals, which ultimately determine the sensitivity of eddy current techniques to flaws. In particular, the phases and magnitudes of coil lift-off and tilt will be investigated as functions of flaw parameters, coil parameters and skin depths.

References

1. A. H. Kahn, R. Spal, and A. Feldman "Eddy-Current Losses Due to a Crack in Conducting Material," J. Appl. Phys. 48 (11), 1977, pp. 4454-4459.
2. B. A. Auld, F. Muennemann, M. Riazat, and D. K. Winslow "Analytical Methods in Eddy Current NDE", in the Review of Progress in Quantitative NDE, ed. by D. O. Thompson and D. A. Chimenti (Pergamon, New York, 1982), in press.
3. B. A. Auld, W. L. Ginzton Laboratory, Stanford University, private communication.
4. H. O. Granberg "Combine Power Without Compromising Performance", Electronic Design 28 (12), 1980, pp. 181-187.
5. R. E. Matick "Transmission Line Pulse Transformers - Theory and Application", Proc. IEEE 56(1), 1968, pp. 47-62.
6. J. Stevick "Broadband Matching Transformers Can Handle Many Kilowatts," Electronics 49 (23), 1976, pp. 123-128.

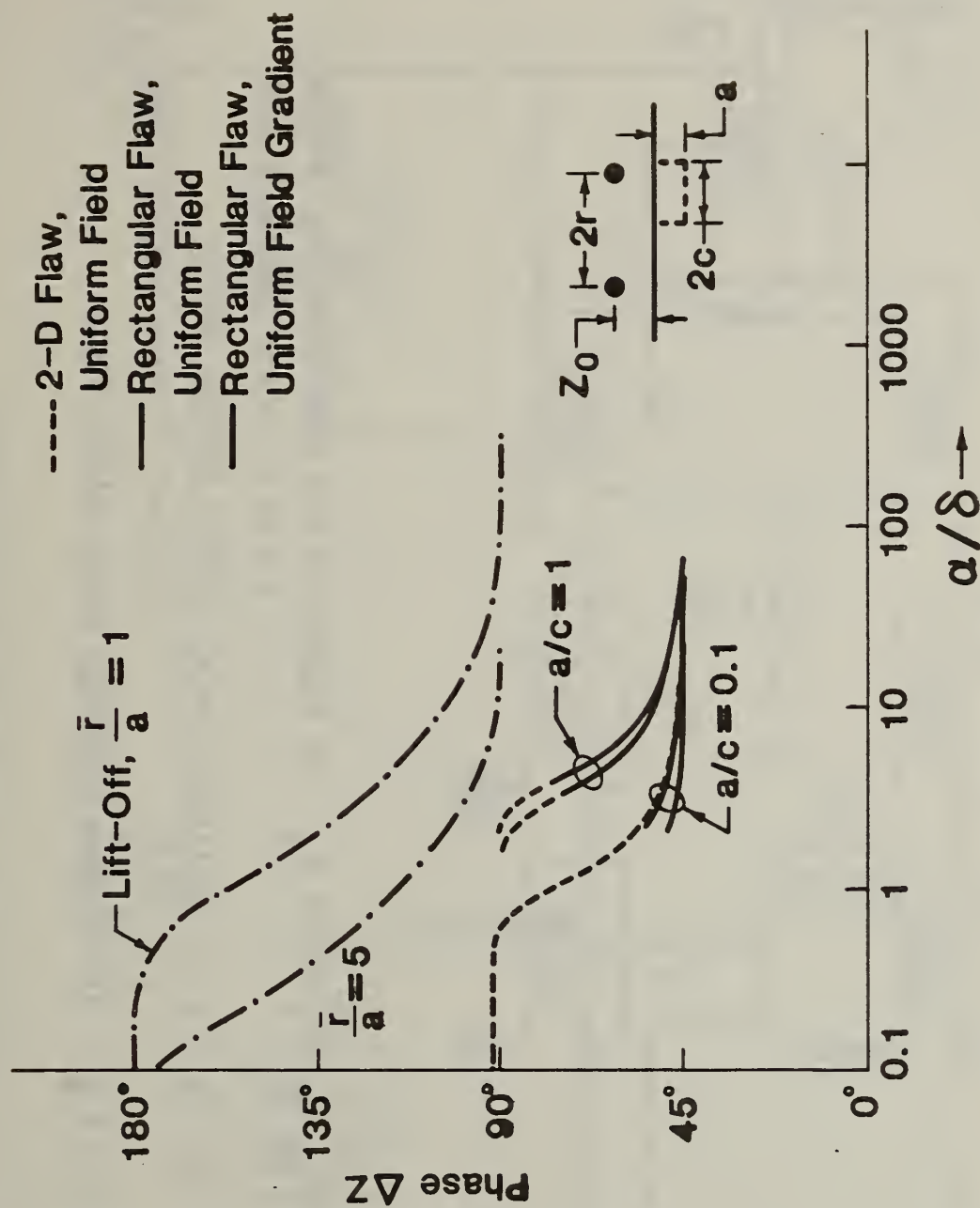
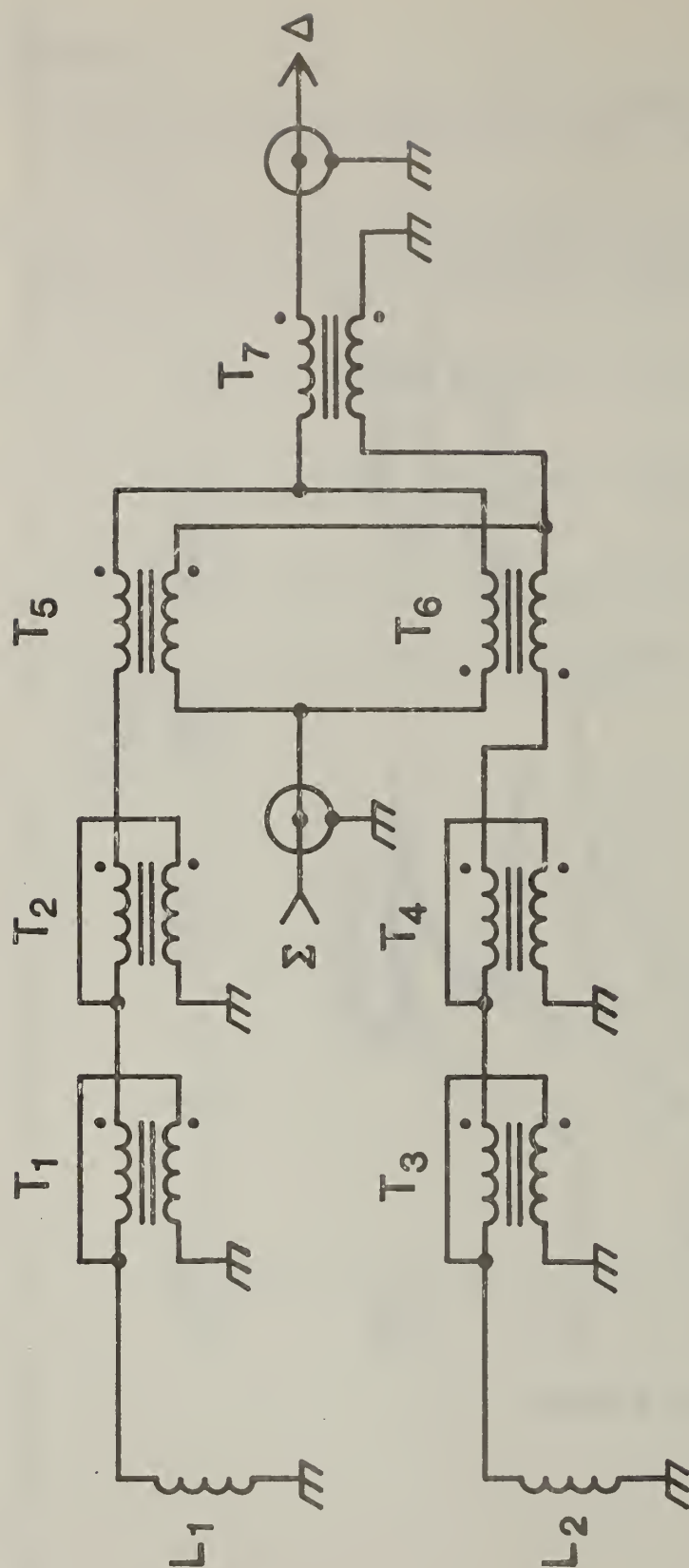


Fig. 34. Normalized phases of flaw and lift-off signals as functions of a/δ , with a/c and \bar{r}/a as parameters.



1. T_1 , T_2 , T_3 and T_4 : 8 Turns #30 AWG Bifilar Wire:
1 Q-1 Core 9.5mm dia.
2. T_5 , T_6 , T_7 : : 8 Turns #30 AWG Bifilar Wire:
2 Q-1 Cores 9.5mm dia.
3. L_1 , L_2 : 10 Turns (Spiral) #30 AWG Wire

Fig. 35. Design of a high-frequency, broadband eddy current probe.

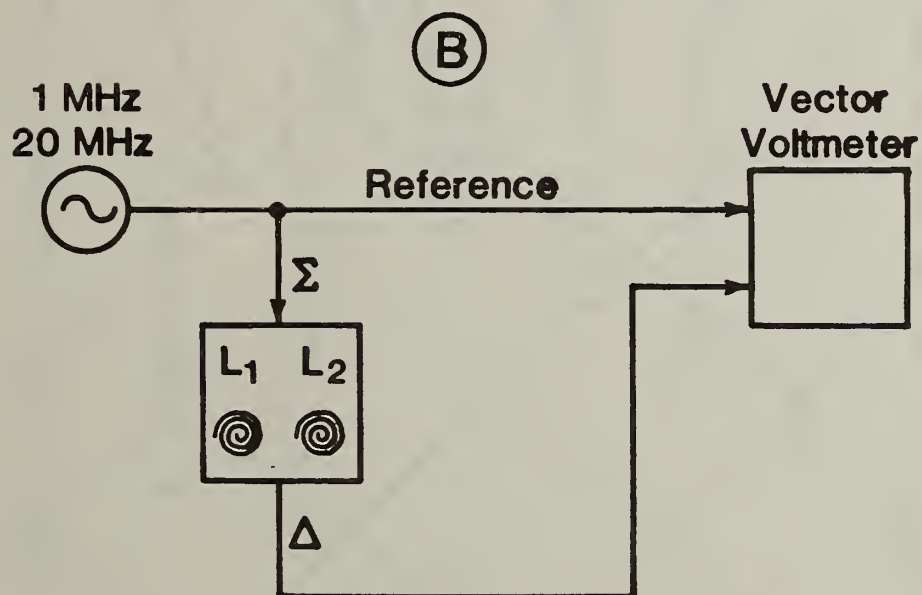
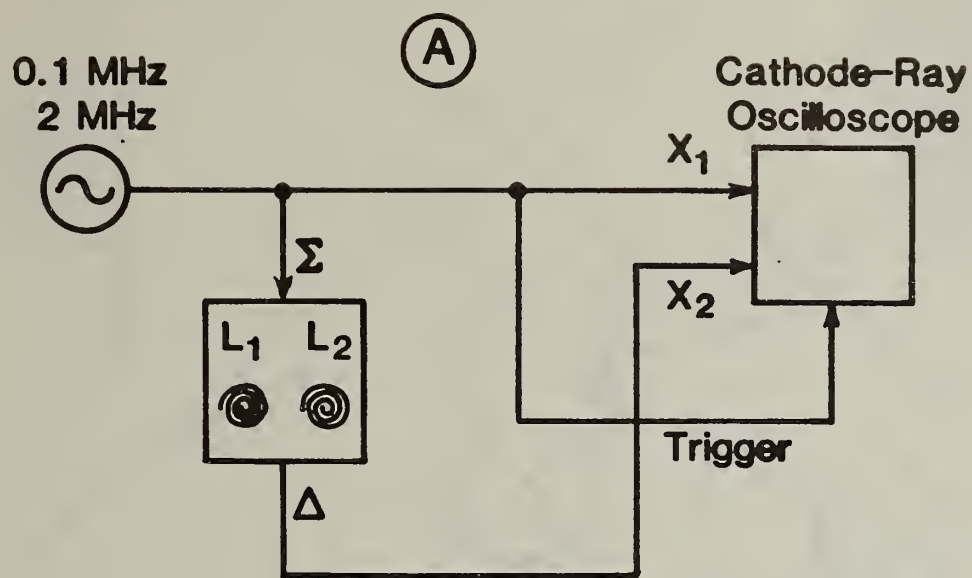


Fig. 36. Experimental setups for measuring eddy current flaw and lift-off responses.

AL CRACK DETECTED BY EDDY CURRENT PROBE PHASE ANGLE AT DIFFERENT FREQUENCIES

0.2MHZ
0.5MHZ
1MHZ
2MHZ
5MHZ
10MHZ
20MHZ

○ △ + × ◇ ▽ ■

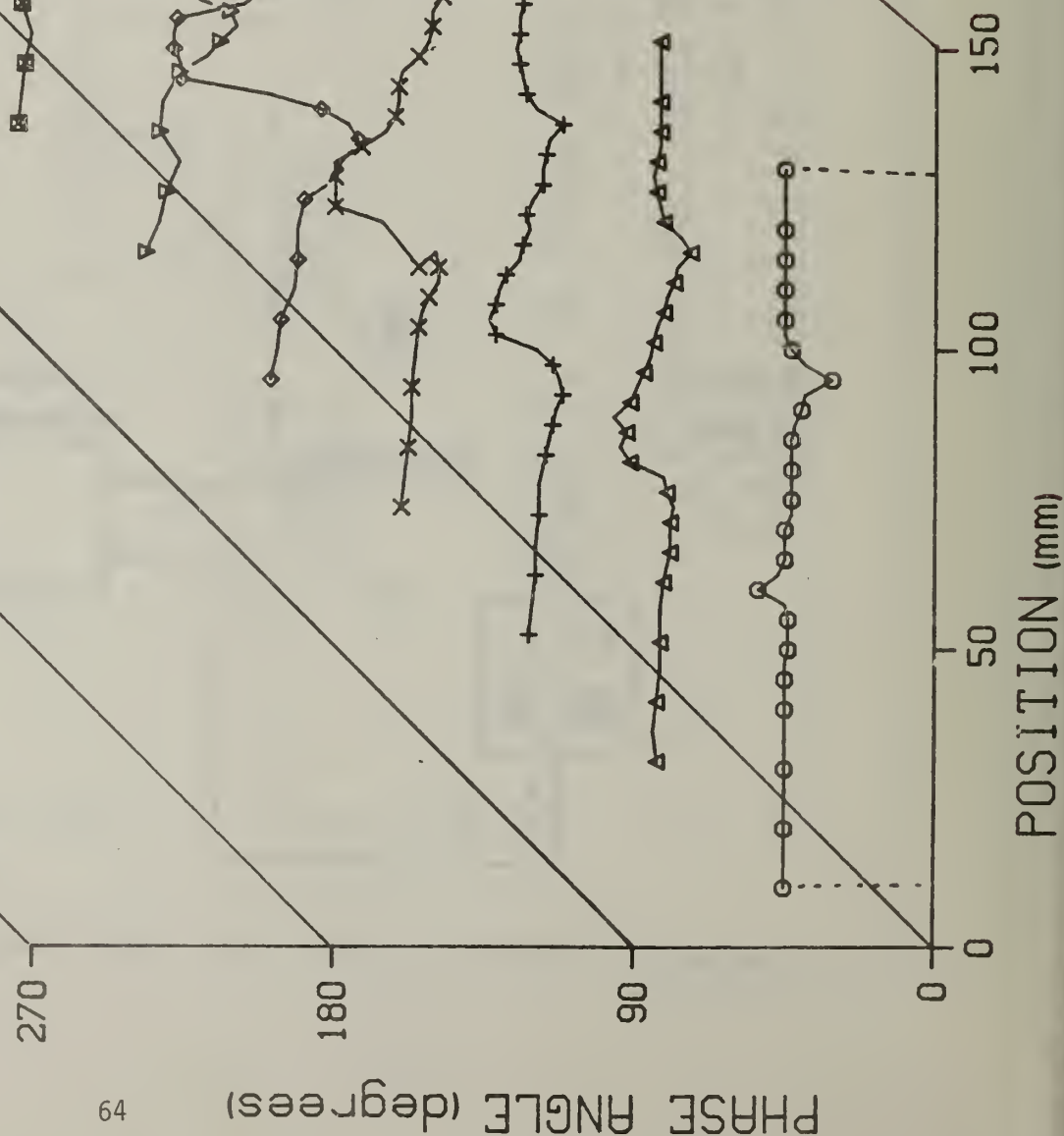


Fig.37. Phases of flaw signals along a scan line bisecting a tightly-closed crack, with frequency as parameter.

SCAN ACROSS CENTER OF TIGHT SURFACE CRACK IN ALUMINUM SAMPLE

0.2MHZ
0.5MHZ
1MHZ
2MHZ
5MHZ
10MHZ
20MHZ

○ △ + × ◇ ▽ ■

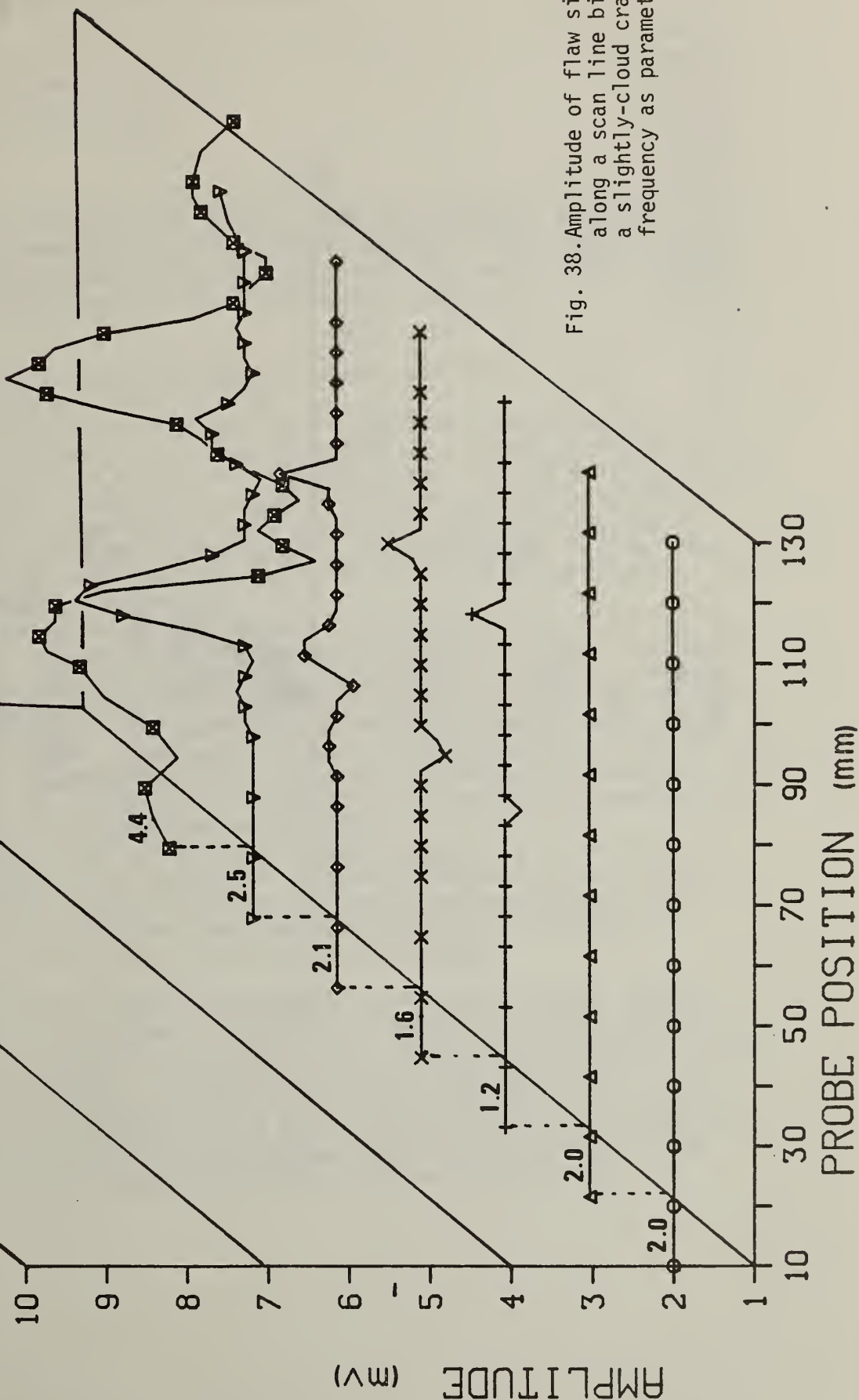
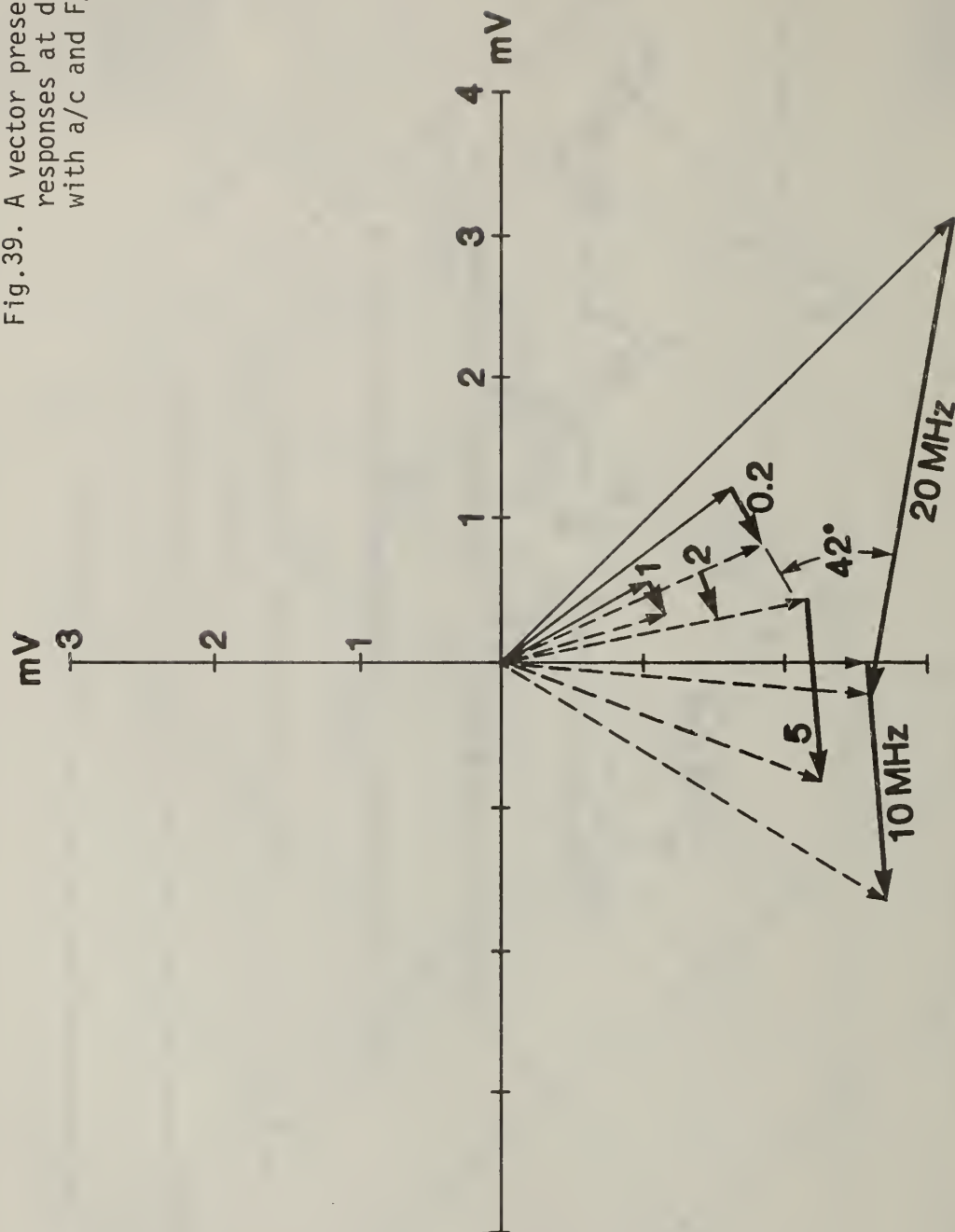


Fig. 38. Amplitude of flaw signals along a scan line bisecting a slightly-cloud crack, with frequency as parameter.

Fig.39. A vector presentation of the flaw responses at different frequencies, with a/c and F/a held constant.



--- Flaw Signal

— Bridge Imbalance Signal

— Bridge Imbalance and Flaw Signal

THEORETICAL MODELLING IN EDDY CURRENT NDE

Arnold H. Kahn

Fracture and Deformation Division

Center for Materials Science

Objectives:

The aim of this project is to provide theoretical support for the development and improvement of electromagnetic methods of NDE. Applications include testing and measurement of materials properties, defect detection and sizing, and contributions to the development of standards.

Accomplishments:

The following major accomplishments have been achieved to date since this program was initiated in 1979.

1) A theoretical analysis was made on the nature of eddy currents in the vicinity of a crack in a conducting material. The applied fields were considered to be uniform in space, as a starting point. In the analysis it was found that the current distribution could be resolved into characteristic distributions associated with the corners and tip of the crack, and that for cracks sufficiently deep, these patterns could be superimposed to give a satisfactory solution. This approach gives insight into nature of the signals arising from a crack.

2) In an attempt to develop the theory on a more quantitative basis, we calculated an exact solution for a longitudinal crack in a cylinder surrounded by a test solenoid. This calculation gave the modification of the impedance diagram due to a crack, over a wide range of frequency and dimensions of the cylinder and of the crack. These calculations were of immediate application in the design of equipment to be used for the production testing of drawn tungsten filament wires for the manufacture of light bulbs. Independent calculations by investigators at the General Electric Company, by the finite element method, were in agreement with the published work by NBS.

3) The analysis of the crack in a plane was extended to cracks of size comparable to the skin depth, the domain of greatest sensitivity of detection. The boundary integral equation method was applied. The results gave the impedance change due to the crack, and the variation of its phase with frequency. Cracks of arbitrary inclination were included.

In the past year the theory was extended so that the boundary integral equation method could be applied to eddy current problems in which the applied excitation field is not uniform in space, as for example excitation by currents in a pair of parallel wires. This model has some of the characteristics of a three dimensional coil configuration, but is still computationally tractable. The necessary computer programs are now being prepared for the production of numerical results on this part of the program. When completed the results will be compared with experiments at NBS and at other laboratories.

The theoretical work on these eddy current problems is being conducted in collaboration with Dr. C. Fortunko at the NBS Boulder Laboratories and Dr. B. Auld of Stanford University.

Future Expectations:

Recent measurements on the phase of the signals from a crack, performed by Dr. Auld and co-workers, give a dependence of phase on frequency similar to that predicted by our theory, but moves to frequencies an order of magnitude higher. Dr. Auld attributes this difference to three dimensional aspects of the measurement system which are not included in our published work. An important part of the work of the immediate future will be the examination of the results of the numerical calculations now being prepared, to ascertain whether spatial limitation of the exciting coil makes a major contribution to the frequency dependence of the phase of the impedance of a crack.

An important part of the theoretical effort will be the collaboration with Drs. Fortunko and Auld in the design of coils and apparatus for the purposes of making critical measurements for testing and theoretical models, and for analyzing the measured results.

In addition to the study of the non-uniform exciting field, we shall also extend the same computational methods to treat open cracks. The results of the calculations may help to explain some of the variability reported in measurements on artificial and natural cracks.

MAGNETIC MEASUREMENTS

Lydon Swartzendruber

Metallurgy Division

Center for Materials Science

Nondestructive evaluation methods utilizing magnetic leakage fields are widely used for detecting defects in ferromagnetic materials such as iron and steel. These methods involve the magnetization of the material and the subsequent detection of the leakage fields resulting from any defects which might be present. A common technique for detection of leakage fields is magnetic particle inspection (MPI). MPI involves the spraying or flowing of minute magnetic particles over the magnetized material. Patterns are formed on the surface which indicate the location of surface or subsurface defects. This method reveals the presence and location of defects, but gives limited information about their size, shape, or depth below the surface. Other methods, such as measurements with a Hall probe or moving coil, give more quantitative information about the leakage field but correlation of the measured field with the shape and location of the defect also presents considerable difficulty.

In a material of constant permeability, analytical calculations of leakage fields for various geometries, such as long transverse cylinders, are possible. We have previously shown that measured magnetic leakage fields above artificial cylindrical defects in a steel sample are considerably larger than the strength calculated analytically for a material of constant permeability, however high that permeability might be. Clearly, the nonlinear B-H relationship has a significant effect in this type of measurement. Thus, any mathematical model of such a system which incorporates permeability as a constant is insufficient; permeability must be incorporated into the model as a function of the field strength. This complication necessitates numerical solutions which require lengthy calculations for each specific case.

Utilizing a nonlinear finite difference method, and an analytical representation of the nonlinear B-H relationship, numerical calculations have been performed on the Metallurgy Division computer. The numerical method was used to calculate leakage fields for subsurface defects and for slits open to the surface. For comparison, linear calculations were also performed. These calculations were then compared with experimental measurements. The nonlinear numerical calculations are in qualitative agreement with the experimental measurements and confirm that: (1) the leakage field perturbation due to the defect continues to increase well into the saturation region of the magnetization curve; (2) the leakage fields have a shape nearly that expected from a linear magnetic dipole, and; (3) nonlinearity causes the defect to appear closer to the surface than its actual physical distance and stronger than predicted by a linear theory.

MAGNETIC PARTICLE INSPECTION STANDARDS

L. Swartzendruber

Metallurgy Division

Center for Materials Science

This project was initiated by the Specifications and Technical Data Branch of the Army Materials and Mechanics Research Center, Watertown, MA. Military Specification MIL-M-11472, "Magnetic-Particle Inspection, Process for Ferromagnetic Materials", is being reviewed for proposed revision or cancellation and replacement by Military Specification MIL-STD-271, Military Specification MIL-I-6868, or American Society for Testing and Materials Recommended Practice E709-80. The contents of these documents have been compared with current state-of-the-art practice in magnetic particle inspection as revealed by industrial practice, available literature, current applicable Military Standards, Aerospace Materials Specifications, and American Society for Testing and Materials documents. A draft version of a revised MIL-M-11472 has been prepared. Feedback from Department of Defense users will be used to eliminate or revise portions as deemed necessary.

DEVELOPMENT AND APPLICATION OF A SECOND GENERATION IMAGE INTENSIFIER
FOR REAL TIME MICRORADIOGRAPHY

M. Kuriyama, W. J. Boettinger, H. E. Burdette, and R. D. Spal

Metallurgy Division

Center for Materials Science

The resolution of real time radiographic systems is often dictated by the spatial resolution of viewing detectors. To overcome this difficulty, an x-ray image magnification technique was developed (1,2). This development does not, however, negate any further improvement of the spatial resolution of image detectors. As a continuing effort seeking a better detector, we have employed a double intensified charge injection device (ICID) camera to develop an x-ray image intensifier. This ICID camera is, in effect, a modified solid-state charge-couple TV camera.

In general, there are two approaches to obtain optical signals from x-ray photons: a) direct photon-electron conversion in videcons and b) visible photons converted from x-ray photons by a phosphor, and subsequently viewed by an optical image intensifier. In this work, we chose the second approach. Phosphors of different particle sizes were prepared on fiber optics plates ($\sim 30 \mu\text{m}$). This ICID camera was tested by a wedge shaped resolution test pattern after one of the fiber optics plates was mounted tightly in front of the camera. Typical results are 2.9 line pairs/mm for FG3M phosphor and 4.5 lp/mm for P20 phosphor (4.3 mg/cm^2) by visual test. The last value corresponds to limiting resolution $110 \mu\text{m}$.

To determine quantitatively the degree of resolution in this system and determine quantum efficiency, another set of measurements was made using this system with the two kinds of phosphors. The ICID camera was operated in photon counting mode, that is, low flux, high gain mode. The image output was digitally processed, using a video frame grabber and a digitizer interfacing LSI 11/23. With the P20 phosphor, the order of 4 pixels in radius per a single photon was observed. One pixel is $40 \mu\text{m} \times 30 \mu\text{m}$. This result agrees with the visual result of $110 \mu\text{m}$ limiting resolution (5% MTF).

Quantum efficiency was found to be 100% with a thick phosphor. The thinner phosphor, the higher the resolution, but less quantum efficiency, as predicted. The decay time of the phosphors was much shorter than the TV frame period ($\sim 30 \text{ ms}$).

This system was used to obtain video tape images from dental teeth, indentation impressions on a NaCl crystal and a copper crystal in the microradiography mode. This system was also used to record real time data from various crystals in the x-ray diffraction topographic mode using synchrotron radiation.

REFERENCES

- (1) W. J. Boettinger, H. E. Burdette and M. Kuriyama, Rev. Sci. Instr. 50
26 (1979).
- (2) 1978 NDE Annual Report.

RADIOGRAPHY

J. W. Motz, R. C. Placious, and D. Polansky
Radiation Physics Division
Center for Radiation Research

A. RADIOGRAPHIC STANDARDS

1. Radiographic Detection and Sensitivity

Until recently only one radiographic standard addressed the problem of image quality. This standard uses an image quality indicator called the plaque penetrameter. While it is widely accepted and used, it lacks the ability to accurately measure an x-ray system's real image quality limits. Moreover, statistical analysis was impossible since it required that only one "event" be detected (one hole in one plaque).

To allow a better evaluation of image quality, a new standard was developed requiring that a statistically significant number of images be detected. Moreover, fine graduations were built into the system so that penetrameter sensitivity could be measured over a range of values instead of one. This new standard was designated "A Standard Method for Determining Relative Image Quality Response of Industrial Radiographic Film". It now carries an ASTM designation, E-746-80, and NBS can supply it to users as an SRM. The numerical index resulting from use of this method is "EQUIVALENT PENETRAMETER SENSITIVITY (EPS)".*

Following this introduction of a new image quality standard, users of high energy radiation (for very thick materials) asked for a similar capability and we have been working on this problem.

Several NBS designs were tried by users around the country. None of these proved to be sufficiently suitable for adoption as an industry standard. Each design, when tested, proved deficient in one respect or another. For example, the high energy system on an absolute basis has significantly lower EPS capability. This has led to problems in "tuning" the test device to the proper range of EPS values. The X-Ray Physics Group of NBS in cooperation with the Office of Nondestructive Evaluation, is providing the designs, the test devices, and the exposure protocol for this work. We also collect test data and evaluate the results of the round robin tests. Our plans are to continue this activity to its conclusion. We have recently developed a new model image quality indicator which it is hoped will eliminate some of the previously revealed difficulties and will prove to be the final version. A document will then be developed and submitted to ASTM for review and approval.

* See ASTM Standard E-142-77

2. Development of a Visual Acuity Standard for Radiographers

Recently a design for testing visual acuity of radiographic inspectors has been published (1). This should prove to be a useful standard and will probably be introduced to the NDE community through ASTM or ASNT.

This design is being developed into a working device by the X-Ray Physics Group of NBS. A number of test patterns are needed for this standard. The present approach is to develop the test patterns using a radiographic rather than a photographic method. Reproducing the test patterns could be done photographically, however. So far we have produced one set of the patterns for the thinnest slit and three specified contrast levels.

We plan to continue development of this system and will recommend, if necessary, coordination of a series of round robin tests among radiographic nondestructive laboratories.

3. Unsharpness

Radiographic unsharpness, also called radiographic definition, has been the subject of many publications in both industrial and medical radiology. It is well recognized that a high degree of unsharpness can greatly affect the analyses of a flaw or even prevent detection. Voluntary standards organizations have been reluctant to support work on this subject. Inasmuch as flaw sizing will eventually become an important factor in NDT, we feel it should be pursued and, if possible, a field method be developed for measuring total unsharpness (U_T).

We have demonstrated the inadequacy of existing procedures for assessing unsharpness by a very brief series of tests. The results are given in Table 1. This data demonstrates that the device produced by CERL* for measuring total unsharpness is not sufficiently sensitive to small variations in U_T and that the calculated value of U_G (geometric unsharpness) is probably low by a factor of two or so. This is not surprising since it considers only the geometric variables of the x-ray system.

Our plans are to continue work in this subject, at a fairly low level of activity, however, and to gear our effort to a system which will measure U_T rather than U_G and which will be relatively easy to adopt to field use.

* Central Electricity Research Laboratories, Surrey, England.

Table I

Unsharpness Data

- I. kVcp=200, source size= 4x4 MM, SFD=32" (81.3 cm) film type - Kodak AA, Screens=.005" front .010" back (Pb)

<u>Test</u>	<u>Film Density</u>	<u>Screens</u>	<u>Absorber</u>	<u>Results</u>		
				<u>CERL</u>	<u>UG</u>	<u>EPS(%)</u>
1	2.14	No	None	.005"	~0	-
2	1.93	Yes	None	.008"	~0	-
3	1.75	No	1/4" steel	.008"	.002"	3.57
4	1.56	Yes	1/4" steel	.008"	.002"	3.57
5	2.10	No	1/2" steel	.008"	.003"	2.26
6	2.75	Yes	1/2" steel	.013"	.003"	2.26
7	1.95	No	3/4" steel	.010"	.005"	1.51
8	2.27	Yes	3/4" steel	.010"	.005"	1.51

- II. Same as above except SFD = 64"

1	2.54	No	None	.004"	~0	-
2	2.42	Yes	None	.004"	~0	-
3	2.42	No	1/4" steel	.004"	.001	2.83
4	2.41	Yes	1/4" steel	.004"	.001	2.83
5	2.51	No	1/2" steel	.005"	.002	1.79
6	2.57	Yes	1/2" steel	.005"	.002	1.67
7	2.41	No	3/4" steel	.005"	.003	1.25
8	2.82	Yes	3/4" steel	.005"	.003	1.19

Note: SFD is x-ray Source to Film Distance

4. X-Ray Film Handling

Two documents are being developed in cooperation with and in collaboration with the film company representatives in the ASTM subcommittee on radiographic practice. One relates to film processing, the other to film storage (exposed and unexposed). Our role is as coordinator of these activities. The technical content is the responsibility of the film representatives.

5. Component Evaluation

There are, at present, two efforts being conducted in cooperation with ASTM. These are in the area of kilovoltage calibration and x-ray source size (focal spot) determinations. We are part of the task force involved in these efforts. While laboratory methods are readily available for this kind of measurement, good field techniques remain to be perfected. The consensus of opinion is that kilovoltage calibration will involve some sort of variable x-ray absorption measurement (filter technique) and source size will involve a field application of the pinhole imaging technique.

We will continue to participate in this development by providing some of the tests needed to establish the basis of the standard and later, if needed, calibrations of the field instruments at the NBS facility.

Both of these are high on the ASTM "want" list.

6. The Plaque Penetrameter Standard

As previously mentioned in A-1 above, the plaque penetrameter is the only image quality indicator that has been widely accepted and used by the industrial radiographic community for many years. It has some deficiencies and there is a "streamlining" effort now underway for this IQI. An attempt is being made to reduce, if possible, the number of different sizes and the number of different materials that are specified in the standard (E-142-77). NBS is in the forefront of this effort and has participated in the round robin tests associated with this task. This work will continue until the final form of this simplification of the plaque penetrameter is adopted or discarded.

B. RADIOGRAPHIC APPLICATIONS

1. NDT Support for the Fleet Ballistic Missile System*

The objectives of this program are to (1) provide technical engineering support to the area of nondestructive testing applications for Trident missile components, (2) recertify, twice yearly, all facilities involved in x-ray inspection of Trident rocket motors and (3) proposed evaluate changes in inspection techniques.

* This work is supported by Strategic Systems Project Office, Dept. of the Navy.

The recertification program of radiographic testing facilities is carried out twice yearly by an audit that consists either of visits to installations or submittals of test film for evaluation. This testing procedure verifies that all facilities are following the required test procedures and that a high quality of inspection is maintained throughout the year.

The implementation of real time radiographic testing at all facilities involved in the missile system necessitated extensive qualification testing of new equipment and personnel. This work is continuing at the Navy support bases receive their real time equipment for installation and use. Another certified measurement that was required was the measurement of the radiation outputs of the linear accelerators at all facilities so that radiation flux requirements during inspection can be specified.

Proposed new missile systems being developed for the Department of Defense have required a review of existing nondestructive test systems regarding their applicability to these larger missiles. In addition, there have been proposed new methods of inspection such as computerized axial tomography. These systems are being evaluated. Review and consultation on projects involved in tomographic inspection of the Navy and Air Force new missiles will continue.

2. Digital Radiography

Digital radiography involves the scanning, digitizing, and storing in computer memory of a radiographic image. The image may be from a conventional radiograph or from a real time imaging system.

This activity is growing rapidly throughout the industrial community. ASTM has established a subcommittee with responsibility to develop standards related to real time industrial radiology. NBS is represented on this subcommittee (two participants). We foresee that image quality standards, real time inspection methods, and (probably) image processing and storage will be a part of this effort. The first output of this committee is a tutorial document on real time radiography. D. Polansky contributed one chapter for this document. Since this is a new group in ASTM and since the technology is presently undergoing many changes and advancements, the NBS role is not yet clearly delineated. Our present efforts are slanted toward acquiring expertise in the use of the systems and their advantages/disadvantages relative to a film based system.

As an adjunct to this activity, we are devoting our efforts to acquiring an image processing system and to achieving expertise in image processing of industrial radiographs and images from real time detectors systems. We feel strongly that the future of industrial inspection will be in digital radiography and we are attempting to define the NBS role and be ready to solve some of the many measurement problems that will arise as the technology grows.

3. High Energy Transmission X-Ray Diffraction

This effort is being done in collaboration with other NBS investigators, headed by Dr. M. Kuriyama.

REFERENCES

1. NBS Technical Note 1143. "Visual Acuity Testing of Radiograph Inspectors in Nondestructive Inspection," G. Yonemura, June 1981.

DESIGN STUDY OF A FACILITY FOR NEUTRON-ACTIVATION AUTORADIOGRAPHY OF PAINTINGS AT THE NATIONAL BUREAU OF STANDARDS REACTOR

Y. T. Cheng and M. Ganoczy

Reactor Radiation Division

and

I. Schröder

Nuclear Radiation Division

Art conservation laboratories regularly employ techniques such as x-ray radiography and microscopic examination of pigment layer cross-sections in the study of paintings. X-ray radiographs, however, show only the distribution of dense pigments such as lead white and thus provide only part of the analysis. Relatively recently neutron-activation autoradiography has been used. It extends the range of information that can be obtained by being able to measure the distribution of several pigments other than lead and at the same time identify the elementary composition of the painting.

A current drawback of the neutron technique is that the radiation dose to the painting is two orders of magnitude greater at the existing facilities than a typical x-ray examination. Although this is believed to be well below the level that would damage the painting, it cannot be shown that such radiation doses might not result in some deterioration that would not appear until many years in the future. Therefore, it is very important to reduce the radiation dose to as low a level as possible.

A proposal was submitted to the Smithsonian Institution and subsequently a contract was awarded for a design study of a painting autoradiography facility that would reduce the radiation dose received by a painting by an order of magnitude compared to that available at other reactors. The possibility of building such a facility is made feasible by the unique thermal column built into the NBS Reactor. The proposed study will result in a detailed design of the facility, a cost estimate for its fabrication, and more detailed measurements of the radiation fields.

Experiments were carried out to gather information concerning thermal neutron flux distribution, neutron to gamma ratio, field nonuniformity, size of usable thermal neutron field, radiation shielding requirements, etc..

Figures 40 and 41 show the plane view and side view of the proposed NBSR neutron-activation autoradiography facility, respectively.

The proposed facility will be used for studying oil paintings up to 6' x 6' in size. Flexibility has been built in the design for future expansion to accommodate paintings of larger sizes and modification of the graphite thermal column to improve neutron to gamma ratio.

The neutron-activation autoradiography process utilizes neutron-activation analysis to identify elemental contents in the painting materials and the autoradiographs serve to show the spatial distributions

of these elements. Thus, to make the designed facility suitable for painting studies, a recommended procedure for activation counting and producing autoradiographs was set up. During the course of gathering design information, a test panel, two icon paintings, and an early American painting by Thomas W. Dewing were studied. The study showed the recommended procedure (Table 1) should be followed if the information about short-lived elements (Al, Cu, Ag, etc.) is desirable.

TIME	EVENT	OPTIMIZATION OF AUTO- RADIOGRAPHIC EFFECTS
$T_0 = 0$	End of neutron activation	
$T_1 = 5m$	1st film on for 4m	Ag 108 (2.3m) Al 28 (2.3m) Cr 55 (3.6m)
$T_2 = 11m$	1st γ -spectroscopic count for 5m	
$T_3 = 18m$	2nd film on for 15m	S 37 (5.0m) Cu 66 (5.1m) Ti 51 (5.8m) Ca 49 (8.8m) Co 60m (10.5m) Mg 27 (9.5m)
$T_4 = 34m$	3rd film on for 45m	Sb 124m (21.0m) Cl 38 (37.3m) Cd 111m (49.0m)
$T_5 = 1H25m$	2nd γ -spectroscopic count for 30m	
$T_6 = 2H$	4th film on for 3H	Ba 139 (85m) Mn 56 (2.58H) Pb 209 (3.3H) Cd 117m (3.0H)
$T_7 = 5H10m$	3rd γ -spectroscopic count for 3H	
$T_8 = 8H20m$	5th film on for 15H	K 42 (12.5H) Cu 64 (12.8H) Na 24 (15.0H) As 76 (26.7H)
$T_9 = 1D$	4th γ -spectroscopic count for 10H	
$T_{10} = 2D$	6th film on for 3D	Au 198 (2.7D) Hg 197 (2.7D) Sb 122 (2.8D) Ca 47 (4.7D)
$T_{11} = 5D$	5th γ -spectroscopic count for 3D	
$T_{12} = 10D$	7th film on for 14D	P 32 (14.2D) Cr 51 (27.8D)
$T_{13} = 30D$	8th film on for 30D	Hg 203 (47D) Fe 59 (45D) S 35 (87D) Ca 45 (153D) Ag 110m (253D) Fe 55 (2.6Y) Co 60 (5.26Y)

Table I. Recommended Sequence for Gamma Counting and Film Exposure for Autoradiography.

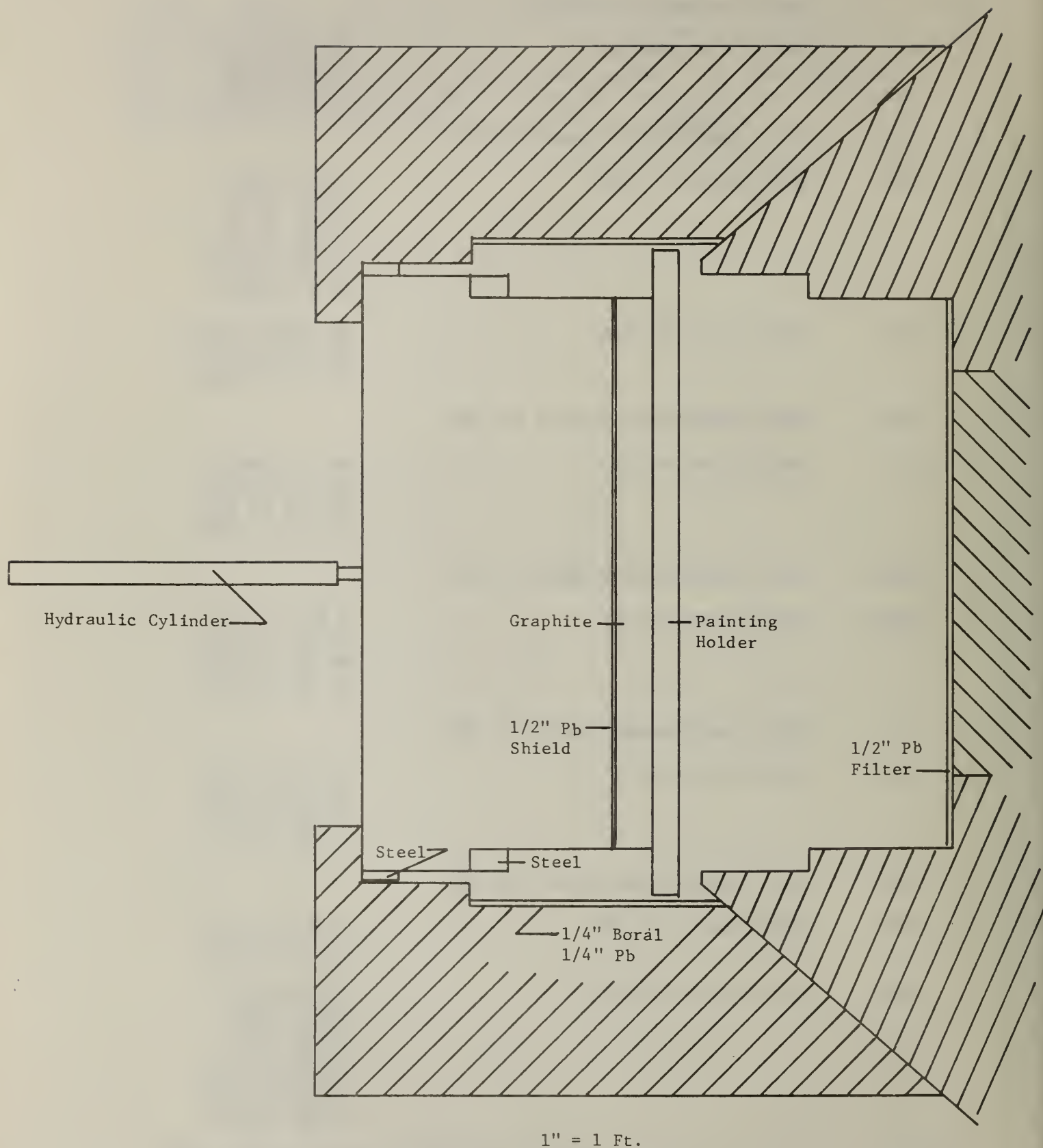


Fig. 40 Top View of the Proposed Painting Autoradiography Facility.

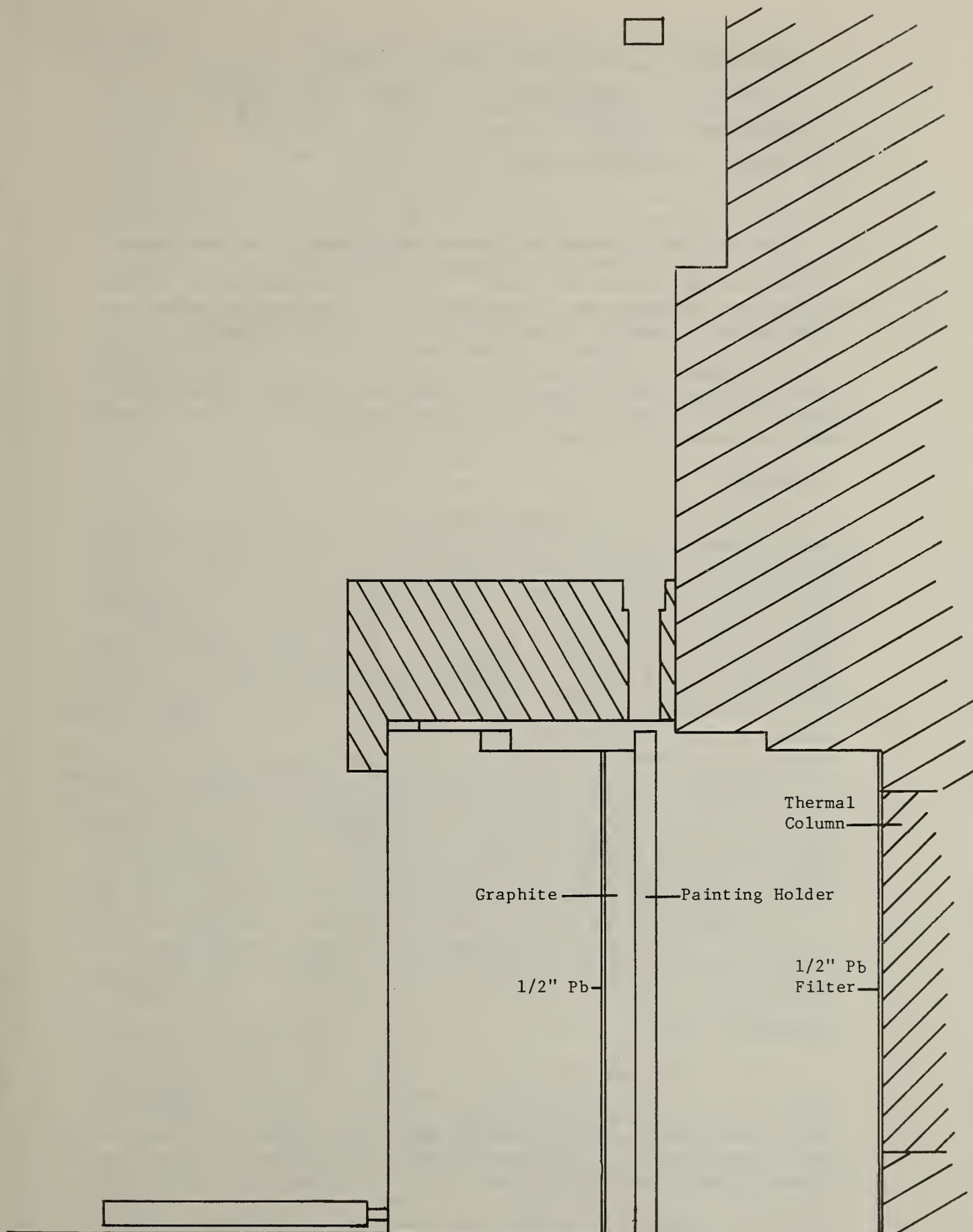


Fig. 41 Side View of the Proposed Painting Autoradiography Facility.

DEVELOPMENT OF HIGH OPTICAL DENSITY STANDARDS

J. Hsia, C. H. Popenoe, and R. L. Booker

Radiometric Physics Division

Center for Radiation Research

The anticipated change in ISO and ANSI standards and continuous demands for higher optical density standard materials require proper action from NBS to meet the needs. Optical Density standards are used to calibrate densitometers. Densitometers are employed to measure exposed X-ray films which are used for nondestructive evaluation.

The objective of this project is to develop high optical density standards (up to optical density of about 5.8), through automation of Inverse Fourth Apparatus(1), characterization of Inverse Fourth Apparatus and development of high optical density standards.

AUTOMATION

A schematic of the Inverse Fourth Apparatus is shown in Fig. 42 . The flux received by a detector at a distance d from the carriage (CR) is proportional to the inverse fourth power of the distance d . Light flux (S) through the source aperture (SA) is irradiated onto the glass fiber (G) on the carriage (CR). The flux is reemitted as the secondary source through baffles (B), sample holder (H) and into the entrance aperture (EA) of the detector system (D). A new sample holder has been constructed utilizing a stepping motor (M) to move sample step by step in or out of the light path. A small pressure-vacuum pump or a solenoid-activated mechanical device (SP) will be used to press the sample tightly against the entrance aperture (EA). The current from the detector is converted to frequency with the current-to-frequency converter (C/F) and the frequency is counted by the counter (C1). The interface (I) receives signals from the counter (C1) and the distance position meter (C2). The interface also relates command from the microcomputer (MC) to the sample holder motor (M), sample positioning device (SP), and carriage motor. The experiment is controlled by the microcomputer through CRT and the data is displayed on a CRT, printed on the printer (PR) and stored in the disk. Some of the computer softwares are being developed. The goal of the automation is to increase precision and ease of operation and characterization. Some detailed results are given below for the characterization of the color temperature of the light source system plus the glass fiber.

CHARACTERIZATION

Current ANSI specifications(2,3) require that illumination of the sample be with light having a color temperature of 3000K. Obtaining a light source which emits 3000K light is simple enough; any number of tungsten filament lamps are available that can be operated at a specified color temperature such as 3000K. However, in the inverse fourth apparatus, radiation emitted from the source is systematically directed by an optical system that includes a reflector, filter, lenses, diffuser, and optical fibers. If each of these components is spectrally non-selective, then 3000K radiation from the source will pass spectrally

unmodified to the surface of the optical density step tablet to be measured. However, manufacturer's data and measurements on similar components indicate that each of the components departs from spectral neutrality to some degree. One approach in determining how light from the source is selectively attenuated would be to measure the spectral reflectance or transmittance of each of the components and then compute the individual and net effects on the chromaticity of the source. This is easier said than done, since the components are non-planar and are imbedded in the instrument. However, since what we want is the net effect, a procedure that characterizes the nature of the resultant light from the source system is both acceptable and feasible.

We used a portable Pritchard 1980B spectroradiometer to measure the spectral radiance of the light from the source system. A color temperature calibration curve on the spectroradiometer was obtained by characterizing a source at 4 color temperatures in the range of interest for the inverse fourth source. During calibration of the spectroradiometer, the light from the standard source was reflected from a diffuse, white Halon plaque. On evaluating the inverse fourth source, this same Halon plaque was used to reflect the light to the spectroradiometer. During these measurements, the turn-around carriage was positioned in its full forward position to increase the light flux at the entrance aperture of the detector port to its maximum value. The detector module was then removed and the Halon plaque positioned to provide a suitable target for the focusing optics of the spectroradiometer. The spectroradiometer measured the spectral radiance of the reflected light at 10 nm intervals in the region 400-700 nm and computed the color temperature of this spectral distribution. The voltage to the lamp source was systematically varied and the process repeated until the lamp voltage that produced a source system color temperature of 2856 K (CIE Source A)(3) was determined. A calibration voltage for 3000K was also determined in the process.

The color temperatures measured on the inverse fourth source are actually correlated color temperatures, since, strictly speaking, color temperature implies a Planckian or grey-body spectral distribution. The spectral distributions of the inverse fourth source system, at a color temperature of 3000K, and that of a 3000K blackbody source are shown in Fig. 43. Both curves are normalized at 560 nm, which tends to exaggerate the small differences that appear at both ends of the curve; in fact, the chromaticity coordinates of these two sources are identical.

Other work planned in the future for characterization of the apparatus includes: detector spectral response, distance measurement accuracy, zero distance determination, the uniformity of the power law dependence of the range of the carriage position, and intercomparison with inverse square instrument.

DEVELOPMENT

One X-ray company has produced several high optical density step tablets for us to evaluate. The planned tasks in the future for development of the high optical density standards include: characterization

of candidate materials, calibration of optical density, pilot run with selected users, intercomparison with other international laboratories, final selection of standard reference material and preparation of documentations and certificates.

REFERENCES

1. D. A. Swyt and J. G. LaRock, "Inverse-fourth apparatus for photometric calibration", Rev. Sci. Instrum. 49 (8), 1083-1089 (Aug. 1978).
2. American National Standard, "Conditions for Diffuse and Double Diffuse Transmission Measurements (Transmission Density)", American National Standards Institute, 1430 Broadway Ave., New York 10018.
3. International Commission on Illumination, "Colorimetry", Publication CIE No. 15 (E-1.3.1) 1971.

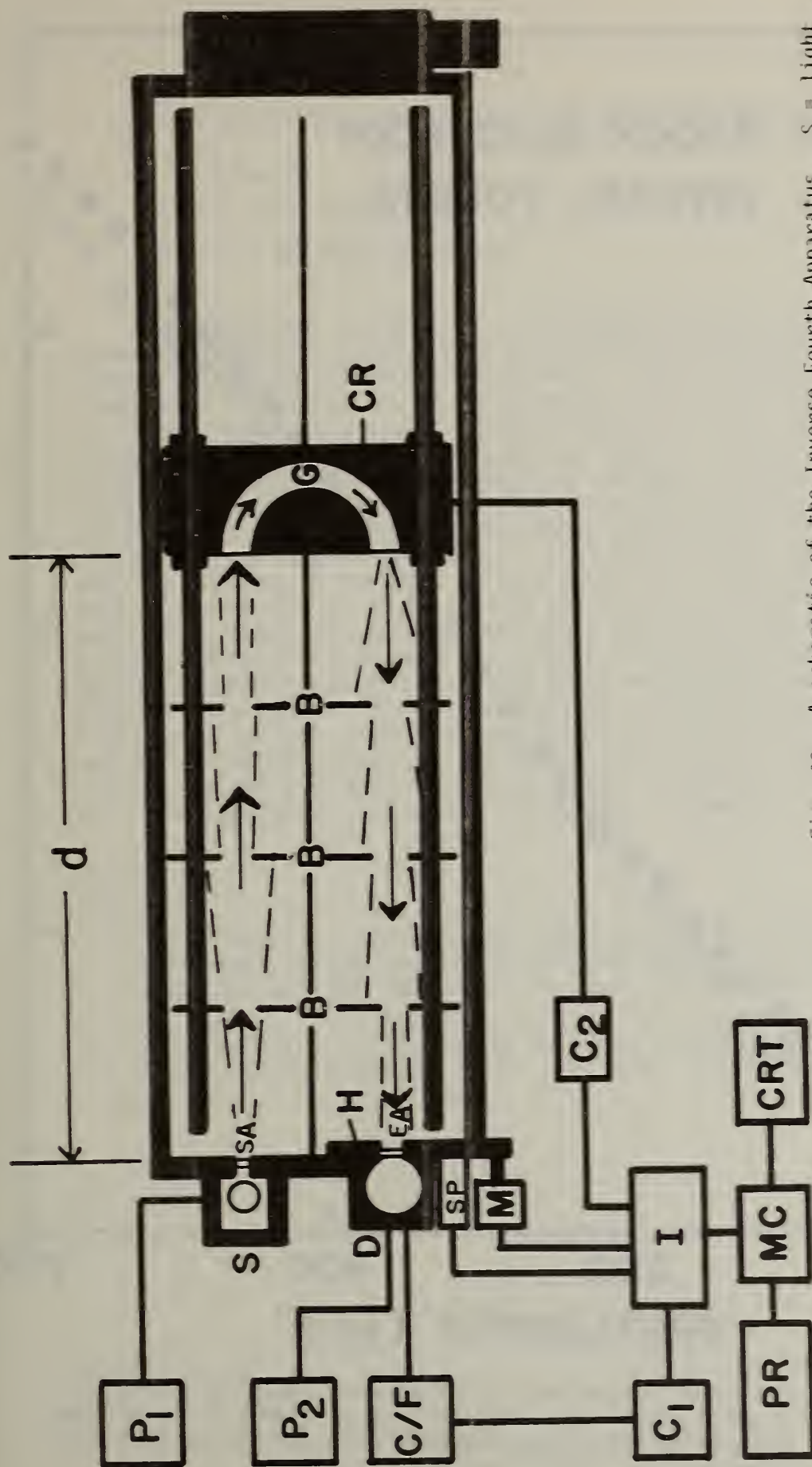


Fig. 42. A schematic of the Inverse Fourth Apparatus. S = light source system, SA = source aperture, G = glass fiber, CR = carriage, B = movable baffles, H = sample holder, SP = sample positioning device, M = motor, EA = entrance aperture, D = detector system, P1 = power supply, P2 = high voltage power supply, C/F = current to frequency converter, P2 = counter, C2 = position meter, I = interface, MC = microcomputer and disk drive, CRT = terminal, PR = printer.

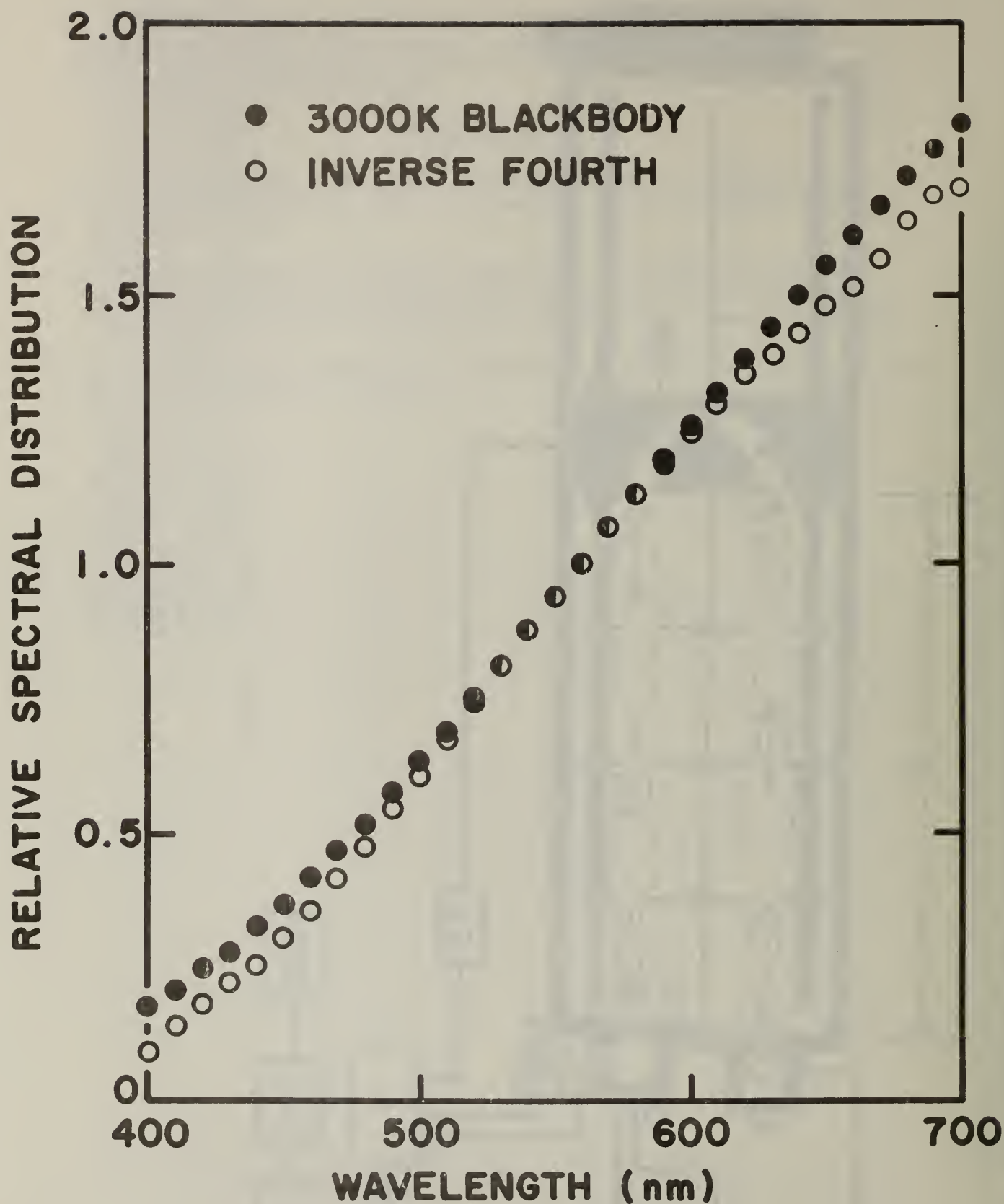


Fig. 43. The relative spectral distribution of the Inverse Fourth Source system (including the optical fiber) at a color temperature of 3000K compared with the relative spectral distribution of a 3000K blackbody source.

VISUAL ACUITY REQUIREMENTS FOR NONDESTRUCTIVE TESTING

G. T. Yonemura

Building Physics Division

Center for Building Technology

The purpose of this project is to improve precision and reliability between instruments, in this case the instrument being the human eye. Studies on reliability of detecting faults from radiographs indicate a significant difference in the performance of different inspectors within a given installation, and a larger difference in the performance between installations. There are several general causes for this lack of precision, but we are addressing one, the visual acuity of the inspectors. Stimulus and observer parameters that can effect precision of fault detection are discussed in reference 1. Microdensitometric scans of aircraft radiographs indicated that defects varied significantly in three variables: contrast (density differences between defect and background), blur (sharpness of the edges) and size (already considered in current tests). Visual acuity test parameters based on the above and other considerations have been recommended in reference 2. These specifications were sent to the medical departments of the different armed services for comments and approval. The specifications were approved by the medical departments of the Army, Navy, and Air Force. Currently master visual acuity test charts are being made radiographically. The master charts will be used to mass produce test charts which in turn will be sent out to the field for validation tests to reflect performance of active radiographic inspectors.

References

1. G. T. Yonemura, "Considerations and Standards for Visual Inspection Techniques," Nondestructive Testing Standards--A Review, ASTM STP624, Harold Berger, ed., Amer. Soc. for Testing Materials, 220-230 (1977).
2. G. T. Yonemura, "Visual Acuity Testing of Radiographic Inspectors in Nondestructive Inspection," NBS Tech Note 1143 (1981).

OPTICAL MEASUREMENT OF SURFACE ROUGHNESS

E. C. Teague, T. V. Vorburger, F. E. Scire, D. E. Gilsinn, M. J. McLay
and C. Y. Trahan

Mechanical Production Metrology Division
Center for Manufacturing Engineering

There have been, over the last ten years, increasing efforts in the U. S. and the rest of the world to use light scattering rather than the traditional stylus instrument for nondestructive evaluation of the surface roughness of manufactured parts. The theory of light scattering from surfaces whose irregularity heights are comparable to and larger than the wavelength of the light is more difficult and much less developed than that for highly polished surfaces. Light scattering has therefore been used primarily for comparison measurements of surface roughness. Our work has been directed towards building the experimental capability and theoretical expertise to investigate the behavior of light scattering measurements in terms of their use for both comparator and absolute determinations of surface roughness.

The basic approach we have taken is to relate light scattering measurements of a test surface carefully to those of area of 3-D stylus measurements of the same surface. Comparisons of characterizations i.e., moments of the surface power spectrum, from the two measurements methods are being used to analyze and determine the valid ranges of different theoretical models and to determine the most efficient detector configuration for an instrument design.

The system, described in last year's report, for performing angular distribution measurements is now assembled and the performance has been very carefully evaluated. A photograph of the completed system is shown in Figure 44. The system consists of an array of 87 detectors interfaced through a 100-channel scanner/digital voltmeter to a Hewlett-Packard 9845T desktop computer. Light scattered from the test surface is picked up with fiber optics places around a 180 degree yolk above the test surface. This multidetector design was chosen because it allows rapid measurements of the angular distribution of scattered light. Some of the system parameters which have been evaluated and our findings are:

- a) Fiber optics transmissivity; uniform to within a three standard deviation of 18.5 percent.
- b) Background noise level of the detector amplifiers; less than 100 microvolts. This noise level results in a useable dynamic range of 10^4 in input light intensity.
- c) Accuracy of angular spacing of fiber optics. Angular position of fiber optic mounts was $2n \pm 0.1$ degrees, where $n = 2$ to 88.

- d) Optical alignment of the fiber optics. The center of the focal region of all fiber optics mounted in the yoke was within one millimeter of yoke center.
- e) Detector linearity. Nonlinearity of a typical detector output voltage is less than five percent over a dynamic range of 10^5 in input light intensity. Tracking of the response properties of the fiber optic/detector/amplifier combinations is still being measured. Initial checks indicate that the voltage outputs of all 87 systems track to better than 25% over three orders of magnitude change in light intensity.

Results from one of our first comparisons of light scattering and stylus measurements of surface roughness are shown in Figure 45. The test surface was lapped stainless steel. The dots are experimentally determined values and the solid line represents the results obtained with a two parameter nonlinear least squares fit to the experimental data. The theoretical model used for this fit was a simpler scalar approximation. It had, as parameters, the root-mean-square deviations of irregularity heights, R_g , and the spatial autocorrelation length of the surface roughness. Better models should yield much closer agreement between theory and experiment both in terms of the agreement between predicted and measured angular distributions and between stylus and light scattering values for the first moment, R_g , of the power spectrum.

Due to unacceptable motion errors found in the x-y stage design described in last year's report, we have designed and constructed a second x-y stage utilizing flexure pivot bearings. This stage, shown in Figure 46, provides for almost error free motion over an area of about 5 x 5 millimeters. The new x-y flexure stage is now at the point of full mechanical operation. Positional readout for each axis is achieved by HP plane mirror interferometers. The scanning axis (x) uses a stepping motor/lead screw drive where the rotational torque (due to the lead screw) is decoupled using a spring loaded "wobble" pin. Data acquisition, control of the start and end of the x-axis scan, and adjustment of the y-axis are all under the control of a minicomputer. The y-axis is incremented at the end of each x-axis scan using a Burleigh "Inch-Worm". The steps generated by this device have not proven to be reproducible at the desired 0.1 micrometer level. To overcome this difficulty the step increment is determined with the HP interferometer and corrected as necessary to achieve the desired accuracy.

Preliminary testing indicates that the monolithic x-y flexure had roll, pitch, and yaw values less than 5 arc seconds. The orthogonality of the axes has been measured to be less than ± 2 arc seconds which is the specified orthogonality of the "True Square" which is used for the interferometer mirrors and for the specimen carrier on the flexure stage.

With both the light scattering apparatus and the 3-D stylus profilometry now in operation and with both systems' performance carefully evaluated, our immediate plans are to continue the comparisons of stylus and light scattering measurements to determine the capability of various models for

accurately predicting statistical measures of surface roughness. Surfaces to be used in the comparisons will range from sinusoidal profile grating-like surfaces to the random surface of an electron-discharge machined surface. Another major objective of our work is to determine the sensitivity of light scattering measurements to the use of different detector configurations, e.g., for a fixed number of detectors, is a measurement performed more accurately with the detectors closely spaced in angle around the specular direction or with the detectors more widely spaced over the full 180 degrees?

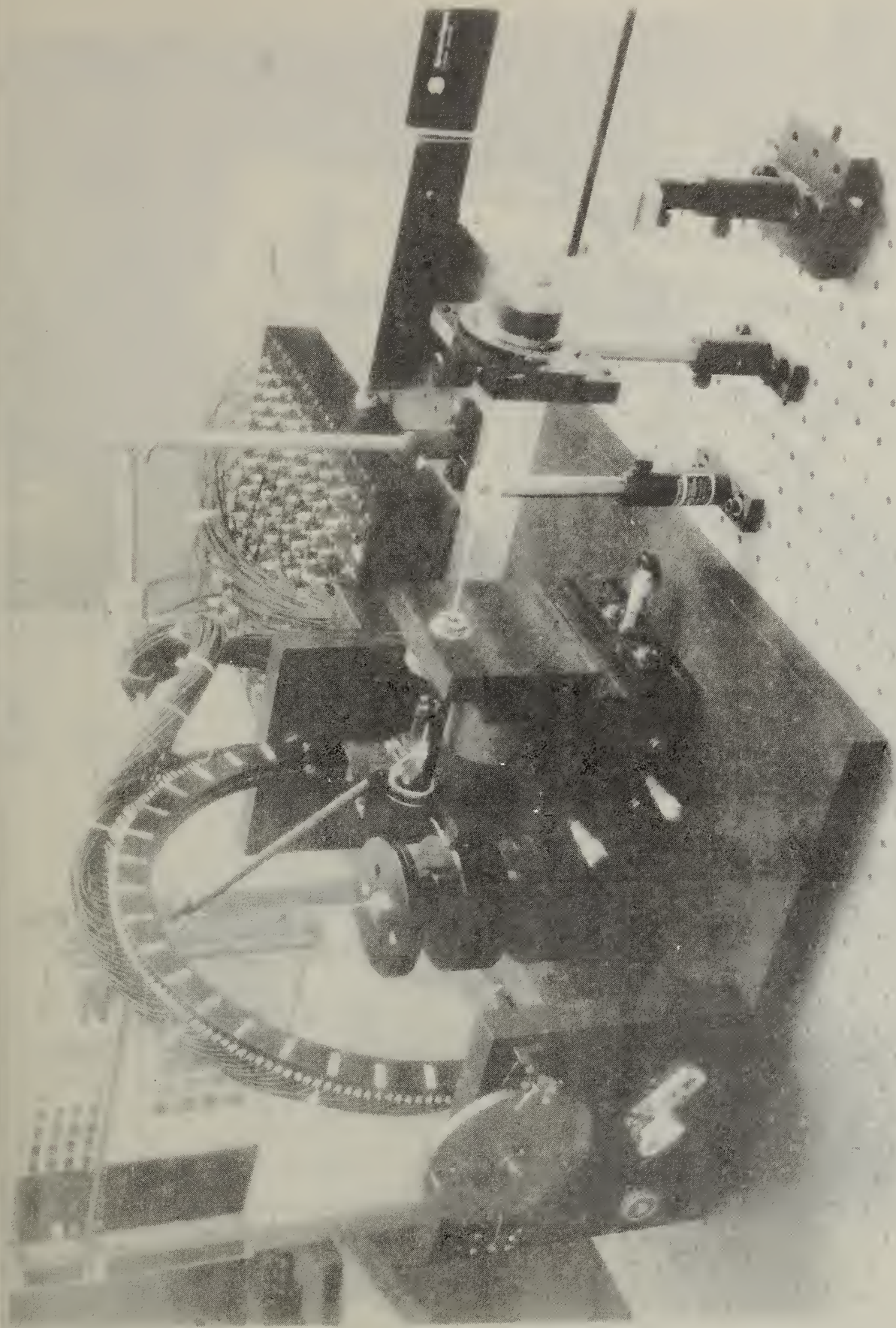
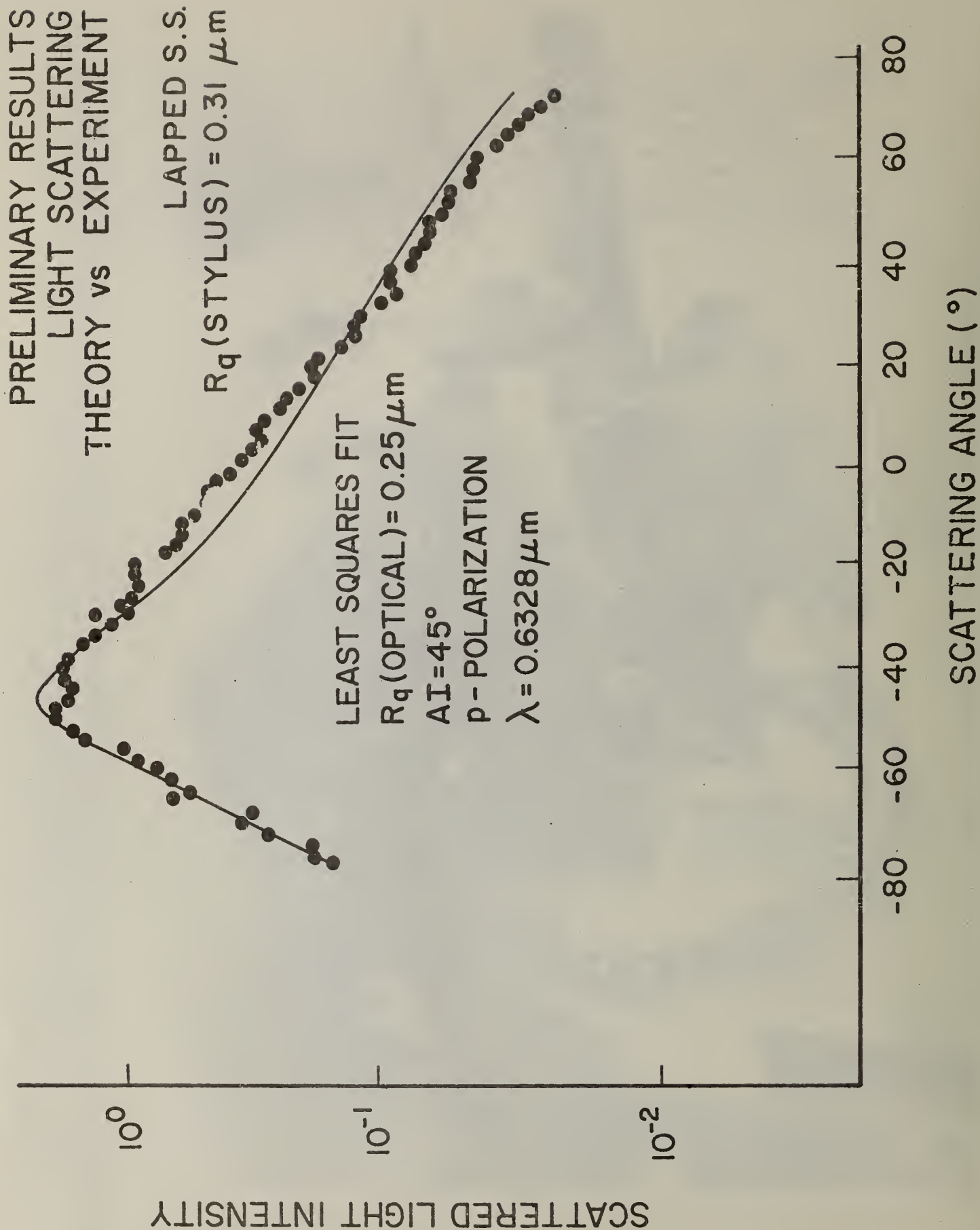


Fig. 44. Photograph of DALLAS apparatus. In the foreground are shown the yoke on the left with lenses and fibers in place, the rotating mirror assembly in the center, and the laser and polarizer setups on the right. In the background are shown the photodiode/opamp detector array and the scanner/voltmeter system, which digitizes the output voltages from the array and sends them to the desktop computer.

FIGURE 45



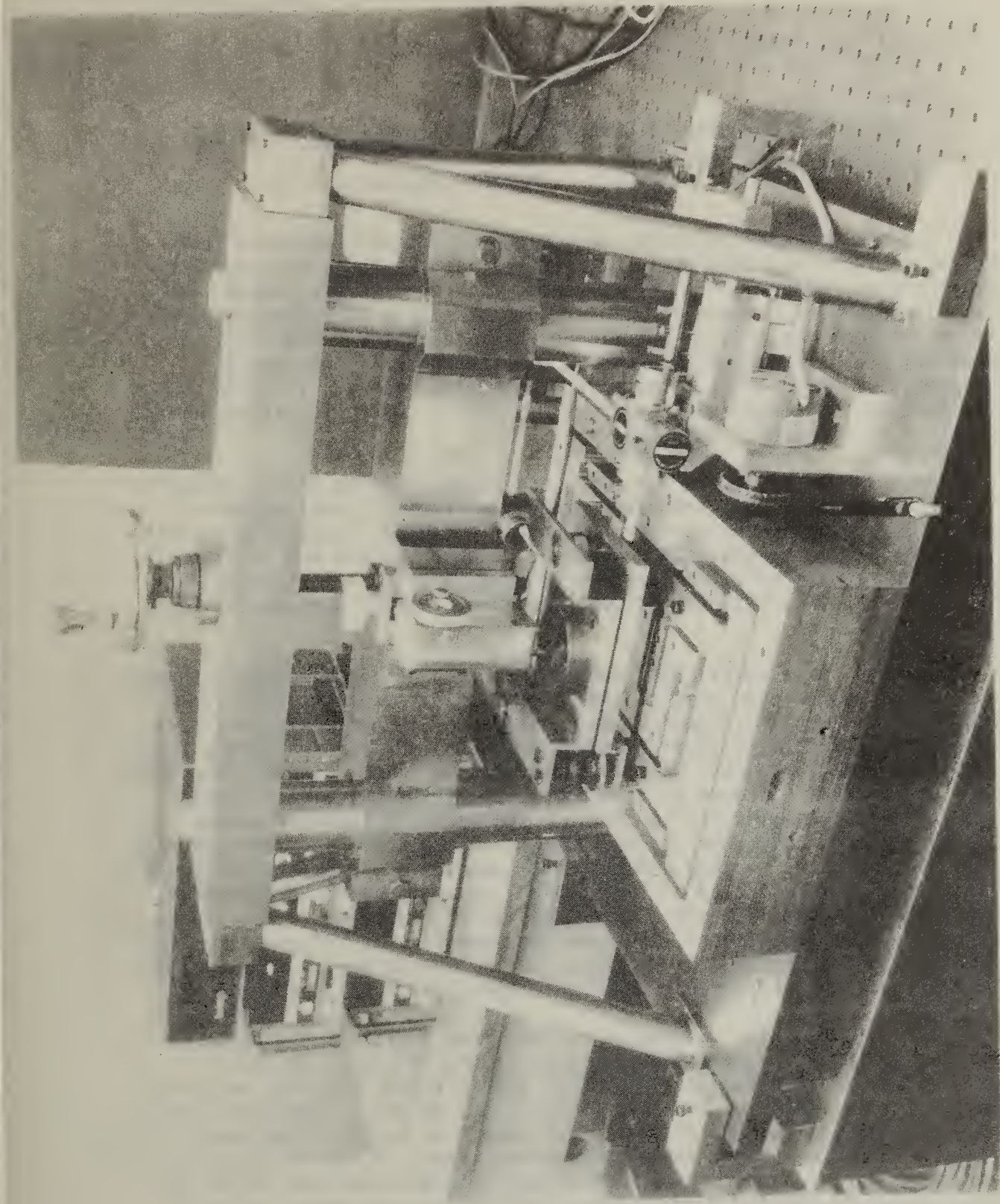


Fig. 46. Photograph of second generation x-y stage for 3D stylus profilometry. The stylus transducer is in the center of the photograph and poised above a thin square test specimen which is in turn resting on the leveling mechanism for aligning the specimen plane with the plane of motion of the stage. One axis of the two-axis plane mirror interferometer system may be seen just above the stepping motor.

LIGHT SCATTERING FROM GROOVES

Grady White

Fracture and Deformation Division

Center for Materials Science

Since manufacturing began, scattering of optical radiation from surface defects has been used qualitatively as the basis for acceptance or rejection criteria. In recent years, this process has ranged from manual comparison between scratch and dig standards to automated comparison of diffraction patterns between acceptable and unacceptable parts. However, with increasing emphasis on quality control, the need for quantitative optical NDE methods is greatly increasing. In particular, the ability to relate specific types of defects to particular scattering patterns is of growing interest.

To that end, work has been progressing in this lab toward measuring infrared radiation scattered from grooves of various cross-sectional shapes and relating the data to theoretical models. Construction of the apparatus has been detailed in previous reports as have the results of scattering from shallow rectangular grooves. For such scattering, a Fraunhofer approximation model provided satisfactory agreement with experiment.(1)

However, more complicated structures, such as grooves with v-shaped or trapezoidal shaped cross sections, provide an excellent test for exact calculations developed by D. Maystre.(2) Accordingly, this past year, detailed calculations after Maystre were made for scattering from real v-shaped grooves and results compared with observed scattering from the same grooves. Figure 47 is a composite of the calculated (solid line) and the observed (solid circles) scattering patterns from one position on a groove. We found that the theoretical predictions agreed very well with observation and the discrepancies could be attributed to finite beam size and lack of longitudinal symmetry of the experimental groove. As figure 48 shows, diamond stylus profilometer traces of the groove, spaced $100\mu\text{m}$ apart, indicate considerable variation in the groove shapes. Because the theory predicts the scattering from specific groove profiles, these variations cause the discrepancies observed.

Currently, we are interested in comparing Maystre's theory to a Fraunhofer model in different extremes of groove size. We have measured scattering from three grooves with trapezoidal cross sections which vary in width, w , from $w \sim \lambda$ ($\lambda = 10.53\mu\text{m}$) to $w \gg \lambda$. The first case is in the resonance domain and the latter should be in the Fraunhofer region. Because Maystre's theory requires expensive calculations, it is of considerable interest to know at what point it must be used rather than the simpler Fraunhofer model. These calculations are about to start.

References

1. G. S. White and A. Feldman, *Applied Optics*, 20, No. 14 (1981), 2585.
2. D. Maystre, private communication.

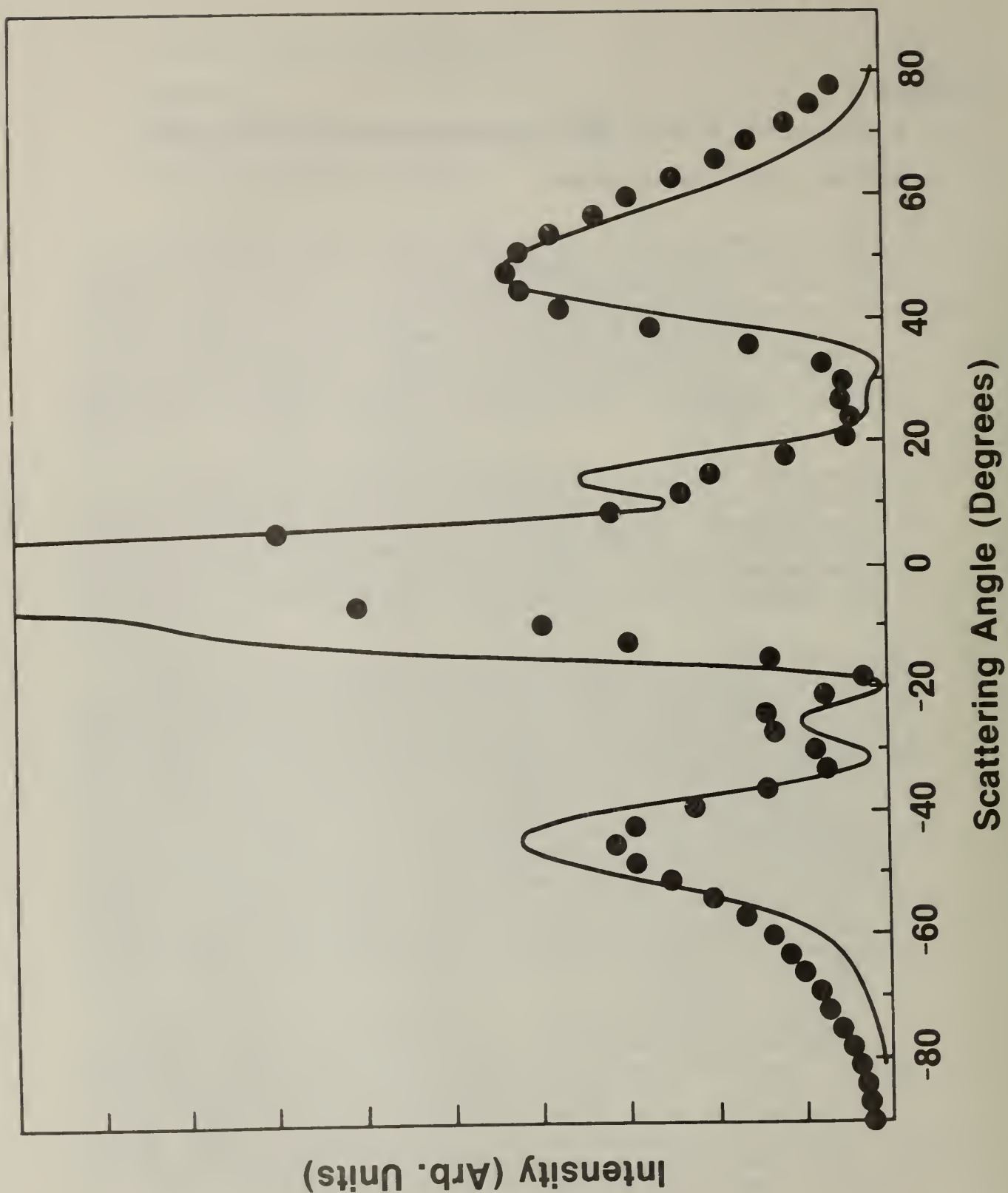


Fig. 47. Comparison between experimentally observed scattering (solid circles) from a v-shaped ($\sim 2\lambda$) groove and theoretical calculations (solid line) based upon the actual groove profile. Lack of symmetry in the scattering profiles reflects corresponding lack of symmetry in the groove.

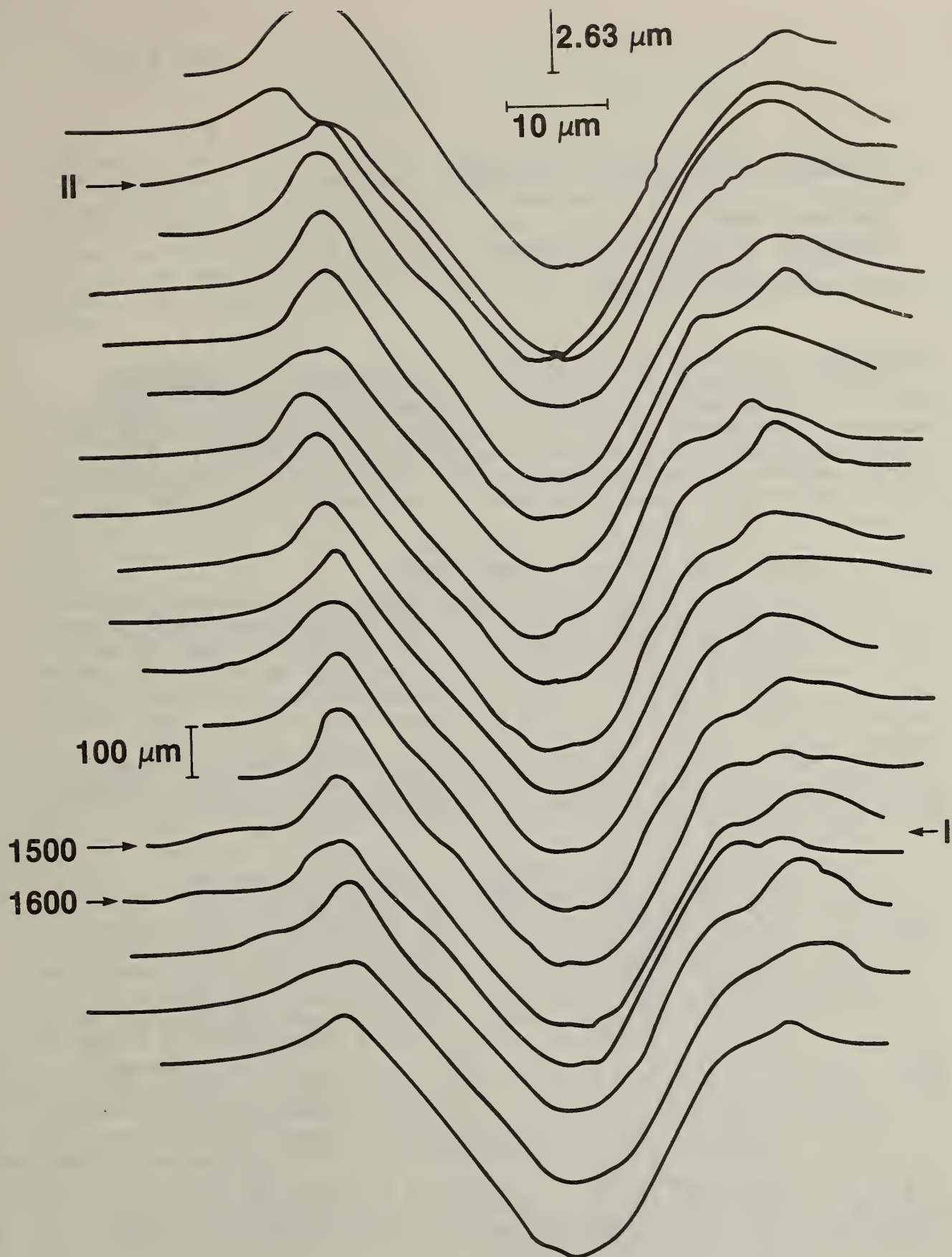


Fig.48. Diamond stylus profilometer measurements of the v-shaped groove. Measurements are taken 100 μ m apart. Positions I and II mark approximate locations of experimental scatter measurements. Theoretical calculations were made from groove profiles at 1500 and 1600 μ m from the groove end.

HOLOGRAPHIC NONDESTRUCTIVE EVALUATION

Charles M. Vest

Department of Mechanical Engineering

The University of Michigan

Objective

This ongoing research project deals with the application of optical holographic interferometry to nondestructive evaluation of materials and components. The project has consisted of a continuing evaluative review of the technical literature of holographic nondestructive evaluation and of a modest experimental research program. All of this work has been carried out with the intent of assessing potential future needs for standards in this area.

Summary of Research Activities and Accomplishments

During the past year, we continued experimental work to determine the deformation of both flawed and unflawed circular aluminum disks subjected to a uniform pressure. The aluminum disks had a variety of "flaws" in the form of blind-drilled holes or slots machined into their back surfaces. A special heavy-duty mount was designed which permitted these disks to be clamped around their periphery with a high degree of uniformity. They were then pressurized from behind with nitrogen. Double-exposure holographic interferograms of these disks were recorded with a pressure change between the two exposures. These interferograms had fringe patterns indicative of the normal deformation of the front surface of the disks under this differential pressure loading.

In the first phase of this project, the flaws were in the form of blind-drilled circular holes located at the center of the disks. Most concepts of holographic nondestructive evaluation require only qualitative interpretation of such interference fringe patterns, because of the presence of a flaw in the object is manifested as an anomaly in the fringe pattern. For example, a region of poor bond in the laminate material may give rise to a local increase in density of fringes when the material is subjected to appropriate differential mechanical or thermal load. The local high fringe density makes the presence of the flaw immediately apparent to the observer. Another example is detection of cracks whose presence causes an abrupt discontinuity in fringes or fringe curvature. This is not true, however, in the application at hand, because the pattern is completely symmetric even in the presence of the flaw. Therefore, a quantitative analysis of the fringe pattern is required. In addition to pure experimental evaluation, we predicted the surface deformation with, and without, central flaws of various sizes and depths using finite element analysis. Good agreement between the finite element calculations and the experimental results were found.

Another aspect of the experimental work conducted over the past year dealt with sensitivity of flaw detection in the pressurized plates. For this work the National Bureau of Standards prepared several aluminum plates with drilled

slots in the back surface. These "flaws" had a variety of sizes, shapes orientations and depths. We found, as would be expected, that the sensitivity of the technique is highly dependent in these various factors as well as the precise location of the flaw. Of particular importance is the orientation of the flaw relative to the fringes in the basic pattern due to the overall deflection of the disk. In particular, if the flaw is parallel to this pattern it may be more difficult to detect than if it is perpendicular to this pattern.

We explored the possibility of forming various types of Moire patterns from combinations of interferograms in order to provide a more sensitive and obvious indication of the presence of a flaw. We had some very interesting successes with this approach. It has been common with objects which are basically flat to form Moire patterns by overlaying two transparencies of interference fringe patterns - one of a "master" component with no flaw, and the other of the object under test. Relatively subtle differences in fringe pattern then give rise to a Moire fringe indicative of the flaw. This technique works reasonably well in the laboratory, but is not very convenient for routine testing procedures because of the difficulty in attaining identical boundary conditions and loading in the two interferograms. We have found that excellent results can be obtained on many flaw configurations by forming a Moire pattern between two transparencies of a single interferogram of the flawed component under test. A good example is shown in the accompanying figures.

Fig. 49 is a photograph of a double-exposure holographic interferogram of a "flawed" aluminum plate. It contains two flaws, one which is oriented parallel to the basic fringe system and one which is oriented perpendicular to it. Although the presence of both flaws can be detected in this figure by very careful inspection, the one which is oriented radially is much easier to detect than one which is oriented circumferentially. Fig. 50 is a Moire pattern in which the presence of the flaws are made much more obvious than in Fig. 49. This Moire pattern was formed by overlaying two transparencies of the fringe pattern shown in Fig. 49. One of these transparencies is slightly magnified with respect to the other. In essence the Moire fringes are displays of the radial derivative of normal deformation. Note that in a sense Figs. 49 & 50 are complementary in that the flaw which is difficult to detect in Fig. 49 is quite evident in Fig. 50, and vice versa.

Fig. 51 is yet another example of the Moire technique which clearly shows that not only the presence of flaws, but also their orientation, shape and size can be estimated. This is formed by overlaying transparencies of a "flawed" and an "unflawed" disk subjected to the same differential load.

The work conducted during this year is a logical extension of the work carried out during the preceding year. In particular, the areas of investigation were suggested by the results of our evaluative literature review. Although this experimental research program is modest, the experience being gained in it, coupled with the ongoing review of the field, is suggesting both new concepts and giving us insight into how one might go about setting standards for holographic nondestructive evaluation.



Fig. 49. Double-exposure interferogram of a pressurized disk with two flaws: one oriented parallel to the circumference (in the upper half of the disk) and one oriented radially (in the lower half of the disk).

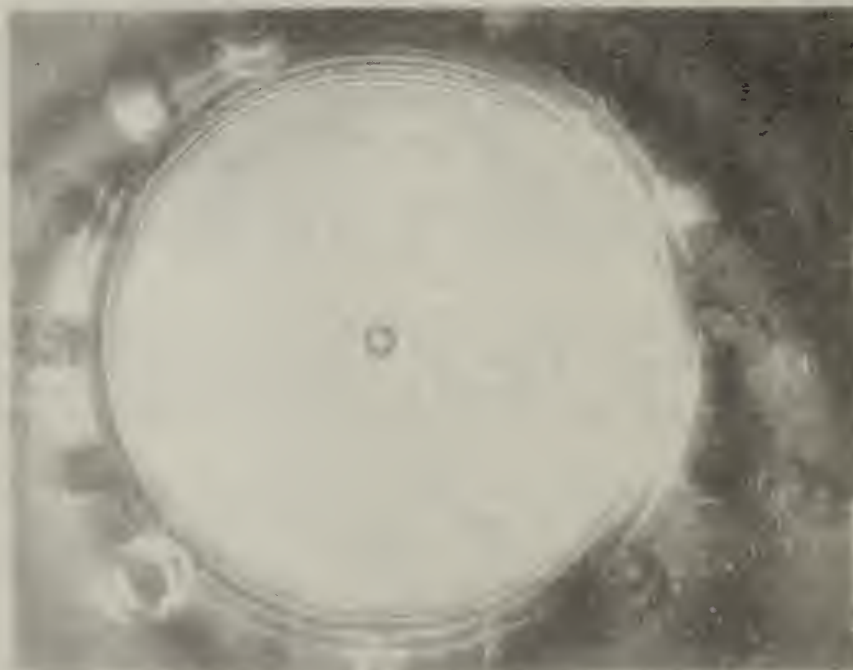


Fig. 50. Moiré pattern formed by overlaying the pattern of Fig. 1 with a slightly magnified transparency of the same pattern.

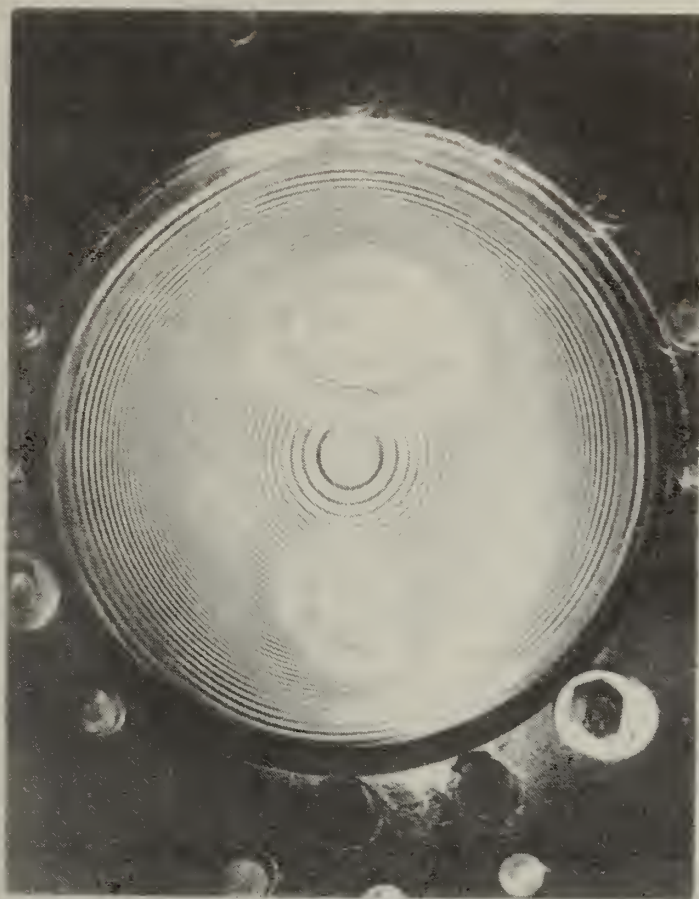


Fig.51 . Moiré patterns formed by overlaying transparencies of interferograms of a flawed and an unflawed disk.

INFRARED METHODS OF NONDESTRUCTIVE TESTING

J. Cohen

Radiometric Physics Division

Center for Radiation Research

Infrared methods of nondestructive testing, especially thermography, are of widespread and increasing importance in industry. This is a newly established project, begun in March 1982, for the threefold purpose of 1) developing expertise and maintaining an awareness of these methods as they are practiced in industry; 2) evaluating the current and future needs for standards and traceability for these methods; and 3) assessing the Bureau's role in this area.

The work on this project thus far has been concerned with developing the necessary expertise and has been concentrated on thermography and thermal imaging systems, including their performance measures. Thermal imaging systems are complex, being comprised of diverse, interacting subsystems such as optical systems, mechanical-optical scanning systems, infrared detector, signal processing, and display apparatus. The thermogram, or visual display of an infrared target, depends on the thermal and spatial characteristics of the target and its surroundings, as well as on the imaging system per se, thus the desirability for standardized testing of performance measures. Further, a given test condition may enhance one particular performance measure, while degrading another performance measure, e.g., increasing detector field of view increases temperature sensitivity, but may decrease spatial sensitivity. Then the values of both performance measures, not just one, should be disclosed. The writing of a Technical Note, "Elements of Thermography for Nondestructive Testing", has begun.

In the future, studies of other infrared methods of nondestructive testing will be undertaken. Also, ASNT and ASTM have just recently established committees on the title subject, and the principal investigator intends to become involved with both groups.

EVALUATION OF ORGANIC COATINGS PERFORMANCE ON METALLIC SUBSTRATES
USING INFRARED THERMOGRAPHY

M. E. Knight and J. W. Martin
Building Materials Division
Center for Building Technology

A rapid, nondestructive testing procedure using infrared thermography is being developed for detecting corroded areas at the steel/organic coating interface and for detecting blisters under the organic coating. The organic coating can be clear or pigmented and the substrate can be smooth or sandblasted. Defects, visible or invisible to the human eye, are detected provided that the thermal properties (e.g., emissivity, thermal conductivity) of the defected area differ from that of the background.

Experimentally, the procedure is 1) to uniformly heat the test specimen to a temperature greater than ambient and 2) to measure the emitted thermal energy using an infrared thermographic camera. In our case, the test specimens were heated to 45-55°C from the backside using a collimated light source. A temperature uniformity of greater than 0.5°C was maintained across the panel. The camera used in this study has a 2-5.6 micron detector with a temperature resolution of 0.2°C, at 30°C. The spatial resolution is 1 mrad.

In determining the defect resolution of the camera, various types and sizes of defects were artificially fabricated on smooth and sandblasted steel substrates. There were four types of defects that the procedure could detect: 1) corroded areas under intact films, 2) corrosion which had erupted through the film, 3) water-filled blisters, and 4) air-filled blisters. Minor organic film irregularities (e.g., thickness variations in the film) were not detectable. Panels with localized areas of corrosion under intact films were prepared by placing drops of dilute KHSO_4 solution, having various controlled diameters, on clean steel substrates. As the solution dried, red iron oxides formed at each doped location. The panel was then coated. Water-filled blisters were formed using the same procedure as before except that after the coating was cured, the panel was immersed in distilled water. Air-filled blisters were prepared by contaminating small areas of the substrate with a mold release. The panel was then coated. After the coating had cured, a syringe was used to introduce air under the coating. The coating thickness for all defect types was between 25 to 100 microns.

The presence of a defect is observed as varying grey levels on the cathode ray tube output. Corrosion under intact films and water-filled blisters appear hotter than the background; air-filled blisters and corrosion which has erupted through the film appear cooler than the background. With the equipment available in this study, defects having diameters close to 0.5 mm were detectable on smooth substrates. On 50 micron sandblasted panels, defects having a diameter greater than 1 mm were detectable.

From a practical standpoint the procedure has already demonstrated its utility as an evaluation tool for coating performance. Several steps are being explored to increase its usefulness as both a quality control device and for studying interfacial corrosion. These include 1) computer image analysis of the thermographs, 2) improved spatial resolution, and 3) improved temperature resolution.

SMALL-ANGLE NEUTRON SCATTERING FACILITY

C. J. Glinka

Reactor Radiation Division

Center for Materials Science

A new facility for small-angle neutron scattering (SANS) has, within the past year, become fully operational at the NBS Reactor. The new facility performs measurements at smaller angles (thus allowing studies of larger structures) and with data rates up to 50 times faster than the instrument it replaces. This enhances the ability of researchers to study the microstructure of materials such as metals, ceramics, glasses, polymers, biomaterials, and magnetic materials much more effectively and in greater detail.

The NBS SANS instrument can be used to study structural features with sizes ranging from about 10 to 5000 Å, a regime of vital importance to understanding the behavior of real engineering materials. In this size regime, neutron scattering provides information which is complementary with that obtained by electron microscopy or analogous x-ray methods. The SANS technique affords the added advantages that the measurements are inherently nondestructive and may be made on relatively thick specimens or on samples in specialized environments owing to the highly penetrating nature of neutron radiation. The derived information is thus characteristic of the bulk material and can be correlated with bulk measurements carried out, in many cases, on the very same samples. This new SANS facility is expected, therefore, to play an important role in the nondestructive investigation of materials properties.

Figure 52 shows a schematic layout of the SANS facility. The instrument utilizes a direct beam from the Reactor which is filtered by beryllium and single-crystal bismuth, then passed through a mechanical velocity selector, to achieve both low background and tunability of the mean wavelength from 4 to 10 Å. The beam is collimated by a series of masks, having nine apertures each, aligned along an evacuated 4.5 m flight tube preceding the sample. The effect of the masks is to produce nine independent beams which converge to a point at the center of the detector thereby increasing the beam area at the sample by nine without degrading the instrumental resolution. The detector is a 65 x 65 cm position-sensitive proportional counter with a resolution of 5 mm in both directions. The detector may be positioned at either 2 or 3.5 m from the sample at the end of an evacuated flight tube which can be rotated about the sample position to reach larger angles. Measurements can be made at scattering vectors as small as 0.003 Å^{-1} in fluxes ranging from 10^4 to $5 \times 10^5 \text{ n/cm}^2\text{-sec}$, depending on the collimation and choice of wavelength.

The sample area at the instrument is large enough to accommodate equipment such as furnaces, cryostats, magnets, or deformation devices, for example, so that the scattering can be monitored as the sample environment is changed. A computer-controlled sample changer is also available for ambient measurements which enables up to four specimens to be examined automatically.

An interactive color graphics display terminal linked to a high-speed computer is available at the facility for the direct imaging and detailed analysis of SANS data. Software has been developed which enables quantitative results to be obtained on-line to allow true interactive experimental design.

A number of cooperative research projects have already been initiated with the Metallurgy, Polymers, and Fracture and Deformation Divisions at NBS as well as with other government and industrial laboratories and universities. In the area of nondestructive evaluation, R. Fields and S. Singhal of the Fracture and Deformation Division have made measurements to detect creep-induced voids in stainless steels (see p. 132).

NBS SANS SPECTROMETER

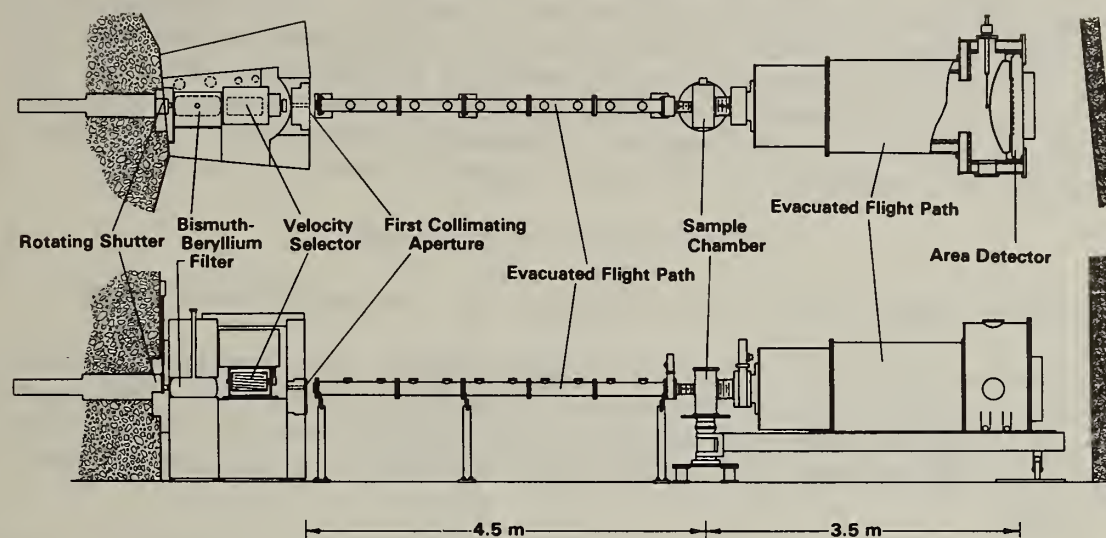


Fig. 52. Small Angle Neutron Scattering Facility.

INVESTIGATION OF SiC-Al COMPOSITE MATERIAL BY NEUTRON SCATTERING

H. A. Alperin, Reactor Radiation Division

S. P. Singhal, Fracture and Deformation Division

Center for Materials Science

We have investigated the feasibility of using neutron diffraction as a tool for the nondestructive evaluation of composite materials. The material selected, SiC fibers in an aluminum matrix, is ideal for this purpose due to the very low aluminum neutron absorption cross section. This makes it possible to observe (111) Bragg reflections from both the fibers and the matrix. Upon application of increasing compressive stress to a cylindrical sample (~ 1 cm diameter) while it is undergoing neutron scattering measurements, it is possible to accurately measure the change in d-spacing (strain) as a function of applied stress (σ) independently for both the matrix and for the fibers.

$$\Delta d/d = -\nu\sigma/E = -\Delta(2\theta)/2\tan\theta$$

Other bulk measurements only give an average for the composite as a whole.

The required accuracy of the measurement derives from the ability to fit a known function (Gaussian) to the neutron lineshape. With sufficient counting statistics (~ 4 hrs for each peak scan) the fit yielded peak positions to an accuracy of $\sim \pm 0.001$ degrees (2θ) which gives a change in d-spacing accuracy of $\sim \pm 1 \times 10^{-4}$ A.

The results are shown in Figure 53. For comparison, an identically-shaped rod of 6061 Al was also measured. From the slope and assuming a Poisson ratio $\nu = 0.31$ a Young's modulus $E = 10.9 \times 10^6$ psi (7.5×10^4 MPa) is obtained; this is very close to the value (10.5×10^6 psi) usually quoted for an Al alloy. The stiffening of the Al matrix in the composite is apparent from Figure 53 and gives the value $E = 19.5 \times 10^6$ psi. The SiC fibers show a value $E/\nu > 300 \times 10^6$ psi.

Several interesting effects are also observed. One is a relaxation effect observed in the fibers upon repeated measurements over a period of 8 hours at a constant value of stress. The range of variation in d-spacing due to this effect is shown by the cross-hatched bars in Figure 53. Another effect is the large initial stiffness shown by both the matrix and the fibers. Neither of these effects are observed in the Al alloy sample.

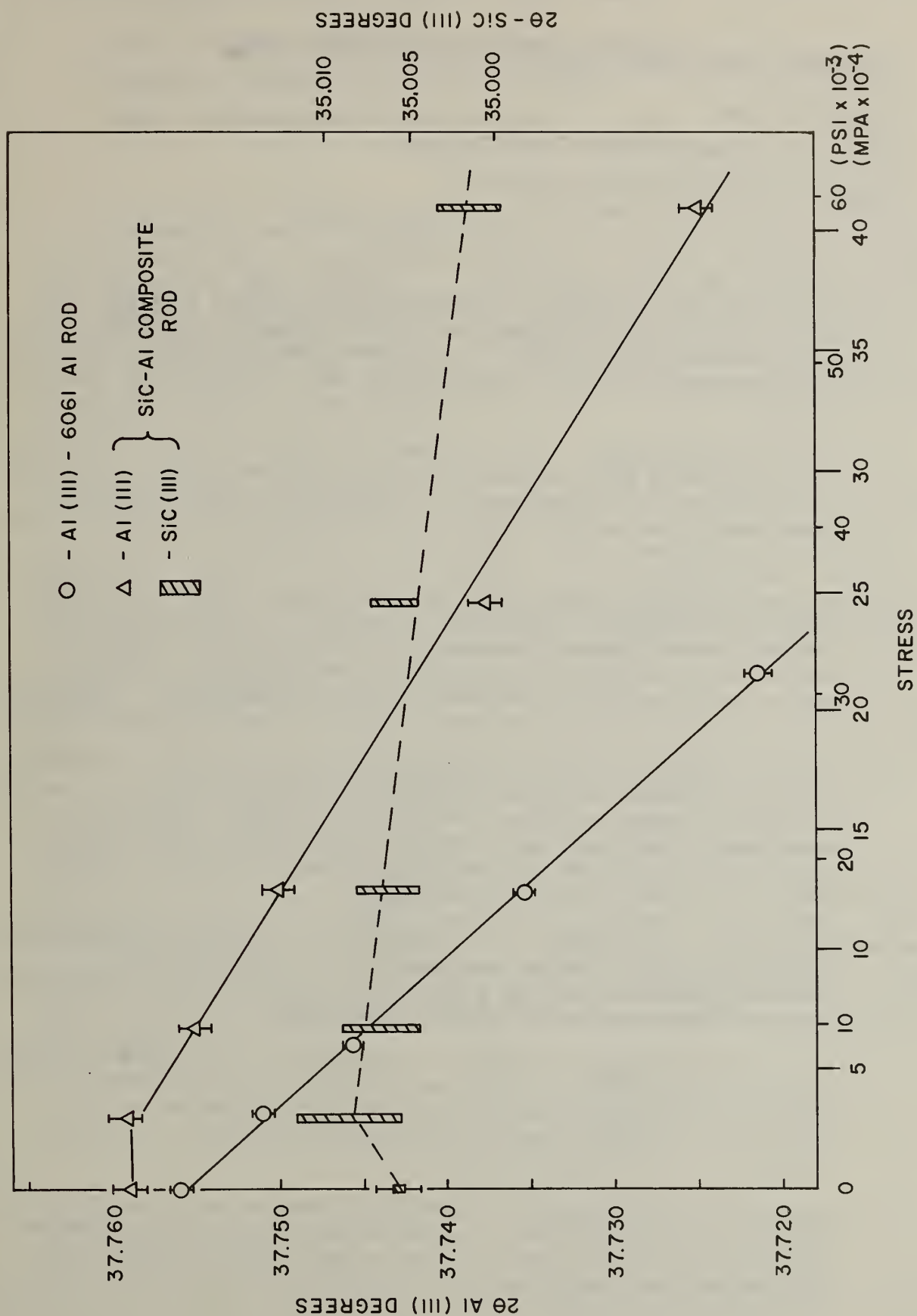


Fig. 53. Investigation of SiC-Al Composite Material by Neutron Scattering.

ULTRASONIC APPLICATIONS TO NDT AND MATERIALS EVALUATION

Gerald Blessing

Mechanical Production Metrology Division

Center for Manufacturing Engineering

1. Titanium Billet Integrity: A large titanium billet, destined to be part of the payload for NASA's Galileo mission, was ultrasonically interrogated for the extent of a surface-appearing crack. Depth and profiling showed that the crack extended most of the billet length at its center.
2. Bridge Weld Specimens: The Department of Transportation provided a series of bridge weld specimens for an evaluation of their integrity. The specimens were ultrasonically scanned with longitudinal and shear waves to especially study (a) fusion line quality and (b) base metal laminations.
3. Ultrasonic Calibration System: The performance of a new ultrasonic system consisting of a commercially available pulser/receiver unit and an externally added tuning box was compared with a previous generation system that still serves as the industry standard for reference block calibration work. It is important that a substitute for the older system be developed since it is no longer manufactured.
4. Surface Roughness Effects on Ultrasonic Echo Amplitude: The effect of sample surface roughness on ultrasonic echo amplitude was studied in a set of seven controlled-roughness steel disks. The echo amplitude was monitored as a function of ultrasonic frequency from 1 to 20 MHz, for both wet and dry back surface conditions. This is part of a current ASTM round-robin study.
5. Sound Speed in Strontium: The Geophysical Institute of Alaska needs to know the shock speed in strontium used as a liner in its shaped-charge devices. The compressional and shear sound speeds were measured for an evaluation of that shock speed.
6. Elasticity of Tungsten Carbide: A need arose in the Temperature and Pressure Measurements and Standards Division of NBS to measure the elasticity of tungsten-carbide used as the piston material in a piston-gauge pressure sensing device being developed as a primary standard for pressure measurement.
7. Composite Rod Wave Speed: An industrial need arose for determining the wave propagation speed in an 80 percent glass fiber reinforced polyester matrix composite rod used in well digging applications. The compressional wave speed was measured for an evaluation of the Young's mode rod speed.

AN ULTRASONIC RESIDUAL STRESS REFERENCE SAMPLE

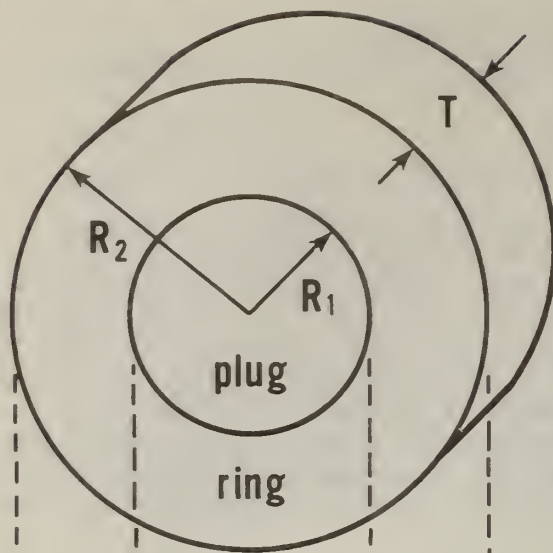
Gerald Blessing, Nelson Hsu and Thomas Proctor
Mechanical Production Metrology Division
Center for Manufacturing Engineering

The need for a reliable technique to evaluate a material's residual stress nondestructively is widely recognized. While ultrasonic elasticity or velocity measurements are frequently applied to such an evaluation, meaningful measurements are very difficult. A significant part of that difficulty is the lack of a sample with a known stress state. To satisfy that need for a reference sample, we have taken the approach of fabricating a ring-plug shrink-fit disk assembly. Figure 54 illustrates the design and summarizes the stress distribution. Its advantages are that it possesses a well-defined stress state which is theoretically tractable, is simple to fabricate, and is amenable to other stress analyses.

In our work to date, the propagation rate of ultrasonic longitudinal and shear waves has been studied in an aluminum alloy ring-plug disk. Relative longitudinal wave speeds across the disk diameter have been shown to be in quantitative agreement with calculated residual stress levels, assuming literature values for the acousto-elastic coupling coefficient. Relative shear wave speeds were in qualitative agreement with the theory, quantitative comparisons having not been made for want of the appropriate acousto-elastic constants. These results on the stressed disk have been compared to those obtained on a like-dimensional sample of the same material, constructed without the addition of internal stresses. This manner of determining the reference sound speed for zero stress is straightforward, but requires careful interpretation for the effects of material texturing and inadvertent stresses.

This work represents our initial efforts to develop an ultrasonic residual stress reference sample. In order to provide a quantitative interpretation for our shear results, the appropriate acousto-elastic constants need to be determined. We would like to experimentally verify the theory which shows that the unstressed sound velocity may be obtained by a weighted average of the sound speed over the stressed disk volume. This would represent a significant step forward in determining a material's absolute stress value. Plans also include fabricating and testing specimens of other materials, especially steel, which is of great practical interest. Finally, more precise and repeatable measurement techniques are being studied for this application.

(a) shrink fit disk



Design parameters

- Material properties
Young's modulus E
Thermal expansion Q

- Geometry

Thickness T

Plug radius R_1

Disk radius R_2

Differential radial interference Δ

Computed parameters

$$P = \frac{E(R_2^2 - R_1^2)\Delta}{2R_2^2}$$

$$A_1 = \pi R_1^2$$

$$A_2 = \pi (R_2^2 - R_1^2)$$

Stress distributions

- In plug

$$\sigma_{rr} + \sigma_{\theta\theta} = -2P$$

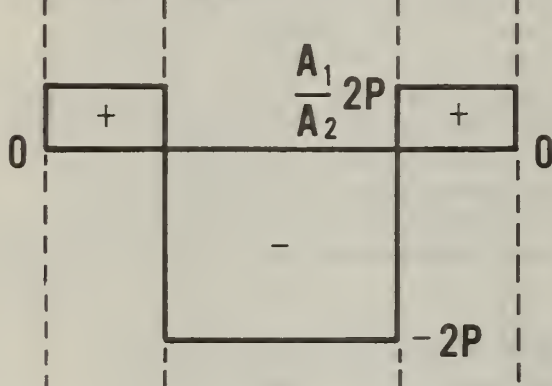
$$\sigma_{rr} - \sigma_{\theta\theta} = 0$$

- In ring

$$\sigma_{rr} + \sigma_{\theta\theta} = \frac{R_1^2}{R_2^2 - R_1^2} \cdot 2P = \frac{A_1}{A_2} \cdot 2P$$

$$\sigma_{rr} - \sigma_{\theta\theta} = \frac{R_1^2 R_2^2}{R_2^2 - R_1^2} \cdot 2P \cdot \left(\frac{-1}{r^2} \right)$$

(b) $(\sigma_{rr} + \sigma_{\theta\theta})$ distribution



(c) $(\sigma_{rr} - \sigma_{\theta\theta})$ distribution

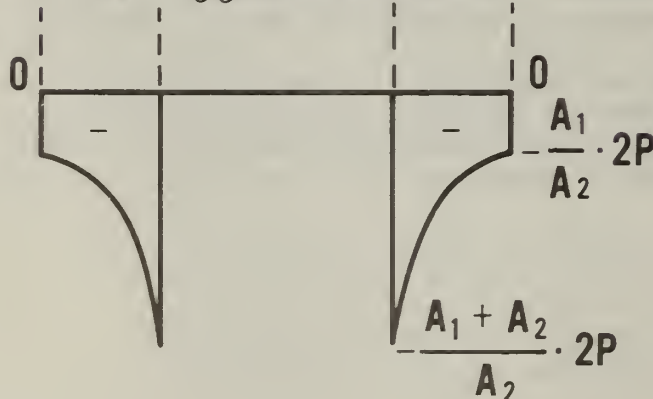


Figure 54. (a) The design parameters for the shrink fit disk; and the computed parameters and stress distribution for (b) the sum of the principal stresses sensed by longitudinal waves, and (c) the difference of the principal stresses sensed by shear waves.

NDE CHARACTERIZATION OF THIN STRUCTURALLY MODIFIED SURFACE LAYERS
ON BULK SUBSTRATES

M. Rosen, F. Nadeau, and R. Mehrabian

Metallurgy Division

Center for Materials Science

Laser and electron beam irradiation techniques are being applied extensively for the modification of properties of the surfaces of metallic structures. High intensity power transfer onto the metallic surface produces a liquid pool that rapidly solidifies under the influence of the chilling effect of the cold substrate. Formation of hard martensitic layers on a soft pearlitic bulk, solid solution strengthening of the peripheral layer, grain size refinement, dispersion hardening or formation of an amorphous layer on a crystalline substrate can be achieved by laser or electron beam heating. Of particular interest, from both technological and scientific points of view, are the physical and mechanical properties of the modified surface layer, as well as its dimensions. In most instances, the thickness of the modified layer is not accessible to nondestructive testing. However, the determination of the thickness of a case-hardened steel shaft may be of prime importance for engineering design. Similarly, it is of interest to characterize the process of amorphous glazing on a crystalline substrate. The physical properties of the amorphous layer and its depth may be important parameters for the evaluation of the efficiency of the glazing process and determination of the strength of the modified layer.

Microstructural modification in peripheral layers of bulk specimens was obtained by means of rapid heating and cooling with an electron beam. Relatively thick amorphous layers (about 1mm) were obtained on crystalline PdCuSi. In addition, martensitic and bainitic microstructures were produced on pearlitic steel plates. The NDE characterization is being made by measuring the Rayleigh surface wave velocity. Therefore the metallurgical characteristics and the thickness of the modified layer can nondestructively be determined.

The essence of this research was to develop a technique by which Rayleigh surface waves may be launched. The Rayleigh waves propagate within the surface layer only penetrate the substrate at specific wave frequencies. The Fourier analysis of the frequency content of the Rayleigh waves allows determination of the thickness of the layer provided its elastic moduli differ by several percent from those of the crystalline substrate.

NONDESTRUCTIVE EVALUATION OF COMPOSITES

H. M. Ledbetter, J. C. Moulder
Fracture and Deformation Division, Boulder
Center for Materials Science
and
S. K. Datta
Department of Mechanical Engineering
University of Colorado

Detection of low damage levels in composites is a serious, unsolved technological problem; appropriate, reliable nondestructive methods do not exist. Although conventional ultrasonic NDE techniques have proven successful at detecting macroscopic damage such as delaminations, large cracks, or bubbles, this type of damage is not likely to occur in a composite material until perilously close to failure. This situation contrasts sharply with the usual behavior of flaws in metals, where a period of slow, steady crack growth may be expected before the integrity of a structure is threatened. Thus, methods are required for quantitatively characterizing microscopic damage throughout a composite, as opposed to severe localized damage. Internal friction, which is a gauge of energy dissipation within a material, should be sensitive to this type of damage, particularly at low frequencies where the wavelength is comparable to specimen dimensions.

Last year we reported the results of low-frequency measurements of Young's modulus and internal friction for specimens of uniaxial HMS/934 graphite/epoxy composite both before and after subjecting the composite to various types of mechanical deformation: tensile loading, thermal cycling to 76 K, and 10^5 cycles of tension-tension fatigue at 60 percent of ultimate tensile strength (UTS). These measurements revealed significant changes in both modulus and internal friction following mechanical deformation. Furthermore, the induced elastic-property changes were found to be time dependent; the modulus and internal friction showed a tendency to relax with time following deformation. One puzzling aspect of the results was that although tensile loading to 90 percent UTS caused Young's modulus to decrease by 1-2 percent and internal friction to increase by 20-30 percent, the effect of tension-tension fatigue for 10^5 cycles at 60 percent UTS was just the opposite: Young's modulus increased by about 1 percent, while the internal friction decreased by about 10 percent.

To provide a more complete description of this unexplained behavior, we report here the results of further studies of the effects of fatigue on Young's modulus and internal friction for graphite/epoxy composites. Two different graphite/epoxy composites were studied: HMS/934 and GY70/934, both in a $(0^\circ, \pm 45^\circ, 90^\circ)$ cross-ply lay-up. The same epoxy resin was used in both materials but the graphite fibers were different;

the gy70/934 formulation had a higher modulus but lower ultimate tensile strength than the HMS/934. Specimens in the form of circular rods 78 mm long and 3.8 mm in diameter were machined from a single block of each material.

A Marx three-component composite-oscillator technique was used to determine Young's modulus and internal friction at a frequency of about 40 kHz; the experimental apparatus has been described in detail elsewhere.(1) This technique has considerably better precision and accuracy than the vibrating-reed pendulum technique used in the previous measurements.

Young's modulus and internal friction were determined for each specimen before and after a schedule of tension-tension fatigue, usually consisting of 105 cycles at maximum stresses ranging from 40 to 85 percent of the ultimate tensile strength. Table 1 and Fig. 55 show the results expressed as the dimensionless ratio of the final value following damage to the initial value for each specimen.

The results show that the net effect of fatigue on the GY70/934 composite was to increase Young's modulus by about 2 percent and to decrease the internal friction by about 20 percent. This behavior, although unexpected, is consistent with that previously observed in uniaxial HMS/934. Contrasting with this behavior, the present results for cross-ply HMS/934 show a decrease in Young's modulus and an increase in the internal friction after fatigue. However, the changes induced in the elastic properties do not increase monotonically with applied stress as might be expected a priori. Instead, the changes in elastic properties caused by high-stress fatigue are less than the changes caused by fatigue at intermediate stress levels. Another observation arises by comparing the results for the two HMS/934 specimens fatigued at the same stress level (58.1 percent UTS) for different numbers of cycles. For these two specimens, the one subjected to only 5×10^4 cycles of fatigue showed a larger increase in internal friction than the specimen subjected to 10^5 cycles of fatigue, although the modulus of the latter specimen showed a slightly larger decrease after fatigue than did the modulus of the former specimen.

Results of these experiments suggest two competing mechanisms: one mechanism, dominant during low-stress fatigue and static tensile loading, acts to reduce the elastic modulus and increase the internal friction. The second mechanism acts during fatigue at higher stress levels and reduces the changes in elastic properties assumed to occur during earlier cycles.

This hypothesis requires further experiments for its confirmation. In particular, one should monitor both modulus and internal friction of these materials semicontinuously during fatigue to see if internal friction first increases and then decreases, as the postulated damage mechanisms suggest.

Theoretical studies

Collaborating with Prof. S. K. Datta at the University of Colorado, a general theoretical approach has been used to model composite behavior

on the basis of constituent properties. Several properties can be considered from the viewpoint of plane-wave propagation in composites with either arrayed or randomly distributed inclusions (fibers or particles). Assuming long wavelengths (longer than the particle diameter), one can derive relationships for elastic wave speeds and attenuations for both longitudinal and shear waves. These relationships contain two further assumptions: particle distribution is homogeneous and uncorrelated, and Lax's "quasicrystalline approximation" holds. This approximation is to assume that

$$\langle u_j \rangle_{ij} = \langle u_j \rangle_j$$

where $\langle u_j \rangle_{ij}$ is the ensemble average of the displacement field at the j th-scatter position, keeping the i th and j th scatters fixed in position. We have already applied these methods successfully to compute the elastic constants of fiber-reinforced boron-aluminum composites.(2) Recently, we extended the method to the anisotropic-fiber case and applied it to graphite/epoxy composites.(3)

REFERENCES

1. H. M. Ledbetter, Cryogenics 20, 1980, 637-640.
2. S. K. Datta, H. M. Ledbetter, and V. K. Kinra, in: Composite Materials: Mechanics, Mechanical Properties and Fabrication (Japan Soc. Compos. Mater., Tokyo, 1981), 30-38.
3. S. K. Datta, H. M. Ledbetter, and R. D. Kriz, Proceedings Fourth International Conference on Composite Materials, ICCM-4 (Tokyo, October 1982).

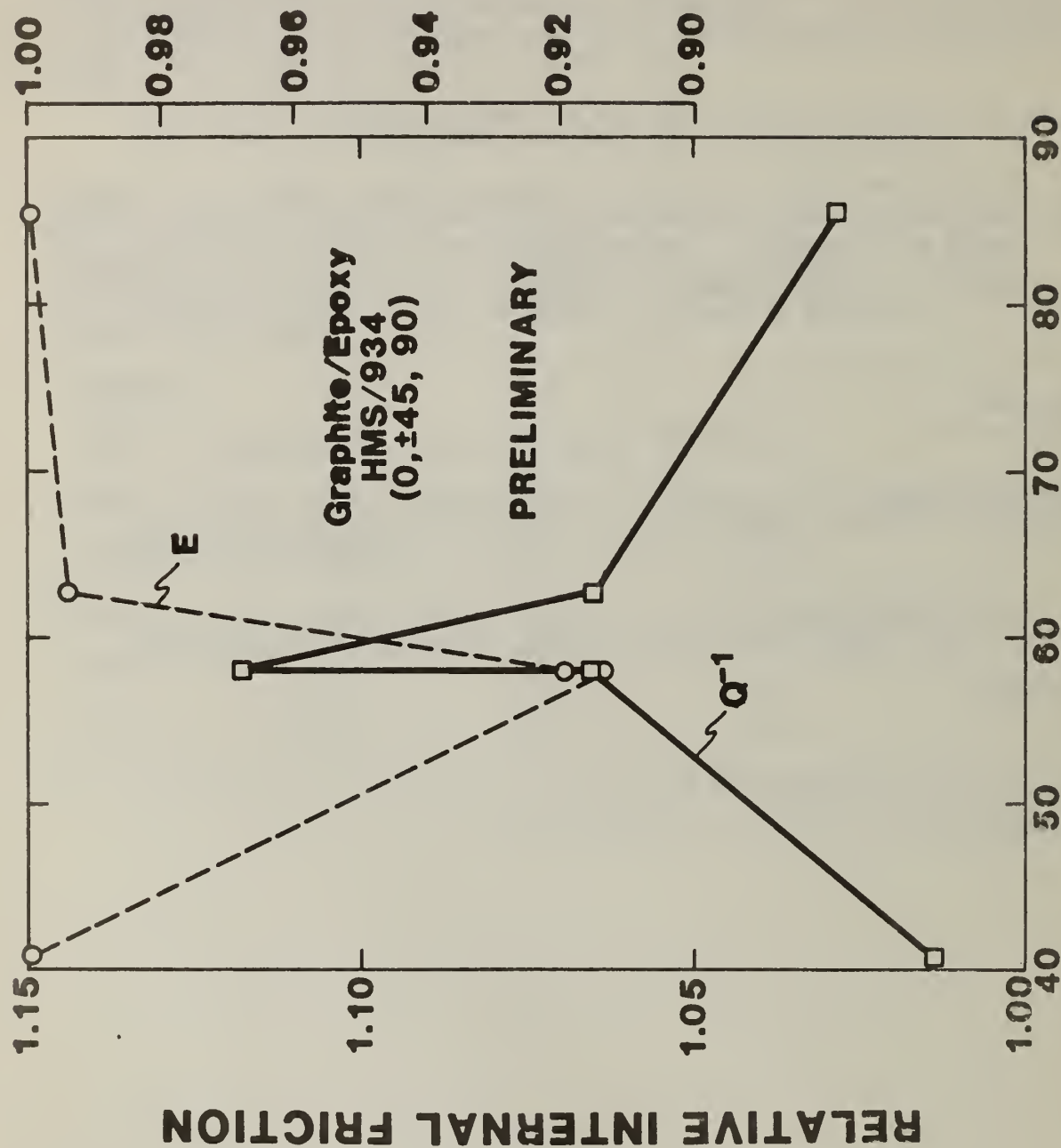
Table 1. Effects of cyclic fatigue on Young's modulus, E, and internal friction, Q^{-1} , for (0, ± 45 , 90) graphite/epoxy composites.

Material	Maximum fatigue stress (% of ultimate)	Number of cycles	E/E_0	Q^{-1}/Q_0^{-1}
HMS/934 (0, ± 45 , 90)	40.7	10^5	1.001	1.014
	58.1	5×10^4	0.919	1.118
	58.1*	10^5	0.914	1.065
	62.5	10^5	0.994	1.065
	85.6 ⁺	10^5	1.000	1.028
GY70/934 (0, ± 45 , 90)	62.0	10^5	1.022	0.803
	67.0	10^5	1.022	0.773

*Fatiguing performed at 76 K.

⁺Subsequently failed after 100,790 cycles.

RELATIVE YOUNG'S MODULUS



FATIGUE STRESS (% of ultimate)

Fig. 55. Effects of cyclic fatigue on relative internal friction, Q^{-1}/Q^{-1}_0 , and relative Young's modulus, E/E_0 , for HMS/934 (0, ±45, 90) graphite/epoxy composite.

GREEN STATE NDE

T. Negas

Center for Materials Science
Materials Chemistry Division

Mechanical failure of technical ceramics generally results from defects introduced into the finished microstructure during any stage of processing (powder-green compact-sintering). Typical flaws that are generated include voids, surface cracks, pressure (density) gradients, and inclusions, such as large grains or impurity phases. To insure structural/chemical reliability, therefore, it is imperative that these flaws be detected during processing using NDE methods.

Although NDE methods (e.g., radiography, acoustic measurements) can be utilized to examine finished ceramics for large ($> 10 \mu\text{m}$) and sub-micron defects, techniques to evaluate green compacts prior to irrevocable densification have not been developed.

This study has focussed on the feasibility of preparing green compacts containing pores ($> 10 \mu\text{m}$) and pore cluster defects. These constitute a major failure mode in densified ceramics where stress is concentrated and can interact with adjacent defects. Normally, these voids result from non-uniform packing of particulates during formation of the green compact. Potential NDE methods to detect these are being evaluated in Division 562. In addition, microcracking in one class of densified ceramics is under investigation in cooperation with Division 562.

Cylindrical green compacts (2.5 cm OD X 5 cm length, no binders) of alumina and YCrO_3 have been fabricated using reactive powders $< 5 \mu\text{m}$. These were compacted by a local commercial firm by isostatic pressing ($\sim 10,000$ psi) to avoid large density gradients. Alumina densifies to better than 98 percent of theoretical density (1500°C) while YCrO_3 requires 1750°C in a reducing atmosphere (N_2 , 10 percent H_2) to obtain > 95 percent. Attempts to introduce pore clusters in the alumina compacts are in progress. Starch, naphthalene, and latex sphere additives to this powder prior to consolidation are under investigation. All require a mild "burnout" to develop the necessary voids. The YCrO_3 compacts were pressed between 5-10,000 psi to obtain variable green densities and, hence, final densities ranging from 83 to > 95 percent of the theoretical density after sintering. These latter materials constitute a series of specimens being examined by elasticity and small angle neutron scattering measurements, in cooperation with Dr. Eldon Case, Division 562 (see below and p. 134).

Although Division 562 is evaluating potential NDE methods for ceramic green compacts, Division 561 has also worked closely through subcontract with Prof. A. G. Evans, Univ. of California, Berkeley, who suggests (formal report submitted to NBS) the use of low amplitude

acoustic waves, x-rays, and neutrons for analysis of green compacts. Presently, none are used for ceramic processing. To avoid disruption of the green compact, low frequency, acoustic waves are necessary for velocity, attenuation, and scattering measurements which could provide information on powder and void size distributions. X-ray and neutron methods also should provide similar information from differential absorption due to void spaces and inclusions.

The small angle neutron scattering (SANS) technique is now under development to detect submicron microfissures in densified YCrO_3 ceramics, although it is anticipated that application to green compacts is possible. In this method, a collimated beam of thermal neutrons of given wavelength is directed onto a specimen. The scattered and transmitted neutrons then impinge on a large array of counters. For scattering centers such as microfissures, the intensity of the scattered neutron beam is proportional to the number density (N) of the cracks, while a crack size can be derived from analysis of the angular spread of the beam.* Densified YCrO_3 ceramics have been measured with SANS, and microfissures in the 175-200 Å range have been detected. These data were successfully correlated with conventional elasticity measurements which relate N and microcrack size to elastic moduli via appropriate theory. An important feature of the YCrO_3 materials is that microcracks can be healed and re-initiated reversibly by appropriate thermal annealing without altering density or grain size. Thus, the same near-perfect and defect material can be investigated.

The SANS technique was chosen over x-rays, since a larger sample volume can be sampled. However, for the case of large pores ($> 10 \mu\text{m}$) in green compacts, our analysis indicates that most of the information will be "buried" at very small scattering angles near the neutron beam stop. Nevertheless, the SANS method offers promise for application to the processing of ceramic green compacts. With submicron sinterable powders, agglomeration (25-1000 Å) of particulates is a significant problem during compaction and sintering. Intra-agglomeration porosity tends to be very fine, while interagglomerate porosity can be in the $<< 10 \mu\text{m}$ range. Differential densification of partly agglomerated compacts normally results in detrimental voids or internal surfaces which cannot be eliminated during the sintering process. The SANS technique could be developed and correlated with surface area and porosimetry measurements to detect states of agglomeration, including abnormal voids ($< 5\text{-}10 \mu\text{m}$) within green compacts.

*Manuscript in preparation, "SANS and Elasticity Measurements on Microfissured YCrO_3 Ceramics", E. Case, T. Negas, and L. P. Domingues.

CRYSTALLIZATION KINETICS STUDY AMORPHOUS Zr-Cu BY ULTRASONIC AND MICROHARDNESS MEASUREMENTS

M. Rosen, F. Nadeau and R. Mehrabian

Metallurgy Division

Center for Materials Science

Metallic glass formation and subsequent crystallization upon heating has recently become an active research area. Rapidly solidified amorphous alloys exhibit a variety of desirable physical, chemical and mechanical properties that are particularly attractive for products in electronics and power industries. Moreover, functional and economic advantages may be gained when crystallizing specific alloys into microcrystalline structures that can be subsequently consolidated into bulk products. Microstructural characterization using nondestructive techniques, e.g., ultrasonics may thus be attractive both for its contribution to understanding the kinetics and mechanism of the transformation and for its ultimate application for on-line feedback control of materials processing variables.

Metallic glasses are not thermodynamically stable, and they tend to structurally relax and finally crystallize upon appropriate heat treatment. The activation energy for relaxation continuously increases with time, which may correspond to the removal of quenched-in defects. Associated with relaxation and crystallization are variations in the elastic and mechanical properties. Young's modulus E and shear stiffness μ generally increase by 20-40%, but the bulk modulus K by only about 7% upon crystallization. The density of glassy metals is generally only 0.31-1.5% less than the corresponding crystalline structures. As-quenched glasses contract approximately 0.5 volume percent during structural relaxation preceding crystallization.

Straightforward elasticity and wave propagation theories enable one to calculate Young's modulus E . For one-dimensional extensional wave propagation in a homogeneous, isotropic, linearly elastic solid, Young's modulus is given by $E = v_E^2 / p$ where v_E is the extensional wave velocity and p is density

The Cu-Zr metallic glass ribbons were prepared using the melt-spinning technique. A 2 mm wide, 30 μm thick ribbon was produced. Ultrasonic, x-ray and STEM (Scanning Transmission Electron Microscopy) examinations indicated that the ribbon was completely amorphous. The ribbons were heat treated in evacuated capsules at temperatures above the glass transition point, T_g , for different time intervals in order to obtain information about the crystallization kinetics and its mechanism.

The objective of the present investigation was to study the crystallization kinetics of Zr-Cu ribbons (about 50 μm in thickness) by means of laser-generated and piezoelectrically detected, ultrasonic waves whereby the extensional wave velocity, and consequently the Young's moduli could be

determined as a function of crystallization time. The amorphous-to-crystalline kinetics could thus be determined to a high degree of accuracy.

The inherent difficulty in measuring sound-wave velocities in thin-ribbons was overcome by developing a technique applying the load on the specimen by means of rapid deposition of energy from a single-pulse of a Q-switched Nd:YAG laser. A state of unbalanced compressive thermal stress is produced. The stress gradient propagates along the ribbon in the form of an elastic wave. The piezoelectric crystal, at a distance from the spot where the last radiation was deposited, detects the local displacement. Thus, the transit time of the propagating wave could be determined accurately by means of a transient-pulse recorder. In this work, ultrasonic extensional waves were detected using the National Bureau of Standards conical PZT transducer having a flat response between DC and 2 MHz. Signal amplification was provided by an EMI 6306 charge-sensitive amplifier powered by an EMI Power Supply Type 6396. A silicon photodiode triggered a Nicolet Explorer III digital oscilloscope so that the elastic wave could be recorded and transit times read directly from the screen of the oscilloscope. The transit times were determined to better than 1 part in 10^4 , and the source-receiver distance to within $\pm 0.3\%$. All velocity measurements were conducted at room temperature.

Small sections of each heat treated specimen were mounted in epoxy for Knoop microhardness number (KHN) measurements. To minimize anvil effects and to ensure that KHN values were taken of the bulk material, each specimen was cut perpendicular to its length vector, and then was mounted with its cut face exposed. After polishing the mounted ribbons with 0.05 alumina polishing powder KHN values were determined using a 10g load and averaging four symmetrical indentations.

The structural relaxation and crystallization effects induced by isothermal heat treatment on the room temperature ultrasonic extensional wave velocity, Young's modulus, and Knoop microhardness of Cu-Zr ribbons are summarized below.

Velocity versus log-time curves exhibited isokinetic sigmoidal behavior. Extensional wave velocity increased approximately 2.0% and Young's modulus by 4.0% due to structural relaxation. Young's modulus increased 43% upon transformation from the amorphous to the fully crystalline state. Knoop microhardness increased to a relative maximum, equal to 44-88% of the asymptotic KHN value, during structural relaxation. KHN then decreased to a minimum, due to stress relief annealing. The final microhardness rise to an asymptotic KHN value of approximately 720 kg mm^{-2} was due to crystallization of a hard, brittle equilibrium Cu-Zr phase.

Using data derived from the velocity versus log-time curves, the

activation energy for 50 % crystallization was found to be 360 kJ mol^{-1} and the n parameter from the Johnson-Mehl-Avrami equation was approximately unity. This value is consistent with one-dimensional diffusion-controlled growth.

An as-spun ribbon contains many quenched-in defects so that the glass may be viewed as having a continuous distribution of varying coordination or excess free volume. Reduced coordination in given atom complexes permits the material to undergo shear transformation without undue constraint and results in a ductile metallic glass. Heat treatment removes quenched-in excess free volume through structural relaxation. The amorphous material has a rigid close-packed atomic distribution and thus approaches the ideal glassy state. Consequently, the glass should harden and become less ductile in the relaxation regime. This behavior was indeed observed in the present study. The main contribution to hardness was attained during the relaxation of the amorphous phase.

D. L. Hunston

Task # 15770

Polymer Science and Standards Division

Center for Materials Science

In applications such as adhesives, fiber-reinforced composites, paints, coatings, etc. the polymer must be fluid in the early stages of fabrication so that the proper flow, leveling, wetting and spreading at interfaces, etc. can be achieved. The polymer must then harden by cooling, solvent loss, or chemical reactions to form a rigid material. In most cases the successful fabrication of a final product requires that associated changes in mechanical properties take place at the appropriate times and rates. It is desirable therefore to have nondestructive techniques that can monitor these changes as they occur. Unfortunately, this is generally very difficult, particularly since many of the applications involve thin films, whose mechanical properties are difficult to measure and can not usually be predicted from experiments on bulk samples.

To address this problem, an effort is being made to develop new methods for nondestructively characterizing thin films. The work to date has focused on the investigation of an ultrasonic shear wave propagation technique. A shear deformation was chosen because the shear properties of liquids and solids are very different. Ultrasonic frequencies were selected because in this range the attenuation of shear waves in many polymers is so high that a thin film can be treated as if it were infinitely thick and this greatly simplifies the analysis. The device consists of a thin strip of aluminum or quartz in which a shear wave is propagated. When the surface is coated with the polymer to be tested, the wave in the strip generates a shear wave in the coating. Although the high attenuation in the polymer makes it impossible to observe this wave directly, its generation causes changes in the wave in the strip, i.e., an increase in attenuation and a decrease in velocity measured along the strip. By examining the wave in the strip before and after the coating is applied, the shear mechanical properties of the coating can be determined. Although a quantitative evaluation requires the measurement of changes in both velocity and attenuation, it is sometimes useful simply to follow changes by monitoring attenuation.

During the last year the apparatus necessary to implement this technique has been set up and tested by examining several model polymer systems. The measurements are made using the pulse-echo technique, and to assist in the data acquisition and analysis, the apparatus has been interfaced to a minicomputer. The first samples tested were based on an epoxy-type polymer that cures by free radical initiation. Figure 56 shows a plot of attenuation vs. curing time for two formulations containing the same epoxy but with different concentrations of accelerator. The experiments clearly show that there is an initiation period prior to the onset of cure. The rate of cure influences the width of the transition while the ultimate attenuation level depends on the structure of the cured film among other factors. When the accelerator concentration is changed both the reaction rate and the induction period are altered but the ultimate attenuation level remains the same. This type of information can be crucial in designing epoxy-based adhesives and composites.

The second model system studied this year involved natural-product based drying oils that are used in some printing inks (1). Thin films of these liquids harden by polymerization when exposed to oxygen. The rate of hardening must be correct if proper performance is to be achieved. Figure 57 shows the results of a very simple test in which a thin film of the sample was placed on the quartz strip and the attenuation was monitored as a function of time. The initial increase in attenuation is rapid but eventually the attenuation approaches a limit when the film becomes fully cured. The curve in Figure 57 represents the best fit with a simple first order rate equation. Data of this type can be very helpful in optimizing the design of polymer systems.

The results to date indicate that this technique can be used to qualitatively monitor changes that occur during the liquid-to-solid transition in important polymer systems. During the next year an effort will be made to quantify this test. As part of this effort the measurement capability will be expanded to permit the determination of velocity change as well as attenuation. In addition the program will investigate the possibilities for coupling this technique with other methods such as dielectric tests so that both can be used simultaneously. The information provided by this coupling would make both measurement techniques more useful.

REFERENCES

- (1) D. L. Hunston, J. L. Rushford, W. R. Newitt, and B. A. Vaudreuil, "Rheology of Cure for Intaglio Printing Inks", Organic Coatings and Plastics Preprints, in press.

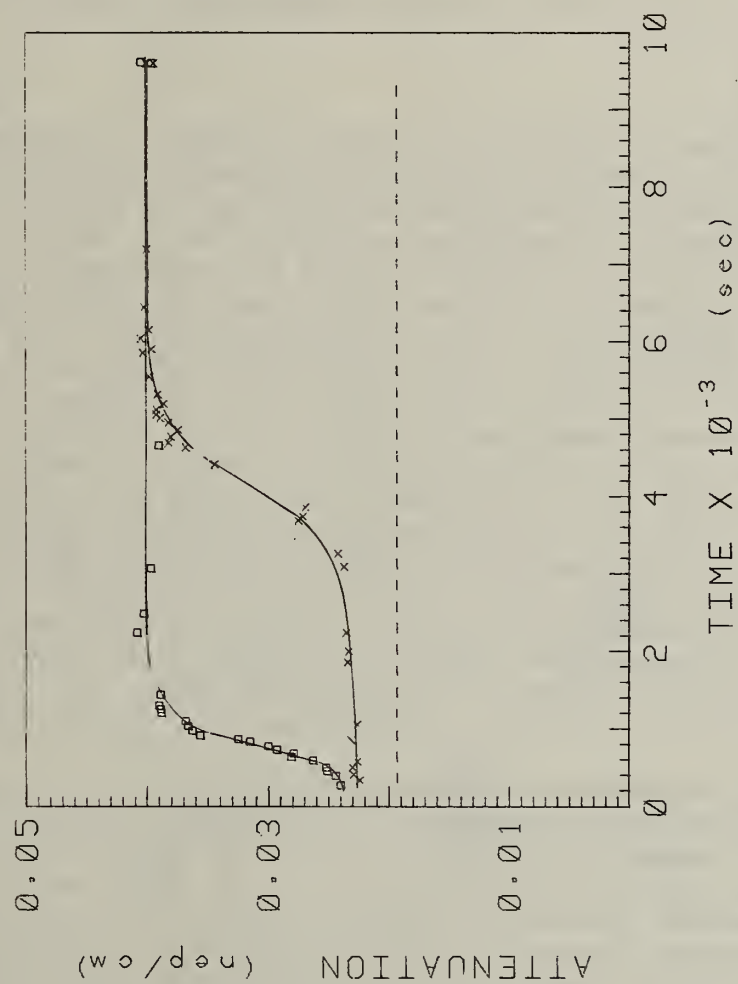


Figure 56. Cure data for the epoxy/accelerator system: dashed line for uncoated strip, X for 0.25% accelerator, and □ for 0.35% accelerator.

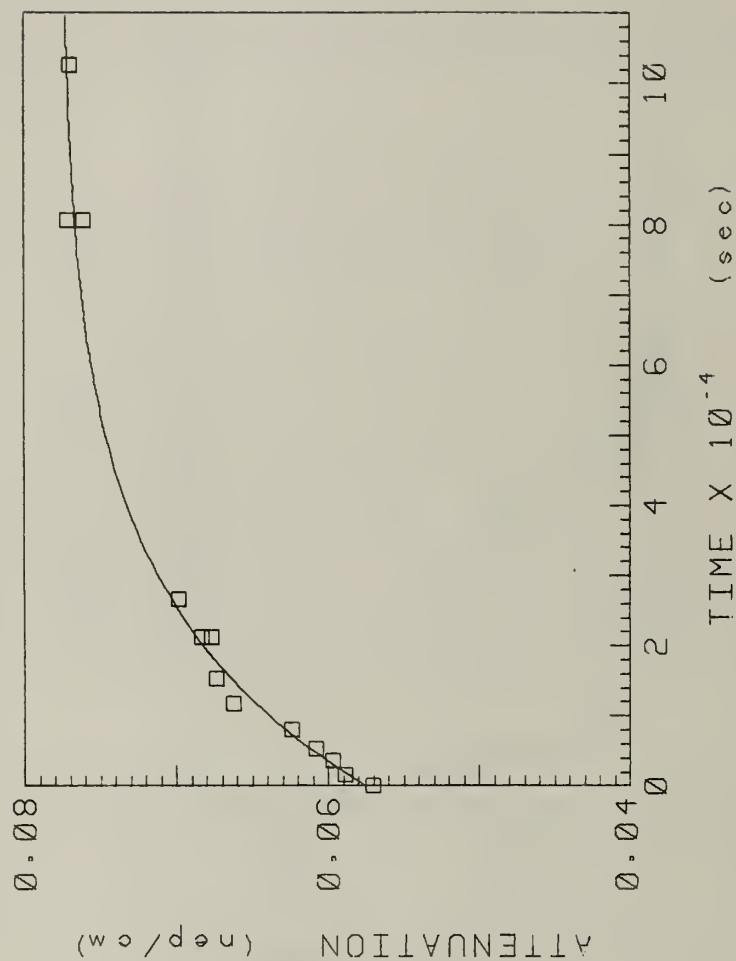


Figure 57. Attenuation vs. time plot for the curing of a drying oil based polymer system. The curve represents the best fit with a first order rate equation.

NONDESTRUCTIVE EVALUATION OF DISTRIBUTED DAMAGE

E. R. Fuller, Jr., R. J. Fields and E. D. Case

Fracture and Deformation Division

and

S. Singhal and C. J. Glinka

Reactor Radiation Division

Center for Materials Science

Introduction

In a number of instances failure of a structural component results from an accumulation of damage distributed homogeneously throughout the component as opposed to the formation and growth of a macrocrack. An example of such a situation is the nucleation and growth of creep cavities in the high-temperature components of energy conversion systems. Another example might be the accumulative damage that occurs in a composite material which is subjected to a fluctuating service stress. An important design consideration in the initial materials selection for such applications is an assessment of the material's failure life, either creep rupture or fatigue failure in the examples mentioned above. Of equal importance, however, in assuring remaining lifetime is a nondestructive assessment of the accumulative damage that has occurred to a given time (remaining) in the service life. If the state of progressive degradation in service can be periodically monitored, the rate of damage accumulation can be determined and actual component lifetime more accurately predicted. Failure due to distributed damage is not necessarily restricted to mechanical failure. In material processing, for example, it is occasionally important to assess the current microstructural status of a component (e.g. the extent of precipitation, microfissuring, sintering, etc.) before further processing is warranted.

The objective of this research program is to address these issues by an evaluation of various nondestructive inspection techniques that have potential for monitoring the extent of distributed damage in these materials. Nondestructive techniques are, in general, more desirable than destructive ones because they can be applied to actual operating components without having to replace the component after inspection. However, nondestructive techniques rarely provide direct measurements concerning the microstructural defect associated with the distributed damage. We intend to compare the results of several common nondestructive inspection techniques with direct observational measurements of the size and abundance of defects, thereby increasing the scientific base for these NDE standards. During the first year, the research effort has focused on the detection and characterization of uniformly distributed microstructural damage through the use of a new small-angle neutron scattering (SANS) facility at NBS. Two model systems have been

developed and utilized for these studies: (1) creep cavitation damage in 304 stainless steel; and (2) uniformly distributed microcracks in a polycrystalline ceramic, yttrium chromite. These studies are described separately below. The small-angle neutron scattering facility is described in a separate report by C. J. Glinka. (See p. 107.)

Cavitation Damage in 304 Stainless Steel

304 stainless steel used in high-temperature applications consists of metal carbides in an austenite matrix. The carbide-austenite interface at a grain boundary becomes a preferential site for cavity nucleation, which at elevated temperatures can be readily activated with low applied stresses by creep deformation and/or grain boundary sliding. The resulting cavities then grow, link and ultimately cause failure. The early stages of this process are extremely slow and the creep cavities, due to their small size, are not easily detectable or quantifiable. It is these early stages of nucleation and cavity growth that are examined in this research through the use of small-angle neutron scattering (SANS).

Since carbide precipitates, as well as creep cavities, give rise to neutron scattering, two requirements must be satisfied for a quantitative evaluation of cavitation damage:

- (i) The volume fraction of carbide precipitates should not change significantly during creep; and
- (ii) A reference sample with equivalent carbide structure should be measured and subtracted from the scattering spectrum of the crept sample.

The first condition was achieved in the present study by a "stabilizing" heat treatment of approximately 40 hours at 775°C prior to initiation of the creep experiments at temperatures of 600°C and below. This allowed a complete precipitation of carbide, thereby stabilizing the volume fraction of carbides. The second condition was satisfied by a reference specimen which was only heated (and not stressed) along with the crept specimen. Although a number of creep specimens were examined in this study, only two fulfilled this second requirement for a reference sample. These specimens were both crept at 600°C: one (Sample C-21) at a stress of 145 MPa (21 ksi) for 745 hours and the other (Sample C-18) at a stress of 124 MPa (18 ksi) for 789 hours. The unstressed reference samples for these specimens are designated R-21 and R-18, respectively. The neutron wavelength for these studies was 5.1 Å giving a range of scattering vectors, Q , from 0.014 to 0.16 Å⁻¹. With this range of Q , contributions from cavities and carbides in the size range of 40 to 450 Å were detected.

The detailed theory and procedure for analyzing the SANS data will be prescribed in a forthcoming publication. A few salient features, however, are described here. If scattering intensity is denoted by I , the differential

scattering cross-section is given by

$$dS/d\Omega = cI/t M T$$

where t is the sample thickness, M is the total monitor count (or scattering time), T is the sample transmission, and c is a combination of experimental constants related to the SANS facility. Creep damage is related to the difference in differential scattering cross-sections between the crept sample (C) and the reference sample (R):

$$[dS_C/d\Omega - dS_R/d\Omega] = c [I_C/t_C M_C T_C - I_R/t_R M_R T_R].$$

Accordingly, all intensities in the following discussion have been normalized by sample thickness, transmission and scattering time.

The scattering intensity for cavities in sample C-21 (i.e., $I(C-21) - I(R-21)$) is shown in Figure 58a, and that for sample C-18 in Figure 58b. A visual comparison of these figures (noting the difference in intensity scale) indicates that for most scattering vectors Q , the scattering from cavities is larger in sample C-21 than in sample C-18, thus indicating the presence of a higher volume fraction of cavities in sample C-21. A Guinier analysis can be performed on these spectra to obtain an average creep cavity size. Guinier showed that for randomly distributed, monosized, spherical heterogeneities scattering curve near $Q \sim 0$ can be approximated by the relation

$$I = I_0 \exp(-R^2 Q^2 / 5)$$

where I_0 is the intensity intercept at $Q = 0$ and R is the cavity radius. This expression is valid only when the volume fraction of cavities is small enough to avoid so called "inter-cavity interference".

Guinier plots of the data in Figure 58 give a straight line behavior only in the range for Q of 0.01 to 0.025 \AA^{-1} indicating that the cavities formed during creep cavitation have a range of sizes rather than being one size. To obtain a cavity size distribution will require further analysis, but an average cavity size has been obtained by a least-squares fit to this low Q region. The results are

$$R = 173 \pm 10 \text{ \AA} \text{ for sample C-21}$$

and

$$R = 133 \pm 7 \text{ \AA} \text{ for sample C-18}$$

Thus, sample C-21 not only has a higher volume fraction of cavities but also a larger average cavity size.

Common to various theories of creep cavitation discussed in the literature is the assumption of a two stage process involving nucleation and growth. In general, the stress level determines both the nucleation and the growth rate; whereas time under load determines the total volume fraction of cavities for that rate. For the present studies, an increase in stress by 21 MPa (3,000 psi) results in larger average cavity size and in greater volume fraction of cavities. Conclusion regarding nucleation, however, require further analyses of size distribution.

Although these analyses are continuing, numerous questions and theoretical obstacles concerning these evaluations have arisen from physical considerations. Chief among these is the fact that cavities always occur on carbides. Accordingly, it may be incorrect to assume that scattering from these two scattering species is independent and uncorrelated. Secondly, stress induced redistribution of precipitates is possible and will contribute to the apparent creep damage as deduced by SANS. This scattering component will not be correctly evaluated if the scattering cross-section is interpreted as totally due to cavities

These complications have been neglected in the past year's effort because at present we have no completely satisfactory way to treat them theoretically or to avoid their influence in 304 stainless steel. However, the analyses, which have been performed, demonstrate that SANS is sensitive to the creep damage in an engineering alloy before this damage is detectable by other techniques, even though an exact interpretation of the data is clouded for a complicated system like 304 stainless steel. Accordingly, it is our intention to better quantify the basic technique by next investigating a simple single phase system for which scattering variations will be solely due to the presence of cavities. Such a material might be copper which is known to be prone to intergranular cavitation. We may then proceed to the case of a two phase material in which no redistribution of the dispersed phase is possible. Finally, we will return to the complicated case of 304 stainless steel having, perhaps, dealt with some of the theoretical and experimental impediments to a complete analysis of the SANS spectrum.

Microcrack Damage in Polycrystalline Ceramics

Microcrack damage in polycrystalline ceramics can degrade the performance of these materials in terms of both their mechanical integrity and their chemical stability (through enhanced permeation of environmental species). Quantitative characterization of this damage is generally done with surface sensitive techniques. Research in this subtask, however, has established for the first time the powerful research tool that small-angle neutron scattering (SANS) provides for the characterization of microcracks and crack-like voids in polycrystalline ceramics. SANS has two principal advantages over surface sensitive techniques for this characterization: (1) surface preparation almost invariably damages the specimen surface,

thereby complicating the subsequent analysis; and (2) surface stresses are not necessarily the same as those in the bulk, so that surface microcrack sizes and distributions may not be representative. Research has progressed in the following three areas:

(1) Development of a "Model" Microcracking Ceramic. In order to study the nature of microcracks with an NDE probe, one must be able to distinguish the response due to microcracks from that due to other microstructural features, such as pores or second phase particles. An ideal way to separate these effects is to have a material for which the microcrack number density can be varied independently from other microstructural features. YCrO_3 is such a material. It undergoes an apparent phase transformation at $\sim 1100^\circ\text{C}$ so that it can be readily microcracked by annealing at temperatures slightly above 1100°C ; conversely, these microcracks can be diffusively healed by annealing slightly below 1100°C . Since the yttrium chromite specimens are initially sintered around 1750°C , the microstructure (porosity, grain size, etc.) changes little during these anneals thereby making YCrO_3 an ideal "model" material for studying microcracking effects in ceramics.

(2) Determination of the Nature of Neutron Scattering. Since relatively little SANS research has been conducted on polycrystalline ceramics, it is important to establish the extent of refractive neutron scattering, before interpreting scattering results as diffractive in nature, otherwise erroneous conclusion would result. This distinction can be determined experimentally by varying either the incident wavelength or the specimen thickness. In both cases, the scattered intensity versus scattering vector should not change for diffractive neutron scattering. For the microcracked YCrO_3 specimens considered in this study the neutron scattering was demonstrated to be predominantly diffractive in nature by varying the neutron wavelength between 6.25 \AA and 8.0 \AA and by comparing the scattering spectrum from specimens with a factor of five difference in thickness (See Fig. 59).

(3) Analysis of Scattering Data. Figure 60 shows the neutron scattering behavior of a YCrO_3 specimen both in its microcracked state (YT1M) and in its healed state (YT1A1). The difference spectrum is plotted in Figure 61. Since the spectrum from the healed state subtracts out the background of microstructural scattering, this difference spectrum represents only the scattering from microcracks. The solid line in Figure 61 is a least-squares fit to a model for scattering from a randomly oriented array of thin disks,

$$I(Q) = (A/Q^2) \exp(-H^2 Q^2/3),$$

where I is the scattered intensity for a given scattering vector; A is a constant; and H is the thickness of the disk. This model is an asymptotic expression for small Q values. The crack-mouth opening, H , as determined from this fit is 170 \AA , which is physically reasonable from several independent estimates of the crack opening in such ceramic systems. Further analyses for large scattering vectors indicate that the scattering is from sharp-edged objects, which is consistent with scattering from micro-pores and microcracks. Additional studies with this and other specimens with various thermal annealing treatments further support these results.

In conclusion, it appears that microcrack damage in YCrO_3 can be detected using small angle neutron scattering. Although much more work needs to be done in characterizing the microcrack size, shape and distribution, the microcrack mouth-opening displacement estimated from SANS data is in general agreement with other independent measures of crack opening. Finally, although not discussed here, a rapid method for assessing total microcrack damage might be through the use of neutron transmission measurements.

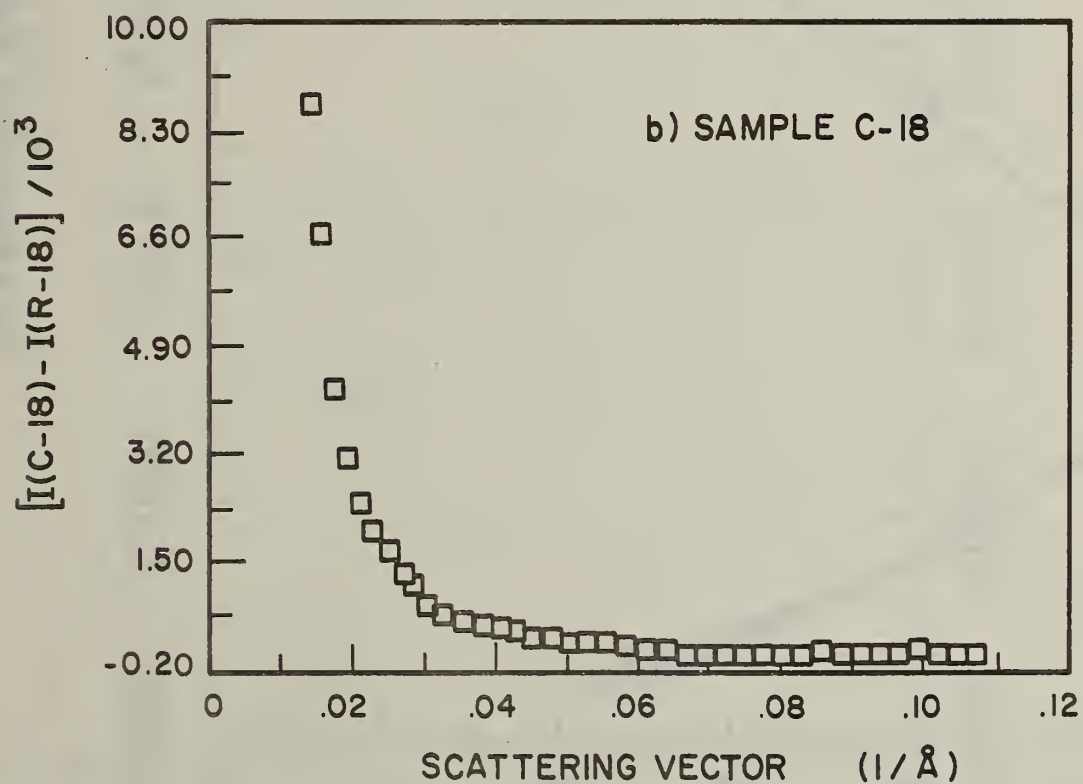
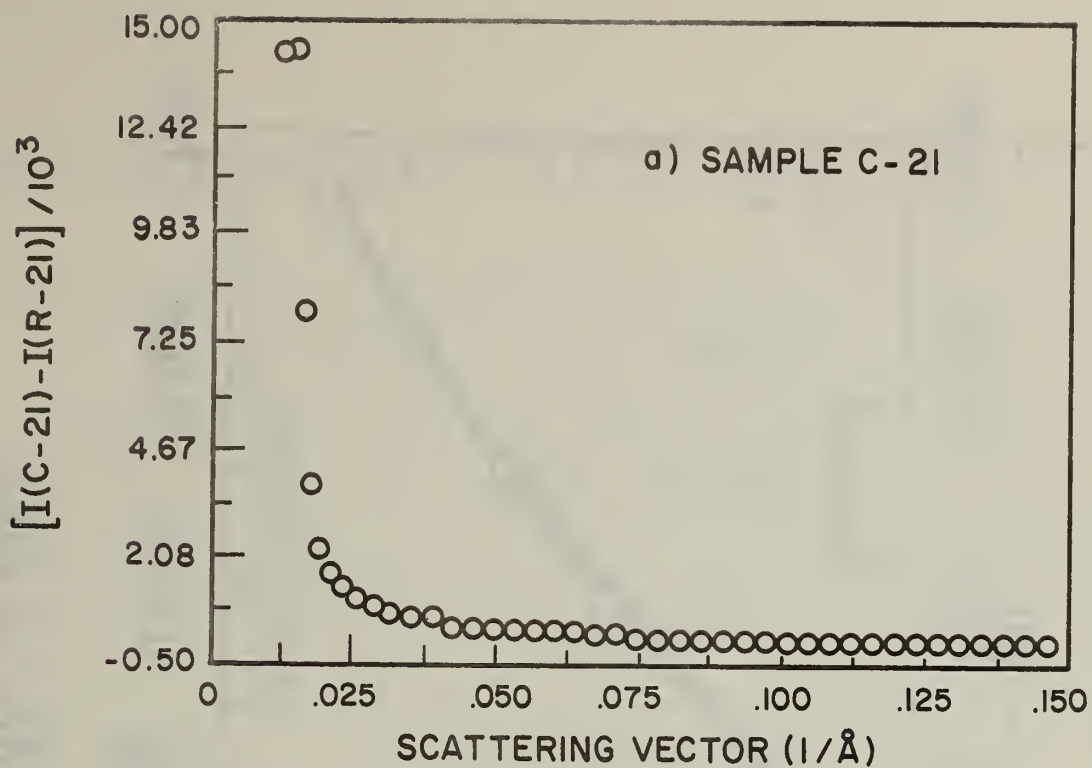
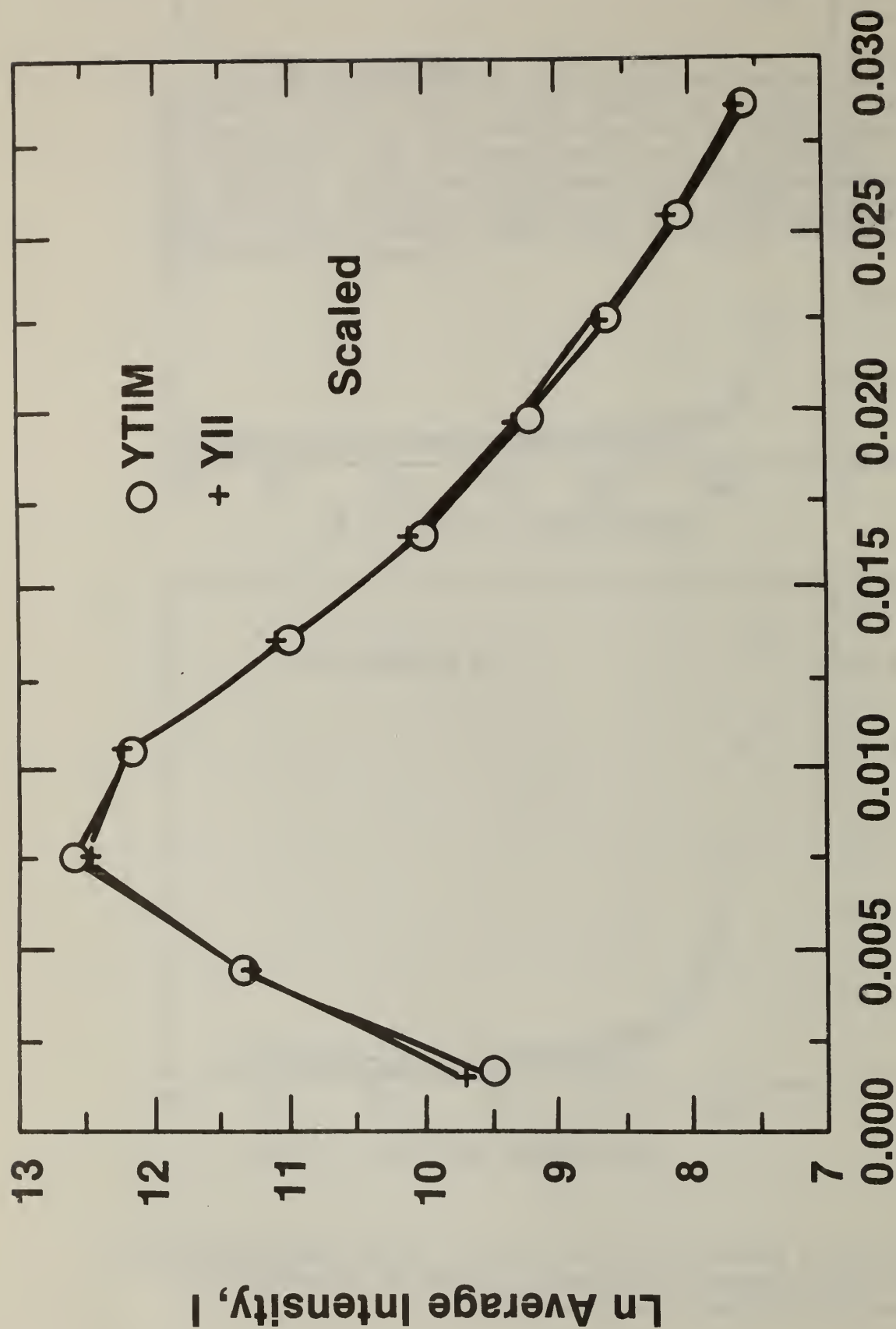
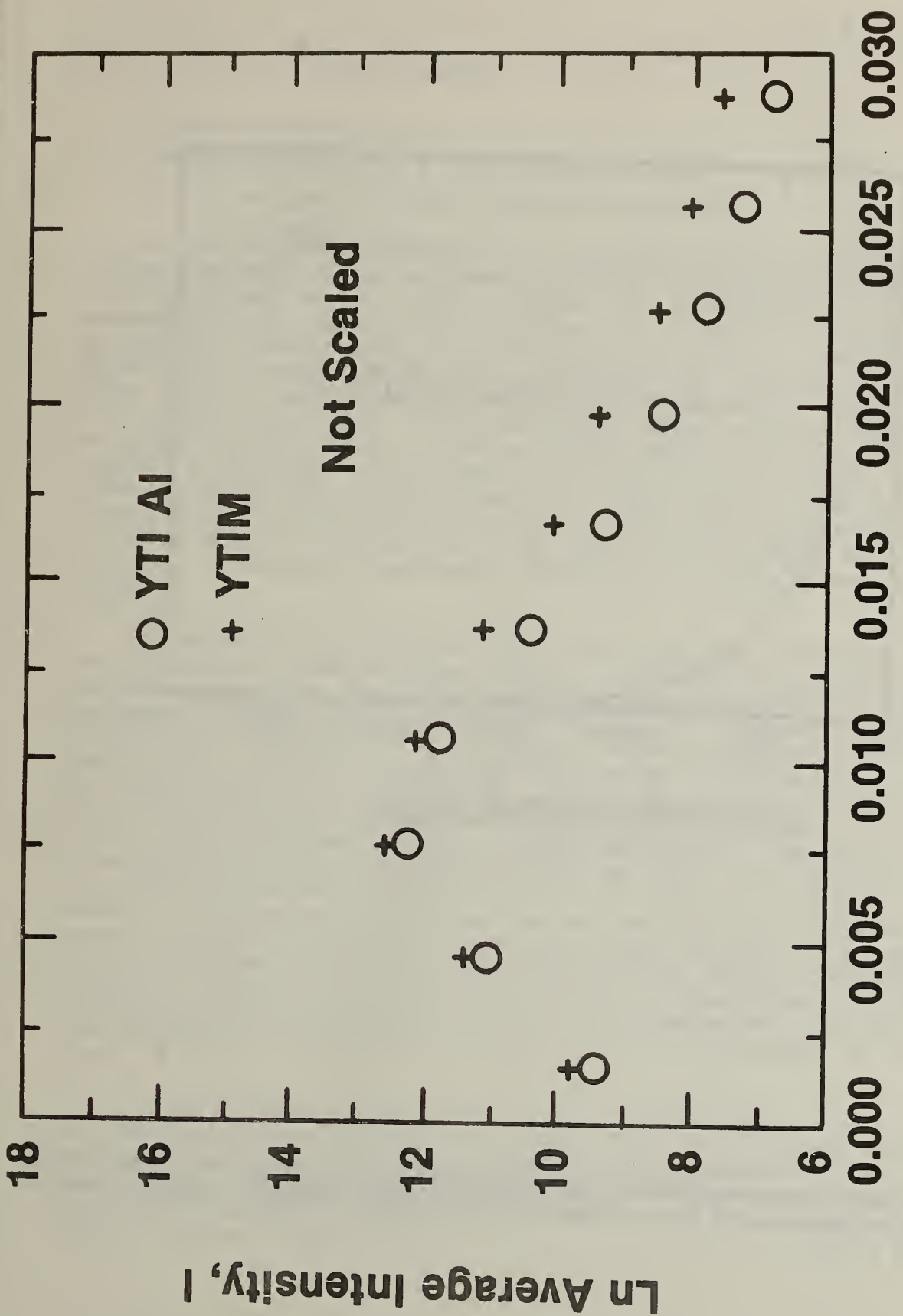


Fig. 58 Small-angle neutron scattering intensity versus scattering vector Q for creep cavities (a) in sample C-21 and (b) in sample C-18. (Note the different intensity scales.)



Scattering Vector, Q ($1/\text{\AA}$)

Fig.59 Small-angle neutron scattering intensity versus scattering vector, Q , for two microcracked polycrystalline YCrO_3 specimens of different thicknesses. Specimen YTIM is approximately five times thicker than specimen YII. Similarity between the two curves implies that scattering is predominantly diffractive in nature.



Scattering Vector, Q ($1/\text{\AA}$)

Fig. 60. Neutron scattering intensity versus scattering wave vector Q for a YCrO_3 specimen both in its microcracked state (YTIM) and in its healed state (YTIAl).

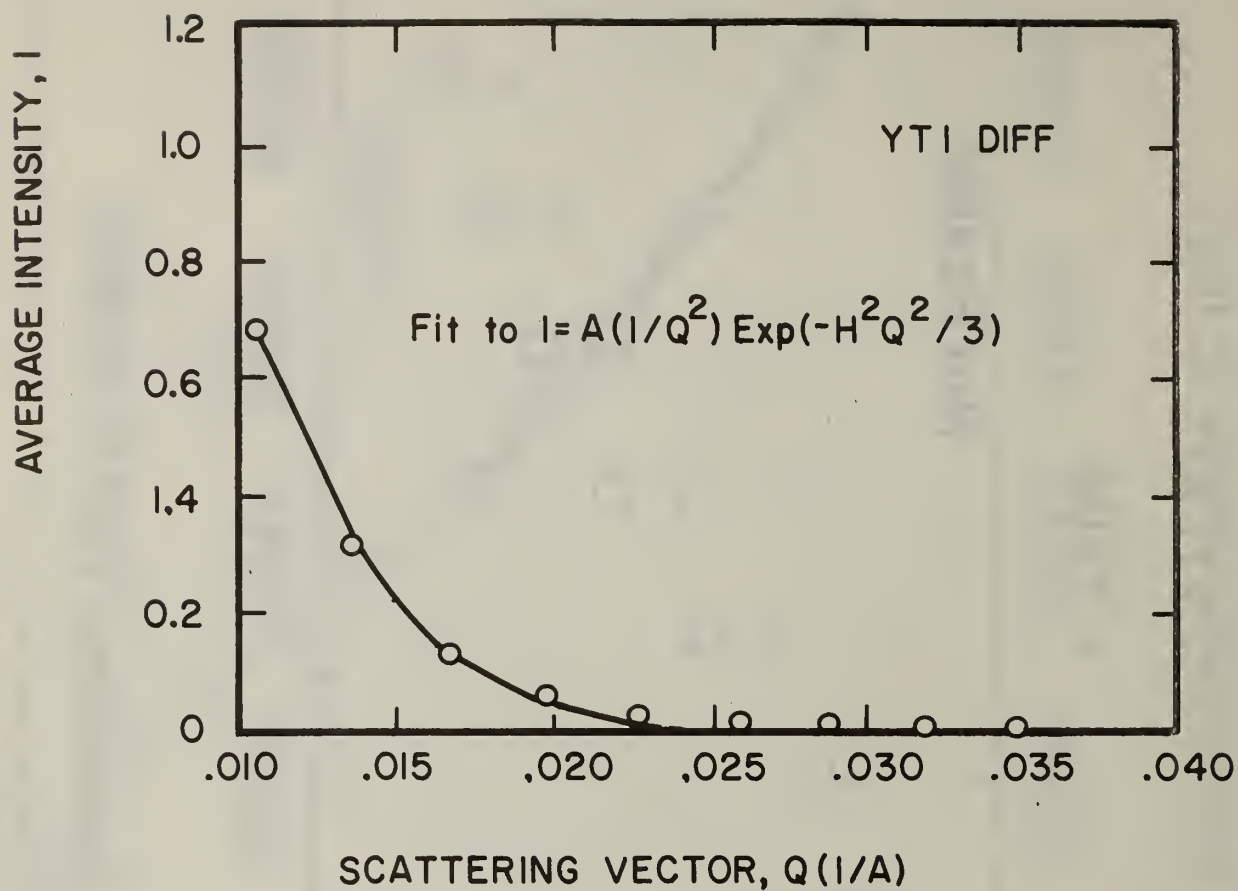


Fig.61 The difference spectrum for the scattering curves plotted in Figure 5. The solid line is a fit to a scattering model from a randomly oriented array of thin disks.

LEAK RATE REFERENCE STANDARDS

Stanley Ruthberg

Semiconductor Materials and Processes Division

Center for Electronics and Electrical Engineering

Leak rate reference standards are necessary for providing small precise flow rates of various gases for the calibration of measurement apparatus as well as for control purposes. The applications of leak measurements are steadily increasing into many segments of industry with the growth of greater product complexity and the need for greater reliability. Commercially available reference leaks are generally of two forms, capillary and permeation. Drawn capillary leaks are affected by particulates and moisture in the environment, while permeation leaks are normally restricted to helium gas and are temperature sensitive. Supplied units range in value from $\sim 10^{-3}$ Pa.m³/s to 10^{-10} Pa.m³/s (1 Pa.m³/s = 9.869 atm.cm³/s) with stated accuracies of 10-20 percent, although interlaboratory comparison has indicated up to an order of magnitude deviation (1). The object of this project is to improve the uniformity and agreement in leak rate measurements through more accurate reference standards.

Extensive consideration has been given to possible structures that could attain the flow precision required. Although porous septums are convenient and have been used, they require repeated vacuum bake out and exposure to gas flow conditions for periods of up to one year to reduce fluctuations in conductance of ~ 10 percent before stabilizing to ~ 1 percent (2). Drawn glass capillary leaks may not be desirable for the very small leak range, but specimens made earlier with entrance apertures of 1 μ m to 25 μ m diam were measured repeatedly for the 0.1 to 1×10^{-7} Pa.m³/s range and appear to have suitable stability(3). Use of such larger bore capillaries with mixed tracer-carrier gas flows and in composite structures for flow division were then considered for the range 1×10^{-6} to 1×10^{-10} Pa.m³/s. Detailed calculations on flow rate and flow mechanism were made to determine feasibility, constraints, and dimensions. The tracer-carrier gas flow procedure did not appear feasible, however, because the necessary reduction of slip and molecular flow components would require relatively large capillary diameters with high flow rates. This left flow divider as a possibility provided it could be implemented in convenient form.

Our measurements in the 0.1 to 1×10^{-7} Pa.m³/s range are made on an absolute basis with a rate-of-rise apparatus (3). The procedure selected for measurements below this range would use a flow generator for the calibration of a mass spectrometer which would then be used to measure the flow rate of a test leak. Again, guidelines for the flow generator are also derived from capillary analysis.

Calculations have now been extended on flow rate and flow composition, with selected results listed in Table I as relevant to the flow divider and to a now possible tracer-carrier mixed flow reference.

In principle the flow generator is simply a fixed, stable molecular flow conductance placed between the mass spectrometer and an accurately set pressure chamber upstream. The structure between the chamber and mass spectrometer is so designed that it has negligible effect on the value of the fixed conductance, and the conductance can be removed for independent measurement. Conductance dimensions and upstream pressure have to be restricted to allow measurement with the rate-of-rise apparatus and yet produce the desired range of known flow rate into the mass spectrometer. Box A of Table I lists one selection. Precision bore glass capillary tubing of 0.1 mm diam is readily available, easily handled, and somewhat insensitive to plugging. With a 0.2 cm length, the flow rate can be measured as a function of pressure down to the level where the conductance is molecular to greater than 99 percent. Below this value, flow rate would be determined from the upstream pressure alone. A 1 cm length would experience the same flow compositional behavior as a function of pressure but extend to smaller flow rates. Cross comparison would be made in the mass spectrometer.

A mixed gas laminar flow leak would also be restricted to a total flow rate within the range of the rate-of-rise apparatus and the mass spectrometer. Box B of Table I has several examples. The data on capillaries of 16 μm and 10 μm diam and others in this range previously cast doubt on the tracer-carrier concept because of the high flow rates and small laminar flow fraction. However, the third example shows a possibility with the long capillaries that are now available for gas chromatography. With the 100 m long, 0.250 mm diam example, the upstream pressure could be dropped to 0.25 atm to produce a laminar flow of ~ 98 percent that would be small enough to be handled by the mass spectrometer pumps. Upstream tracer gas concentrations of 1 percent to 0.1 percent would then yield a tracer flow rate of $\sim 10^{-7}$ and 10^{-8} $\text{Pa}\cdot\text{m}^3/\text{s}$ without significant fractionation. This would also be used to compare against the flow generator for greater assurance on generator use.

A flow divider is represented in figure 62. The low pressure P_1 upstream to a molecular flow leak R_2 is provided by flow through a preliminary capillary R_1 from $\sim \text{atm}$ pressure P_0 and a controlled pumpout through R_3 . Flow division is in R_2 and R_3 . A 30 cm length of 0.075 mm capillary, which is readily available, can produce a 98 percent laminar flow with small enough flow rate to be pumped by a thin, 2 mm diam orifice. With a 35 ℓ/s pump below the orifice, the geometrical conductance is the pumping speed of $\sim 3.5 \times 10^{-4}$ m^3/s . Thus, the 7.2×10^{-4} $\text{Pa}\cdot\text{m}^3/\text{s}$ flow rate through R_1 would produce a pressure of ~ 2 Pa at P_1 . At 2 Pa above a capillary of 2 cm length and 0.5 mm diam for R_2 , the flow rate for 96 percent molecular is 1×10^{-6} $\text{Pa}\cdot\text{m}^3/\text{s}$ which is readily reduced with decreasing pressure for P_1 . Note the flow ratio through R_3/R_2 is >500 . Use of a capillary

as in Box A would extend the flow range to lower values. The conductances of all capillary components can be measured independently, while the conductance of a thin orifice approaches the calculated theoretical value (4).

An ultra high vacuum mass spectrometer system has now been assembled and put into operation. The reference vacuum system for the micromanometer array has been modified, and cold trap refrigeration of the rate-of-rise pump has been repaired. The rate-of-rise system itself will provide the stable pressure generation above the flow generator capillary. A leak holder chamber and manifold has been constructed for insertion between the rate-of-rise apparatus and the mass spectrometer system.

Capillary leaks have been fabricated to dimensions similar to those in Table I, and a long chromatographic column has been procured of the dimensions of the second example in Box B of Table I for use as a mixed gas laminar flow leak. Other capillary leaks have also been drawn to serve as specimens for repeatability tests. We plan to conclude the present study with experimental measurements on capillary flow rates as a function of pressure and tracer concentration following guidelines of Table I. We also plan to intercompare the tracer-carrier mixed flow against the flow generator and determine repeatability of measurements at flow rate $< 10^{-6}$ Pa.m³/s.

References

1. "Leak Rate Reference Standards," S. Ruthberg, NBSIR 80-2162, 56-59 (1980).
2. "The Use of a Silicon Carbide Porous Plug for the Control of Gas Flow into a Vacuum System down to $1 \mu\text{l}\cdot\text{torr/s}$," R. G. Christian and J. H. Leck, J. Sci. Instrum. 43, 229-233 (1966).
3. "Leak Rate Reference Standards, " S. Ruthberg, NBSIR 82-2449, 50-53 (1981).
4. "The Measurement of Conductance to Free Molecular Flow by Substitution Procedures," S. Ruthberg, J. Vac. Sci. Technol. 9, 1457-1469 (1972).

Table I

Flow Rate and Composition of Flow for Capillary Leaks
Air, T = 298K, $P_{\text{downstream}} = 0$

	length	diam	P_{upstream}	Q	lam	slip	mol
	(cm)	(μm)	(Pa)	$\text{Pa}\cdot\text{m}^3/\text{s}^*$		%	
A.	0.2	100	266.6	$1.66(-5)^{**}$	14.0	45.8	40.1
			133.3	$7.95(-6)$	7.3	35.8	56.9
			13.3	$8.05(-7)$	0.7	6.9	92.4
			6.66	$4.05(-7)$	0.36	3.6	96.0
			1.33	$8.13(-8)$	0.07	0.7	99.2
			$1.33(-2)$	$8.13(-10)$			
	1	100	133.3	$1.59(-6)$			
			1.33	$1.63(-8)$			
			$1.33(-2)$	$1.6(-10)$			
B.	1	16	$1.013(5)$	$4.9(-5)$	92.1	7.7	0.2
		10	$1.013(5)$	$7.4(-6)$	87.4	12.1	0.5
			$2.00(5)$	$2.7(-5)$	93.0	6.7	0.2
	10^4	250	$1.013(5)$	$2.6(-4)$	99.4	0.6	0.00
			5.066	$6.7(-5)$	98.9	1.1	0.00
			$2.533(4)$	$1.7(-5)$	97.7	2.2	0.02
C.	30	75	$1.013(5)$	$7.2(-4)$	98.1	1.9	0.0
			$2.026(4)$	$3.1(-5)$	91.2	8.6	0.3
			$1.013(4)$	$8.5(-6)$	83.7	15.4	0.9
	2	500	1.33	$1.02(-6)$	0.4	3.6	96.0
			$6.66(-1)$	$5.1(-7)$	0.00	1.9	98.0
			$1.33(-1)$	$1.02(-7)$	0.00	0.4	99.6
			$1.33(-2)$	$1.02(-8)$			
	$2.5(-3)$	2 mm	1.33	$4.7(-4)$			

* $1 \text{ Pa}\cdot\text{m}^3/\text{s} = 9.872 \text{ atm}\cdot\text{cm}^3/\text{s}$

** $a(-n) = a \times 10^{-n}$

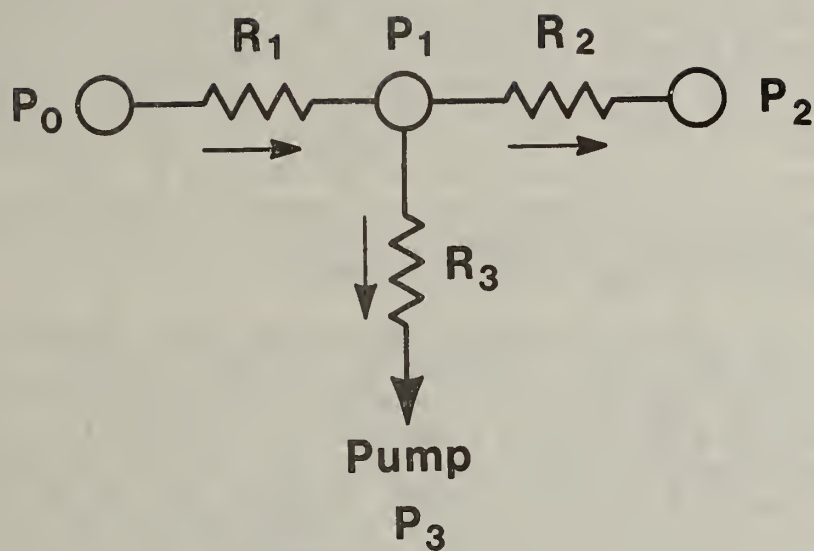


Fig. 62. Flow divider network: R_1 -capillary tube under laminar flow. R_2 -capillary tube under molecular flow. R_3 -thin orifice under molecular flow. $P_0 \sim 1$ atm. $P_2, P_3, \ll P_1$. Flow rate in $R_3 \gg$ flow rate in R_2 .

FLOURESCENT GLASS STANDARDS FOR USE IN DYE PENETRANT TESTS

R. W. Burke and D. K. Hancock

Inorganic Analytical Research Division

Center for Analytical Chemistry

Fluorescent dye penetrant testing continues to be one of the most widely used nondestructive methods for detecting minute cracks and flaws in metallic surfaces. The basic test, as performed currently, is essentially the same as originally developed. It entails coating the part to be tested with the fluorescent dye penetrant, wiping off the excess dye from the exposed surface, applying a developer, and measuring the fluorescence of the resulting indication. While many improvements have been made in the formulation of highly sensitive penetrants, efforts to reproducibly quantify these improvements in terms of their relative fluorescent brightness and crack-measuring capabilities continue to be thwarted by the nonavailability of suitable fluorescent standards for calibrating the test equipment.

Our initial efforts to develop fluorescent glass standards for use with various NDE tests were described in last year's report. At that time, two types of standards were perceived. One consisted of a rectangular piece of uranium-doped glass mounted in a metallic heat sink for enhancing temperature stability; the other type was an assemblage of glass fibers having a series of graded diameters and uranium concentrations. The first type of standard was intended for the reproducible calibration of spectrofluorimetric instrumentation while the second type was envisioned as a working standard for improving the reliability with which the intensities and widths of fluorescent indications could be measured.

As a result of understanding more clearly the needs of industry and the problems associated with their "mass production," several changes in the makeup and design of these standards were considered desirable. During the past year, efforts have focussed on perfecting these changes. The most significant change was the decision to seek an alternative fluorescent glass that could be substituted for the uranium-doped glass used initially. Two factors were instrumental in this decision. The predominant factor was that the fluorescent temperature coefficient of uranium-doped glass is much larger than originally anticipated. Our measurements have shown that the fluorescence of this glass decreases approximately 0.9 percent per degree Celsius in the temperature range of 20-40°C. A second factor was a safety issue involved in the in-house production and fabrication of uranium-containing materials. Subsequent studies showed that the fluorescence of terbium-doped glass is very similar to that of uranium-doped glass. Like uranium, terbium-doped glass fluoresces in the green region of the spectrum and as a consequence exhibits excellent coincidence with both the fluorescence emission

of most dye penetrants and the mesopic sensitivity of the human eye. In addition, the range of fluorescent intensities obtainable with terbium-doped glass is relatively large since doping levels up to 45 to 50 weight percent are possible. Its main advantage for use as a standard, however, is the fact that its fluorescent temperature coefficient is at least an order of magnitude smaller than uranium-doped glass and thereby displayed the minimum kind of improvement that we were seeking. The other major change in our research efforts has concerned the approach to producing a fluorescent standard that can be used in conjunction with the measurement of crack indications. Because of significant handling and mounting problems, the glass fiber approach has been replaced by a system in which fluorescent indications of varying widths and relative intensities are obtained by ruling a series of narrow slits in opaque films that have been evaporated directly on polished glass flats having different terbium concentrations. Six to eight slits per side are planned with widths ranging 5 to 100 micrometers.

Current efforts are concerned with the systematic evaluation of the various formulations of terbium-doped silicate and phosphate glasses now on hand and the subsequent selection of one of these as the base formulation that will be used for the preparation of the two types of fluorescent standards being proposed. At the present time, the phosphate glasses have the apparent advantage because they are intrinsically more fluorescent. This property may be due to the fact that the phosphate matrix is more transparent to ultraviolet radiation and hence the energy reaching the terbium fluorophor is more intense. Once the optimum base glass composition has been chosen, it will be fabricated into forms that are easily incorporated in NDE tests. As an instrumental calibrant, particular emphasis will be placed on providing a configuration and size that is directly usable in the Turner, Model 111, fluorometer. During the same time, the final decision will be made on which evaporated film will be used in the production of the simulated crack indication standard. The goal here is to identify a film that is durable, exhibits a matte finish which closely approximates that of a typical metal specimen, and can be properly ruled. Based on the projected progress, it is believed that sample of both types of standards will be ready for field evaluation by the end of the calendar year.

DYE PENETRANT CRACK RESEARCH

David Lashmore and David Kelley

Materials Chemistry Division

Center for Materials Science

Introduction

Dye penetrant crack SRM's have been in production for two years and last year more than 100 were made. This SRM is fabricated using an electro-forming technology and consists of alternative layers of copper and nickel. There are four layers of copper: the thickest is nominally 2 μm , then next 1 μm , followed by 0.5 μm and 0.2 μm . These copper layers are then electrochemically removed and the space that the copper occupied constitutes the crack. This research project was undertaken to improve various unsatisfactory manufacturing techniques and to investigate several important aspects of the crack geometry that have a bearing on dye pick-up and apparent crack width. Among the topics that were examined were (a) the extent to which the crack edge was "rounded" by the etching procedure; (b) the depth to which the crack penetrated into the block; (c) the polishing technique which was known to "smear" the nickel over the copper; and (d) various techniques to automate the production process.

Results

In order to eliminate as much as possible the rounding of the crack, an improved etching technique was developed. As shown in figure 63, the nickel is theoretically dissolved at a potential lower (more cathodic) than is copper. By placing the nickel/copper laminate in a solution of chromic-sulfuric acid and setting the potential in region I, it theoretically is possible to dissolve only the copper and at the same time avoid producing an appreciable amount of hydrogen. This potential was accurately determined experimentally. Once this potential was determined the previously used two electrode system was modified to include a calomel electrode.

The polishing procedure was changed drastically to reduce to the maximum extent possible the smearing of the nickel and at the same time the polishing procedure was automated. Optimal polishing times were determined. The most significant change was in adopting all diamond polishing abrasives. The previously used aluminum oxide was found to produce a significant amount of deformation. Since this smearing was accentuated by hand polishing all hand polishing steps were removed and our automatic metallography station was relied upon for each step in the surface preparation.

The depth of the crack was determined for the first time. Typical values for one laminate are shown in Figure 64.

Because of the unexpected large depth of the cracks, further research on the effect of etching on dye pick-up seemed unwarranted. Indeed, it would seem possible to reduce the etching time even further.

Table 1. Nominal Crack Depths for the Current Dye Penetrant Test Standard

Line No.	Nominal Width (μm)	Actual Width (μm)	Crack Depth (μm)	D/W
1	2.0	1.89	131	69
2	1.0	0.75	82	109
3	0.5	0.65	26	40
4	0.25	0.18	21	116

Changes in the sample geometry were made to speed up production and to ensure more uniform polishing. These changes were the inclusion of a stainless steel ring surrounding the laminate to keep the sample from rounding and changing the epoxy mold geometry so that mounting of the samples in the holder would result in the sample being exactly parallel to the plane of polishing.

Conclusion and Remarks

1. Procedures have been developed to avoid rounding of the crack edge.
2. The crack depth-to-width ratio has been determined to exceed 40 for all crack widths and to be as high as 116 so that the effect of etching time on dye pick-up is most probably negligible after a given critical etch time has passed.
3. Polishing procedures have been developed to minimize smearing of the nickel.
4. Production has been automated to the maximum extent possible.

The remaining problem with this SRM is the tedious technique used to measure the crack widths. The first three lines are measured on an old optical microscope (for each and every crack) which has rather poor resolution. The finest line is measured on the SEM using a statistically significant number of samples and assuming that the remainder of standards have the same spacing. This is probably a reasonable assumption as the standards are all cut from the same sheet.

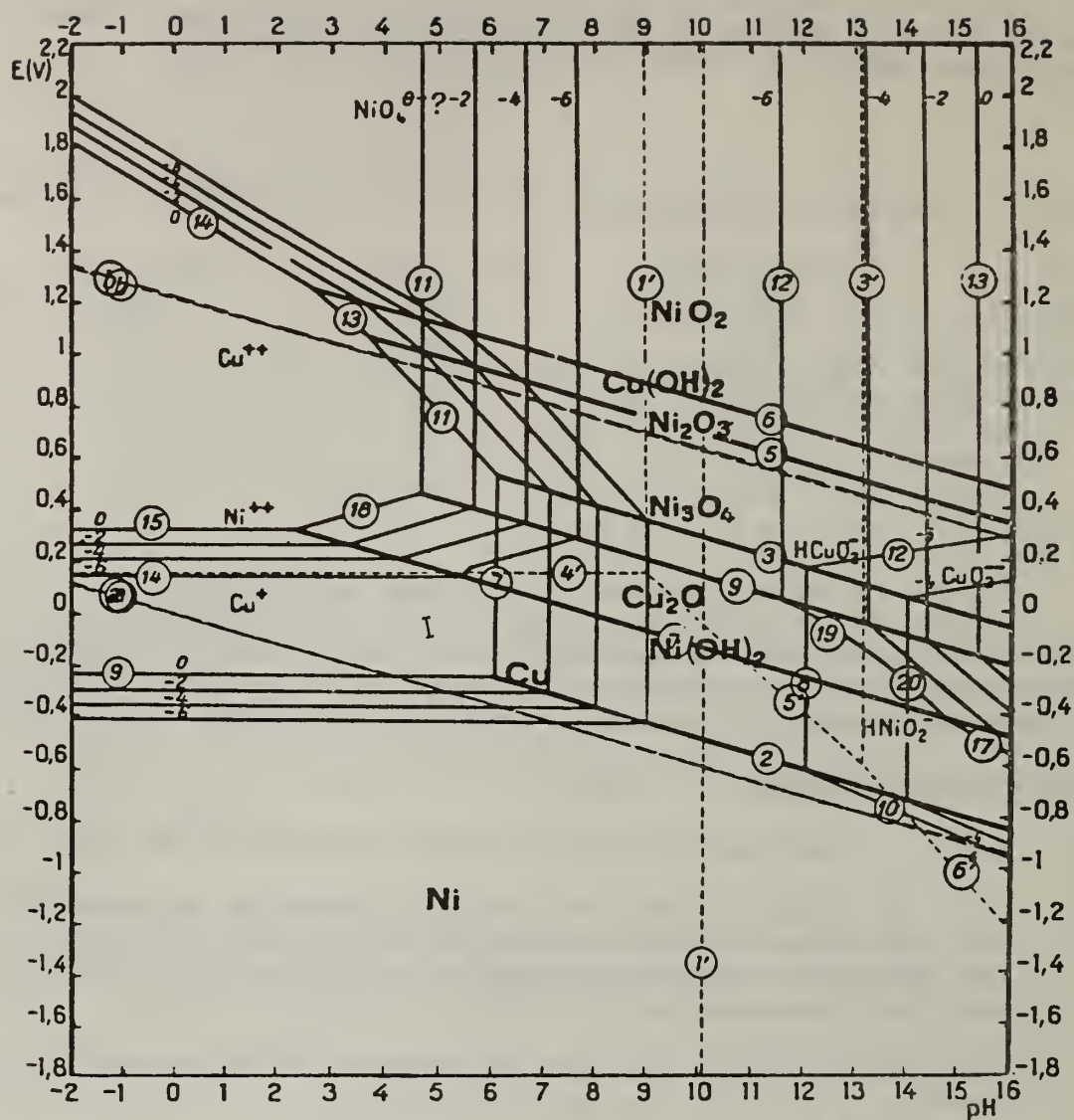


Figure 63. Pourbaix diagram of copper superimposed upon the Pourbaix diagram for nickel.



(a) 2 μm line (235X)



(b) 0.25 μm line (2.3KX)

Figure 64. Crack Depth Profiles.

WEAR CONDITION MONITORING

A. W. Ruff

Metallurgy Division

Center for Materials Science

This research involves techniques of acoustic emission and wear debris recovery from laboratory and field-operating systems that are undergoing wear. In cases of rotating machinery such as gas turbines and pumps, wear of bearings and other components is frequently the life-determining process. Different methods can be used to monitor such mechanical systems, including thermal measurements, vibrational measurements, etc. More direct methods are very desirable, for example, recovery of wear debris from the lubricant, since they bear directly on the problem. However, the capability for early warning of damage, an important issue, varies greatly with the method. We have worked with many groups outside NBS on the use of wear debris as an early warning method; this has been successful in some cases. Project effort is now concentrated on using acoustic signals.

Acoustic emission detection is being used in a study of metallic wear in order to monitor particular wear events such as subsurface crack growth (delamination). While the noise and vibration background in a typical wear test situation can be complex, it may be possible to remove such interferences in the detected ultra-sonic signals by using filtering, synchronous detection schemes, and computer based signal processing. A laboratory bench wear tester has been instrumented with an acoustic detection system and recorder. An incremental stressing contact geometry (consisting of a raised portion on the rotating ring counterface) is used, and the anticipated emission events are searched for in synchronism with the load pulses. Three different steels having varying toughness have been studied; and copper has also been examined briefly, all sliding under lubricated conditions against 52100 steel counterfaces. Some unusual emitted waveforms have been detected from the steel specimens, but they do not occur with every load pulse. Digital pulse recording and analysis will be tried next in order to obtain better resolution of the waveform details. This work is carried out in coordination with the other acoustic emission work in the Metallurgy Division concerned with signal analysis and source characterization. Plans next year include a wear study of other crack-sensitive steels, using digital acoustic pulse detection and characterization techniques. It is planned to accomplish this work in close collaboration with the acoustic emission effort in the Metallurgy Division.

ENGINE CONDITION MONITORING THROUGH OIL ANALYSIS

Stephen M. Hsu

Materials Chemistry Division

Center for Materials Science

Highly formulated lubricants are often used to lubricate various high load, high stress modern engines in various powertrains. One of the major causes of premature engine failure is lubricant breakdown which causes corrosion, fatigue, wear, and sometimes sudden seizure/welding. The object of this project is to develop test methods to measure and understand the degradation of lubricants and its relationship with engine wear/failures.

Conventional oil analysis techniques include infrared spectroscopy and wear metal analysis by emission spectroscopy or ferrography. Emission spectroscopy measures metal particles mostly less than 1 μm . Ferrographic method is effective only for iron (magnetic) wear particles at 1 μm or above. All three techniques function reasonably well in clean oil systems. With normal used oils which are contaminated by airborne particles, oxidized oil components, and wear particles, analysis becomes difficult. Recent ASTM round robin results on oxidation and nitration in used oils by infrared spectroscopy indicated complete disagreement among a score of oil company labs. One major technical problem is how to set condemning limits for various parameters that are measured. High levels of wear metals in used oil indicate incipient seizure and the time to failure may be very short. Oil analysis usually measures oxidation degradation and sometimes contamination, but their relationship to wear and failure are not clear.

During the past year, some key experiments were performed. A carefully selected lubricant with known engine performance was degraded in the laboratory under controlled conditions. Various state-of-the-art measurement techniques as well as conventional oil analysis methods were used to follow the degradation pathway of the oil. Periodic samples were withdrawn and tested in NBS developed laboratory engine simulation tests. We found a definite correlation between additive depletion and increase in wear. However, secondary interactions between additive decomposition products and base oil oxidation products were able to provide additional wear protection but not the load carrying capability of the lubricant. Results are shown in Figures 65 and 66.

In Figure 65, (from left to right) the viscosity of the oil remains relatively stable until about 120 hours. At that time, the viscosity increases sharply to over 800% of the original oil viscosity. The antioxidant capacity is measured by the Ford free radical titration method (1) which measures the ability of the oil to decompose free radicals. We see that the antioxidant capacity drops sharply under oxidation at about 50 hours (antioxidant depletion/degradation). However, it rises again to about the half of the original values. This suggests secondary reactions between the base oil and additive degradation products to regenerate anti-oxidant species. The seizure load (2) indicate the capacity of the lubricant to carry a certain load without seizure. The data in Figure 65 suggest that the seizure load decreases by 30% in the first 50 hours coincidental with the additive depletion. After 50 hours, test results suggest frequent seizures and erratic friction traces and a clear seizure load was difficult to determine. The amount of wear increases about 30% and remains level after 50 hours. Differential infrared results on the phosphorus sulfur bond (characteristic bond of the anti-wear additive zinc dithiophosphate) suggests that the antiwear additive is exhausted in the first 50 hours. This confirms the observed wear and seizure load measurement.

In Figure 66, additional parameters measured in the same experiment are presented. The viscosity increase and the antioxidant capacity are shown for reference. The oxidation induction times are measured with the thin film oxygen uptake test (TFOT) which has demonstrated correlation with engine oxidation results (3). The oxidation induction time drops quickly and reaches a minimum at about 20 hours. This decrease in oxidation stability suggests additive depletion and is in agreement with the antioxidant titration results. After 20 hours, the oxidation stability of the oil increases gradually, again suggesting antioxidant regeneration. Differential infrared measurements on carbonyl (carbon oxygen bond) suggest a continuous rise in the oxidation process independent of other processes. The total acid number measures the organic acidic species formed under oxidation. The data in Figure 66 indicate stepwise increases with different slopes. The acidic species begin to form at about the 75th hour with steep slope. At about the 120th hour, the formation rate decreases and the viscosity increase begins to rise sharply. Average molecular weights as measured by gel permeation chromatography (GPC) indicate a constant level until about the 130th hour.

These results are interesting and significant. Contrary to conventional theories, drastic failure did not occur when all the additives were exhausted. In fact, the original additives were exhausted in the first 40 hours, yet the viscosity failure did not occur until about 120 hours. Coincidental with the viscosity increase, the acidic species in the oil reach a certain level (TAN = 12). The load carrying capacity, however, appears to correlate with the additive depletion.

Controlled experiments with a single lubricant degradation suggest some condemning limits on used oil properties. Three new test procedures have been developed and proven useful in oil analysis for engine condition monitoring. Future work will test other lubricants and additives in an oxidation wear coupled system.

REFERENCES

- (1) Mahoney, L. R. et al, "The Determination of the Antioxidant Capacity of New and Used Lubricants: Method and Application," Ind. Eng. Chem., Prod. Res. and Develop., 17, 250, 1978.
- (2) Gates, R. S. and Hsu, S.M., "Development of a Four-Ball Wear Test Procedures to Evaluate Automotive Lubricating Oils," ASLE preprint no. 82-AM-6A-4, Presented at the ASLE meeting, Cincinnati, Ohio, May, 1982.
- (3) Ku, C.S. and Hsu, S.M., "A Thin-Film Oxygen Uptake Test for the Evaluation of Automotive Lubricants," Presented at the ASLE/ASME joint conference, Washington, D.C., October 7-9, 1982.

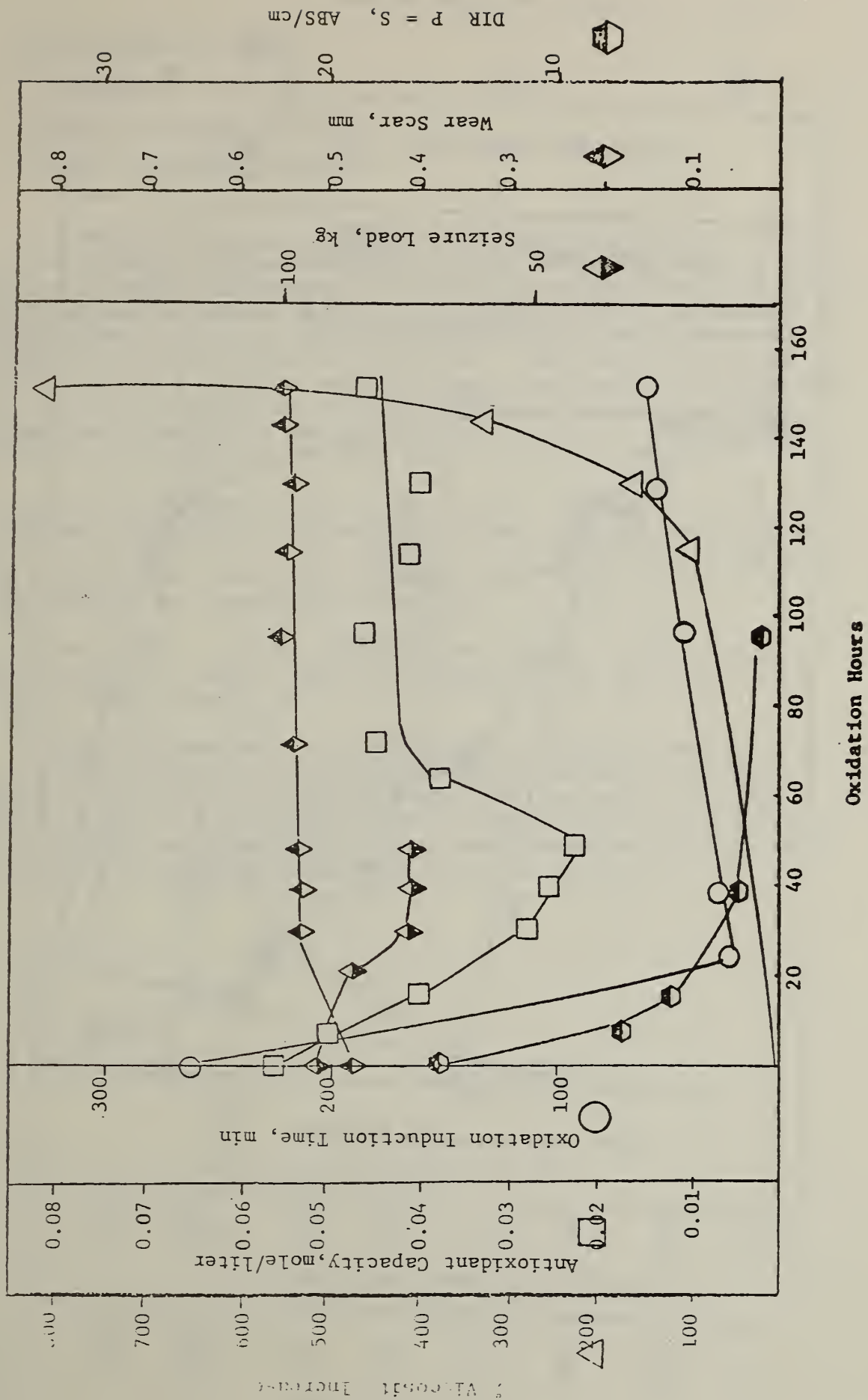


Fig. 65. Effects of Oxidation on Wear

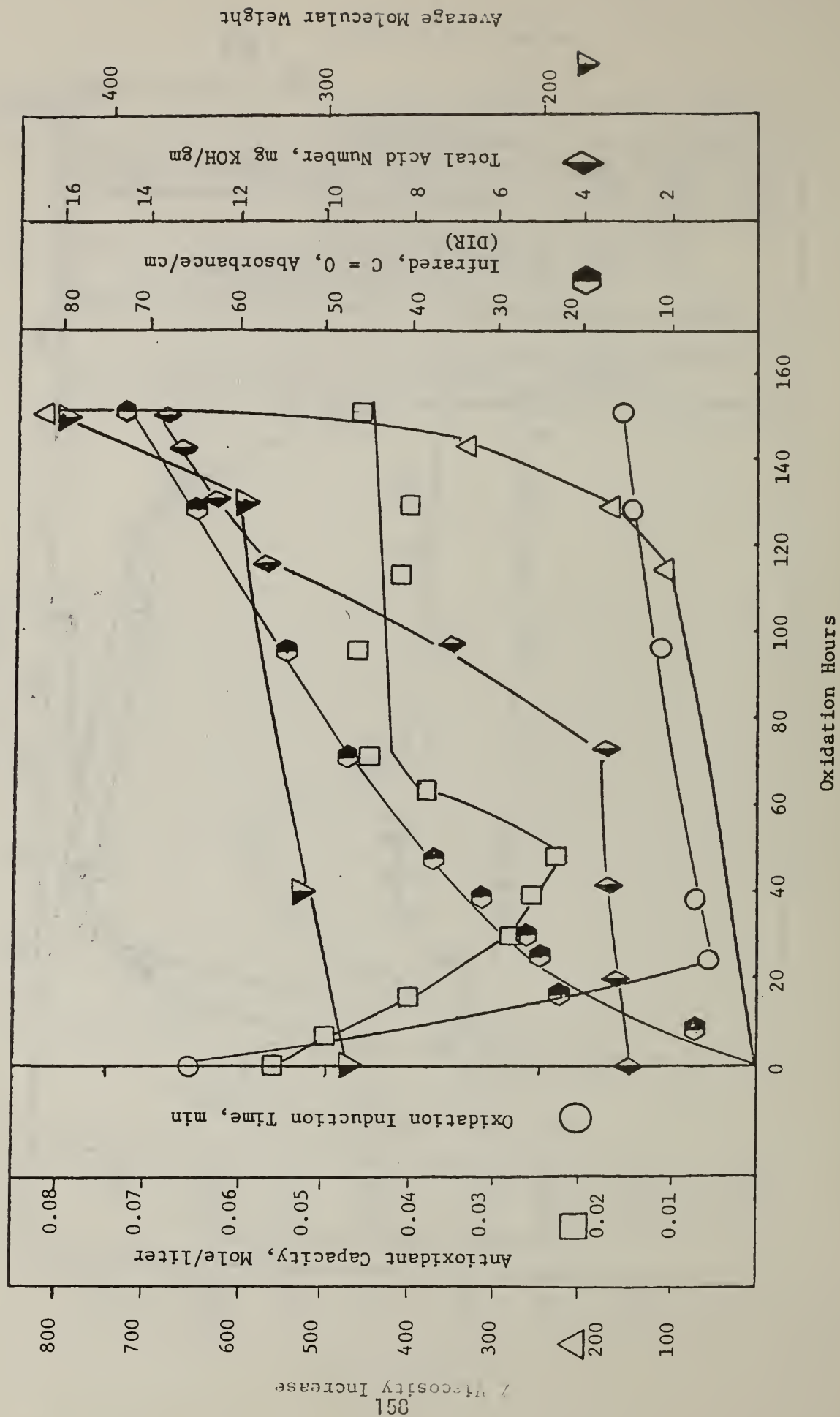


Fig. 66. Effects of Oxidation on Oil Properties

ELECTROMAGNETIC NOISE

U. Bertocci

Materials Chemistry Division

Center for Materials Science

Electrochemical noise measurements have been taken on Fe-Cr alloys of three different Cr concentrations, in order to examine random fluctuations of the current under potentiostatic conditions when these alloys are in passive conditions, both in the absence and in the presence of chloride ions in solution, which can cause pitting. Noise measurements were taken before and after pit initiation. These measurements were carried out with a computer-controlled apparatus, based on a two-channel spectrum analyzer, which can distinguish between fluctuations of the current due to changes in the electrode characteristics and noise induced by the input signal. See Fig. 67.

No noise could be detected in the absence of chlorides, while significant fluctuations were observed in their presence, both before and after pit initiation. The results indicate that the most important role of chlorides is to induce breakdown in the passive film, rather than affecting the repassivation kinetics.

These results also show that noise analysis, as an NDE method, has the feasibility to detect significant changes in the amplitude before pitting actually starts.

Another application of noise measurements in electrochemistry, the determination of the electrode impedance using a white noise input signal, has been used to study the transition from passive to trans-passive dissolution in stainless steels. Comparison with more traditional methods has shown that impedance measurements employing noise are at least as accurate and considerably easier to carry out.

Fe-12%Cr Alloy

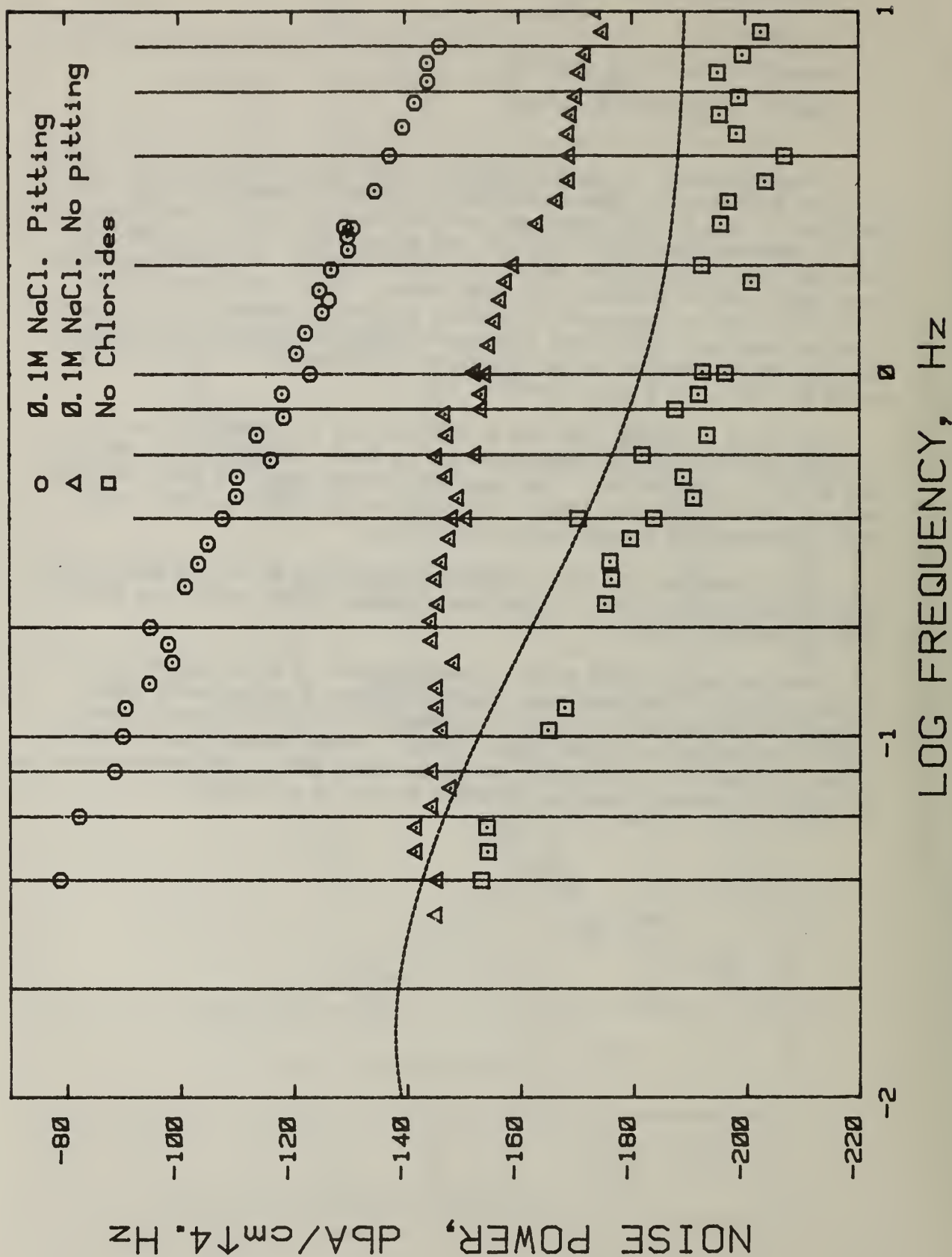


Fig. 67. Noise power spectrum for Fe-12% Cr alloy in pitting and non-pitting regimes. Line indicates noise level contributed by instruments.

ANALYSIS AND MODELING OF NDE ROUND-ROBIN DATA FOR ENGINEERING APPLICATIONS

J. T. Fong

Mathematical Analysis Division

Center for Applied Mathematics

This project was initiated in 1978 to answer the following question:

"When a flaw is detected by two or more NDE teams with different numerical answers for its location and size, is there a rigorous method to compute a single set of numbers to characterize the flaw with a confidence interval to permit the assignment of an engineering safety factor?"

The answer was no when NBS undertook in 1976 a study on the structural integrity of 612 welds of the Trans-Alaska Oil Pipeline. The answer today is still in the negative because controlled experiments in nondestructive evaluation of flaws are rarely conducted and human factors are significant in almost all NDE processes.

Nevertheless, it is possible to develop a data analysis and variability modeling methodology such that round-robin NDE data from carefully planned and well-conducted test programs can yield useful information for engineering applications.

For example, as early as 1965, the Pressure Vessel Research Committee (PVRC) of the Welding Research Council recognized the need to assess the reliability of weldment inspection techniques through an industry cooperative round-robin test program. A total of 12 plate-weld specimens containing intentional flaws of various types were fabricated and inspected by industry teams using techniques and procedures prescribed by PVRC. Upon the completion of the round-robin test program, each specimen was or will be sectioned to verify the true location and size of each flaw as well as to study the reliability of each NDE procedure.

At the invitation of Mr. H. C. Graber, then Chairman of PVRC Subcommittee on NDE of Pressure Components, Fong began the application of an analysis methodology to a complete set of sectioning and round-robin data for PVRC Specimen 251-J in Sept. 1981. The analysis methodology has been under development by Fong as part of the objective of this project. The availability of the PVRC data with true values of the flaw location and size provides for the first time an opportunity to address both the precision and the accuracy questions of an NDE procedure.

The analysis methodology consists of five basic steps: (a) Data Representation; (b) Multi-Level Data Reduction; (c) Variance Analysis; (d) Variability Modeling; (e) Data Retrieval and Display. An analysis of variance technique due to Mandel (1977) and first applied to fatigue and NDE data by Fong (1979, 1981) was implemented in this methodology for generic applications. Example of some preliminary application of the methodology

(steps (a) and (e)) to PVRC data is given in Figures 68, 69, 70. Five sets of data for PVRC Specimen 251-J are currently being analyzed by Fong and his colleagues with partial financial support from the industry-based Pressure Vessel Research Committee.

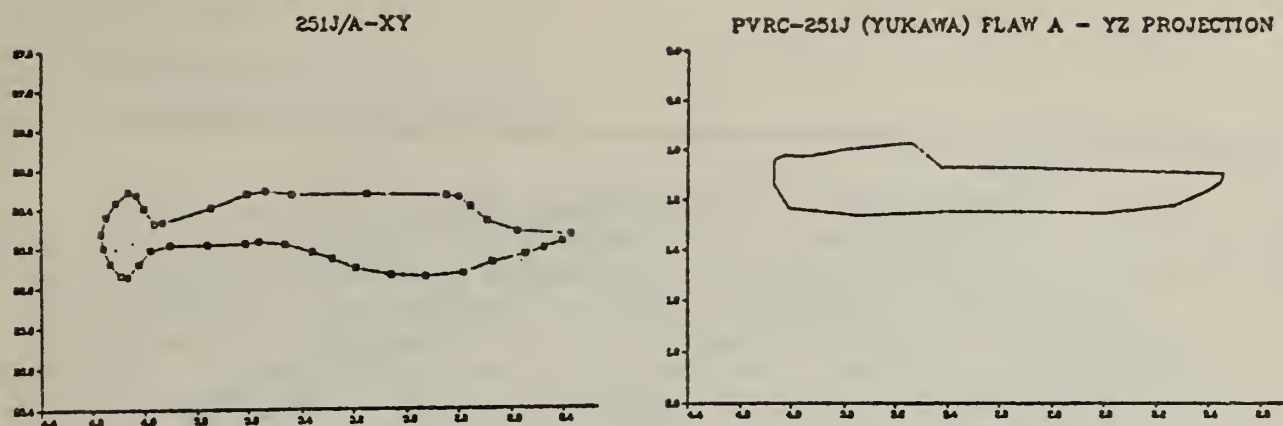


Fig. 68. 2-dim. Computer Graphics Based on Flaw Sketches Furnished by Yukawa of G.E.-Schenectady (1981).

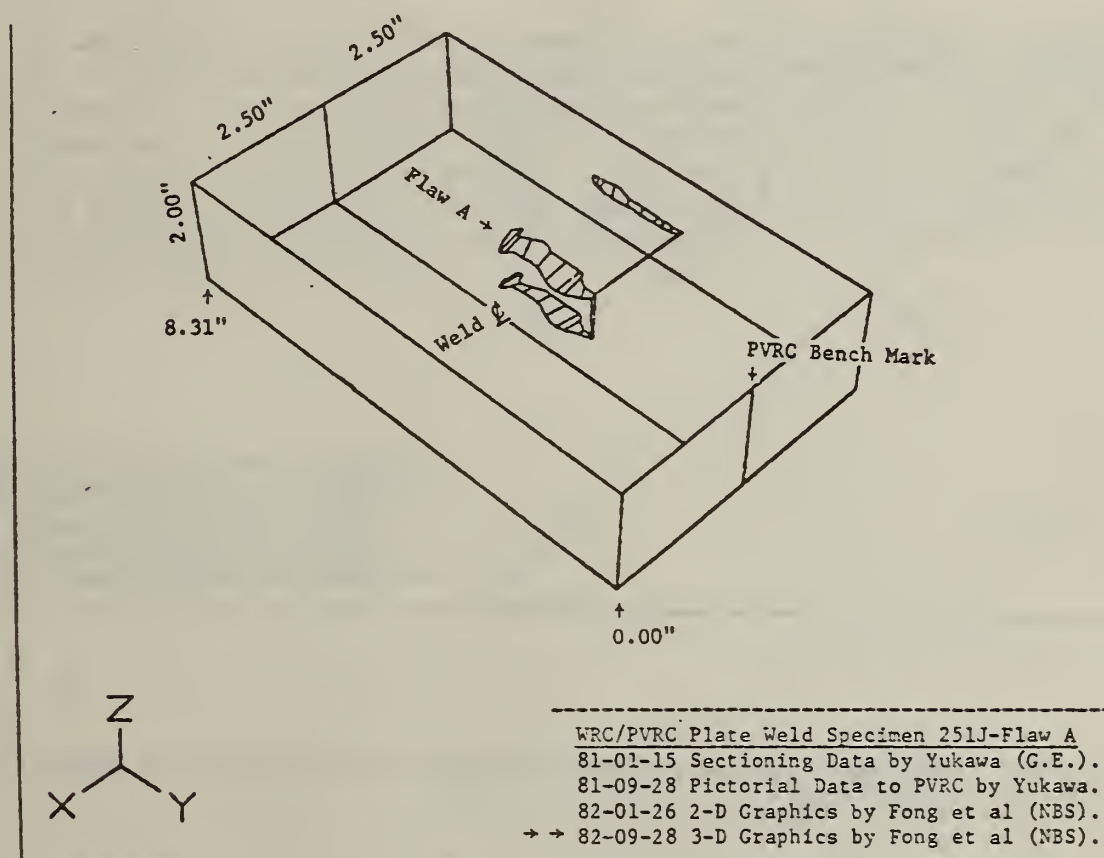


Fig. 69. 3-dim. Computer Graphics for Flaw and Weldment (Fong, 1982).

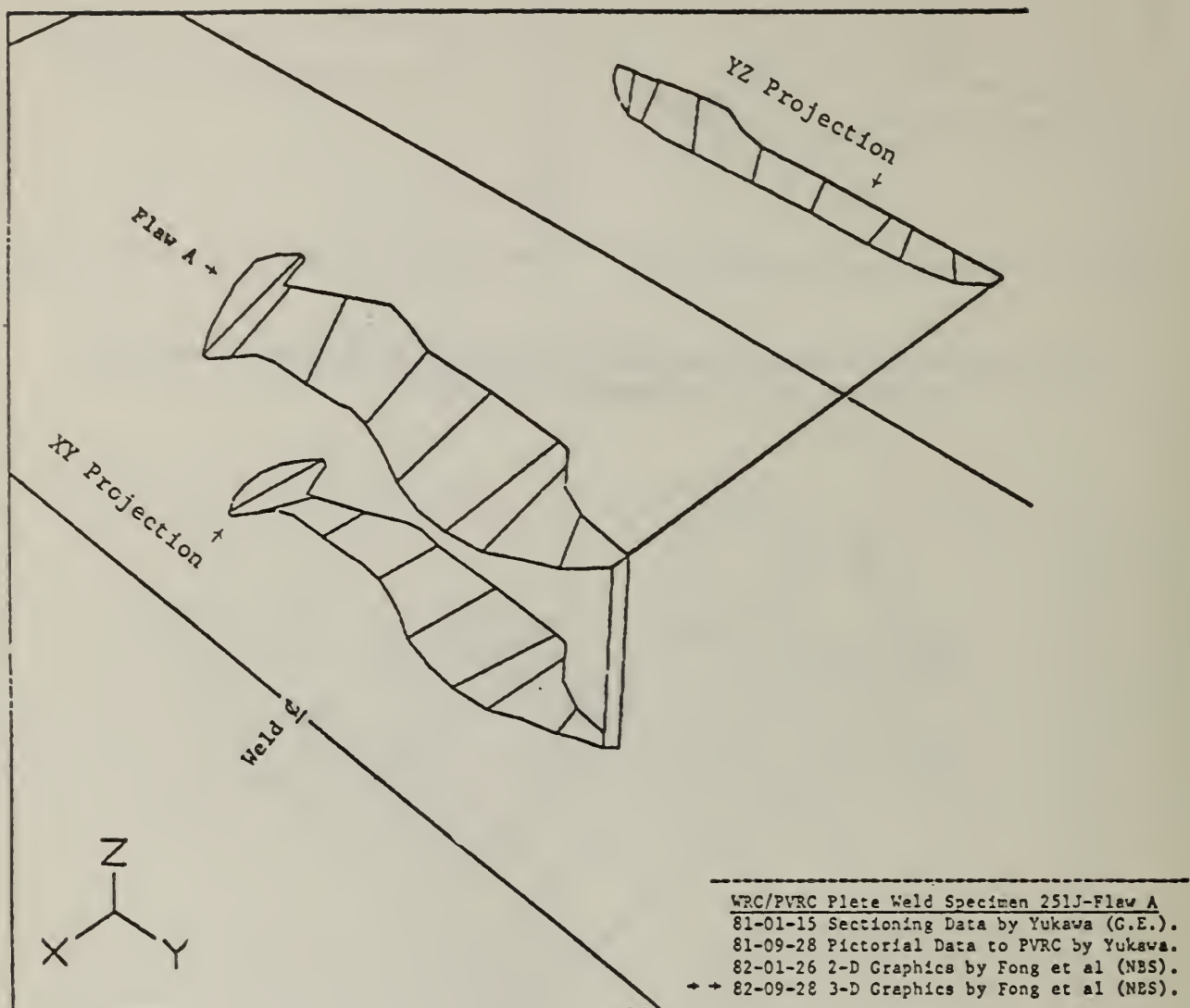


Fig. 70. Enlarged View of Flaw and Weldment for Variability Modeling (Fong, 1982).

USE OF NDE IN REHABILITATION AND PRESERVATION

J. Clifton

Building Materials Division

Center for Building Technology

An important phase of the rehabilitation or preservation of concrete and masonry structures is deciding whether to repair, reinforce, or replace concrete and masonry materials and building components. Information on the condition of the concrete and masonry materials, including any internal metal reinforcement, is usually required before such decisions are made. The traditional process of condition assessment includes making a visual inspection of the structure, characterizing the important properties of a material using cored and other samples, and making an engineering analysis of structural components. For condition assessment purposes, the use of nondestructive evaluation (NDE) methods can be beneficial. For example, while NDE does not entirely eliminate the need for taking samples and analyzing or mechanically testing them, it does substantially reduce the amount of such testing.

NDE techniques applicable to determining the condition of concrete and masonry in structures being rehabilitated have been identified and assessed. The assessment of these techniques were based on consideration of usefulness of information obtained, reliability, and expertise required to use the equipment and to interpret the results. The results of the assessment are given in a paper submitted to the American Concrete Institute for publication in a special publication dealing with rehabilitation and preservation of concrete and masonry structures.

APPENDICES

A. NDE Related Conferences

1. Deformation, Fracture, Wear and Nondestructive Evaluation of Materials, Nov. 23-24, 1981, New Orleans, LA.
2. Time-Dependent Failure Mechanisms and Assessment Methodologies, 35th Mechanical Failures Prevention Group Meeting, April 20-22, 1982, National Bureau of Standards.
3. Seventh International Symposium on Ultrasonic Imaging & Tissue Characterization, June 6-9, 1982, National Bureau of Standards.
4. Process Control Sensors for the Steel Industry, July 27-28, 1982, Gaithersburg, MD.

B. NDE Seminars Organized

<u>Speaker</u>	<u>Date</u>	<u>Topic</u>
L. W. Kessler Sonoscan, Inc.	March 9, 1982	Acoustic Microscopy: Methods, Applications, Outlook
J. A. Swets Bolt Beranek & Newman, Inc.	April 23, 1982	Evaluation of NDE Systems

C. Invited Talks by NDE Office Personnel

1. "Condition Monitoring of Machines," L. Mordfin, American Physical Society, New Orleans, LA, November 24, 1981.
2. "Recent Developments in Non-Destructive Evaluation Measurements at the NBS," G. Birnbaum, Howard University, January 8, 1982.
3. "Calibration, Reference Standards, and Traceability to NBS in NDE," L. Mordfin, Symposium on Validity of NDE Measurements, Butler County College, Butler, PA, February 3, 1982.
4. "NDT Measurements Traceable to NBS," G. Birnbaum, 10th World Conference on NDT, Moscow, USSR, August 23, 1982.
5. "Future Directions of Ultrasonic NDE Standards in the U.S.," G. Birnbaum, 10th World Conference on NDT, Moscow, U.S.S.R., August 23, 1982.
6. "Some Comparisons of Standards for Eddy Current Nondestructive Testing," 10th World Conference NDT, Moscow, U.S.S.R., August 26, 1982.
7. "Advanced Diffraction Techniques for the Nondestructive Evaluation of Internal Residual Stress," L. Mordfin, Seventh International Conference on Experimental Stress Analysis, Technion Israel Institute of Technology, Haifa, Israel, August 25, 1982.
8. "Standards for Quantitative NDE," L. Mordfin, Israel Aircraft Industries, Lod, Israel, August 29, 1982.

D. Awards

Industrial Research, IR-100 Awards

Kenneth Yee and Donald Blomquist of the NBS Automated Production Technology Division won an IR-100 Award for inventing a device that monitors the behavior of machines engaged in drilling holes and sends a warning signal when it senses that a drill is about to break. The "Drill-up" monitors the vibrations in the workpiece while it is being drilled. The device compares the vibration "signature" over a period of time and detects a periodic disturbance in the vibration that the researchers have found is characteristic of a drill that is about to break. "Drill-up" assures that the disturbance is not a random event and signals the machine control system to retract the drill and wait for a replacement.

Dr. Roald Schrack, Dr. C. Bowman, and Mr. J. Behrens, of the NBS Nuclear Radiation Division won an award for the design of a two-dimensional imaging system for resonance neutron radiography that can selectively display the position and concentration of any isotope or element in a complex specimen. The detector is designed for use with higher-energy pulsed neutron sources. The entire device has a sensitive area with a diameter of 2.5 cm. The information is stored by a computer-based data gathering system. The stored data can be used to reconstruct a neutron radiograph image "tuned" to any desired resonance, highlighting any element or isotope with that resonance.

NBS Silver Medal Award

Dr. R. Schrack, Dr. C. Bowman and Mr. J. Behrens were cited for developing Resonance Neutron Radiography which is described in more detail in the IR-100 Awards above.

NBS Bronze Medal Award

Dr. Nelson N. Hsu was cited for his outstanding contributions to the science and technology of experimental and theoretical mechanics and their resulting applications in research and industry. His work on acoustic emission and ultrasonics testing have greatly affected the quality and safety of structures.

NBS Applied Research Award

Dr. Donald G. Eitzen was cited for his unique contributions in applying research to the development of quantitative acoustic emission measurements. Work in his group has resulted in calibration services, major breakthroughs in design and development of an acoustic emission transducer and major advances in the theoretical understanding of stress wave propagation in structures and solids.

ASNT Gold Medal

Mr. Harold Berger received the distinguished American Society for Nondestructive Testing Gold Medal in recognition of his many years of continuing meritorious service to ASNT.

IEEE Fellow

Mr. George C. Harmon of the Center for Electronics and Electrical Engineering has been elected Fellow of the Institute of Electrical and Electronics Engineers. Mr. Harman was named for development of process control and screening procedures for microelectronic welding and bounding.

ASCE Awards

Mr. Jimmy James, a co-op student from Prairie View A & M Univeristy, is the recipient of two separate American Society of Civil Engineers scholarships. Mr. James received the Samuel Fletcher Tapman Scholarship and the B. Charles Tiney Memorial Scholarship.

E. Technical and Professional Committee Participation and Leadership

<u>Name</u>	<u>Parent Organ.</u>	<u>Activity</u>
H. Berger	ASTM	E007 Nondestructive Testing
		SC.01
		Radiographic Practice and Penetrimeters
		SC.05
		Neutron and Radiography
		SC.91
		USA Committee for ISO/TC135 (NDT)
		SC.92
		Editorial Review
		SC.98
		New Methods Review
	ASNT	Materials Evaluation Committee (Chairman)
		Technical Publications Division
		Penetrating Radiation Comm.
		Energy Systems Component Comm.
	American Nuclear Society	Isotopes & Radiation Division Awards Funding Committee
	American Society for Metals	Nondestructive Testing Committee (Chairman)
	American Society of Mechanical Engineers	Pressure Vessels and Piping Division - Decade of Progress Committee
	APS	member
	Brit. Inst. of NDT	member
	Sigma Xi	member
G. Blessing	ASTM	E7.06 on Ultrasonic NDE
		E28.13 on Residual Stress
	National Material Advisory Board	Committee on NDE of Metal Matrix Composites
Don Eitzen	ASTM	E7.06.02
		A1 Reference Blocks
		E7.04.02 AE Sensors

<u>Name</u>	<u>Parent Organ.</u>	<u>Activity</u>
D. Garrett	ASTM	E7.05
J. Hsia	International CIE Subcommittee	Chairman
N. Hsu	ASTM	E7.04 Acoustic Emission
L. Mordfin	ASTM	D20.10.23 Residual Stress
		E7.03 Magnetic Particle and Pentetrant Testing
		E7.08 Leak Testing
		E7.10.04 Infrared Methods, Chairman
		E9.02 Residual Stress Effects in Fatigue
		E28.13 Residual Stress Measurements, Chairman
	ASNT	Liaison Division
		Utilities Committee
		Visual Methods Committee
		Infrared & Thermal Methods Committee, Chairman
	SESA	Residual Stress Measurement Committee
	SAE	Nondestructive Test Methods Division
		X-Ray Fatigue Group
R. Placious	ASTM	E7.01.03 Radiographic Practices and Methods
	ANSI	PH2.34 Industrial X-Ray Film Sensitometry
D. Polansky	ASTM	E-7
		E-10
		F-12
	ANSI	PH 2-34

<u>Name</u>	<u>Parent Organ.</u>	<u>Activity</u>
T. Proctor	ASTM	E28.13.05 Ultrasonic Measurements
C. Teague	ANSI	B46 Surface Finish Measurements
T. Vorburger	ANSI	B46.1 Profile Methods
H. Yolken	ASM ASTM	NDT Committee Ad Hoc Committee Medical Device Standards

F. Publications

1. Journal Publications

1. "R & D Summary: A New Look at the NBS Programme in NDE," H. Berger, NDT International, Vol. 14, No. 5, pg. 292-293 (Oct. 1981).
2. "Radiation-Induced Acoustic Cavitation Threshold vs. Temperature for Some Liquids," M. Greenspan and C. E. Tschiegg, J. Acoust. Soc. Am. Res. Brief, 1982.
3. "Surface-Wave Displacement: Absolute Measurements Using a Capacitive Transducer," F. Breckenridge and M. Greenspan, J. Acous. Soc. Am. 69(4). Pg. 1177-1185, April 1981.
4. "Acoustic Emission Transducer Calibration by Means of the Seismic Surface Pulse," F. Breckenridge, J. Acous. Emission 1(2), pg. 87-94, 1982.
5. "An Improved Piezoelectric Acoustic Emission Transducer," T. Proctor, J. Acous. Soc. Am. 71(5), pg. 1163-1168, May 1982.
6. "Noise Measurements in Electrochemical Systems," U. Bertocci and Ye Xiang-Yang, Corrosion Protection (People's Republic of China), 1982
7. "Optical Techniques for On-line Measurement of Surface Topography," T. V. Vorburger and E. C. Teague, Precision Engineering, 3 (1981), pg. 6.
8. "Light Scattering from Manufactured Surfaces," E. C. Teague, T. V. Vorburger and Daniel Maystre, Annals of the CIRP 30 (1981), 563-570.
9. "Dyadic Green Functions for the Time-Dependent Wave Equation," Egon Marx and Daniel Maystre, Journal of Mathematical Physics 23 (1982) pg. 1047-1056.
10. "Elastic Constants of Polycrystalline Copper at Low Temperatures: Relationship to Single-crystal Elastic Constants, H. M. Ledbetter Phys. Stat. Solidi (a) 66 (1981) pg. 477-484.
12. "Predicted Single-crystal Electric Constants of Stainless-Steel 316," H. M. Ledbetter, Brit. J. of Nondestructive Test. 34, 1981, pg. 286-287.

2. Conference Proceedings

1. "What is NBS Doing in NDE?," H. Berger and L. Mordfin, 36th Annual Quality Congress Transactions, pg. 929-933 (1982).
2. "The 1976 NBS Study of Girth Welds in the Trans-Alaska Oil Pipeline," H. Berger, ASNT Paper Summaries, ASNT Fall Conference, Atlanta, GA (Oct. 1981).
3. "An overview: New Ideas in Nondestructive Evaluation," H. Berger, Rubber Chemistry and Technology, Vol. 54, No. 5, pg. 996-1002 (November 1981).
4. "Standards for Residual Stress Measurement," L. Mordfin, Residual Stress Effects in Fatigue, ASTM STP-776, pg. 2-12 (1982).

5. "Introduction to Residual Stress Measurement," L. Mordfin, Proceedings of DoT Symposium on NDT Measurement of Wheel/Axle Residual Stress, Cambridge, MA, 1981.
6. "Advanced Diffraction Techniques for the Nondestructive Evaluation of Internal Residual Stress," L. Mordfin, Proceedings of the 7th International Conference on Experimental Stress Analysis, pg. 602-603, (Aug. 1982).
7. "Toward the Nondestructive Characterization of Fatigue Damage in Composite Materials," L. Mordfin, Damage in Composite Materials, ASTM STP 775, pg. 7-15 (1982).
8. "Standards for Eddy Current Nondestructive Testing," G. Free, G. Birnbaum, H. Berger, V. Kljuev, Y. Fedosenko, 10th World Conference on Nondestructive Testing, Vol. 7-4, pg. 262-266 (1982).
9. "NDT Measurements Traceable to NBS," H. Berger, G. Birnbaum, D. G. Eitzen, 10th World Conference on Non-destructive Testing, Vol. P, pp. 58-65 (1982).
10. "Future Directions of Ultrasonic NDE Standards in the U.S.," G. Birnbaum, D. G. Eitzen, 10th World Conference on Non-destructive Testing, Vol. 7-5, pp. 267-272 (1982).
11. "The Inverse Problem of Acoustic Emission -- Explicit Determination of AE Source-Time Functions," N. Hsu and D. Eitzen, DARPA/AF Review of Quantitative NDE, Boulder, CO, August 1981.
12. "Traceable NDE Standards," G. Birnbaum, H. Berger, and D. Eitzen, Proc. of the 13th Symp. on Nondest. Eval, April 21-23, 1981, San Antonio, TX. (Also to appear in Materials Evaluation.).
13. "NBS Developments in Quantitative Acoustic Emission Measurements," D. Eitzen, F. Breckenridge, R. Clough, N. Hsu, T. Proctor, and J. Simmons, Proc. of the DARPA/AF Review of Quant. NDE, Boulder, CO, Aug. 1981 (in press).
14. "Dynamic Monitoring of the Precipitation Hardening Process in 2219 Aluminum Alloy by Means of Sound Velocity and Attenuation Measurements," M. Rosen, E. Horowitz, S. Fick and R. Mehrabian, Proc. of the Ultrasonic Symp, Chicago, Oct. 1981.
15. "Ultrasonic Standard Reference Blocks - What Future?" G. Blessing and D. Eitzen, ASNT Conf. Proc., Columbus, OH, (to be published Oct. 1982).
16. "Calibration of Acoustic Emission Transducers: Comparison of Two Methods," F. Breckenridge, T. Watanabe, and H. Hatano, Proc. of the 6th Int. Acoust. Emission Symp., Japan, Oct. 31-Nov. 3, 1982.
17. "Noise in Electromagnetic Systems," U. Bertocci, 6th International Conference on Noise in Physical Systems. NBS Special Publication 614 (1981).
18. "Development of In Situ Techniques for the Detection of Corrosion of Copper Concentric Neutrals of Electric Cables in Underground Environments," E. Escalante, U. Bertocci, J. Mullen, M. Cohen, and J. Kruger, IEEE/Power Engineering Society 1981 Transmission and Distribution Conference, September 20-25, Minneapolis, Minnesota (1981).

19. "Evaluation of Methods for Characterizing Surface Topography of Models for High Reynolds Number Wind-Tunnels," E. C. Teague, T. V. Vorburger, F. E. Scire, S. M. Baker, S.W. Jensen, C. Trahan, and B. B. Gloss, Proceedings of the AIAA 12th Aerodynamic Testing Conference, March 22-24, 1982, Williamsburg, VA p. 246-251.
20. "Elastic Constrants and Internal Friction of Fiber-reinforced Composites," H. M. Ledbetter, Composite Materials: Mechanics, Mechanical Properties and Fabrication, (Japan Soc. Compos. Mater. Tokyo, 1981), p. 65-70
21. "Single-crystal Elastic Constants in Nondestructive Evaluation of Welds," H. M. Ledbetter, in Review of Progress in Quantitative Nondestructive Evaluation (Plenum, New York, 1982).
22. "Stainless-steel Elastic Constants at Low Temperatures: A Review," H. M. Ledbetter, Proceedings ICMC, (Kobe, May 1982).

3. Reports

1. "Technical Activities 1981 - Office of Nondestructive Evaluation," H. Berger and L. Mordfin, Eds., NBSIR 82-2449 (Dec. 1981).
2. "NDE Publications: 1979," L. Mordfin, Ed., NBSIR 81-2351 (Oct. 1981).
3. "NDE Publications: 1980," L. Mordfin, Ed., NBSIR 81-2364 (Oct. 1981).
4. "Fundamental Developments for Quantitative Acoustic Emission Measurements," D. Eitzen, F. Breckenridge, R. Clough, E. Fuller, N. Hsu, and J. Simmons, EPRI NP-2089, Proj. 608-1, Palo Alto, CA: Electric Power Research Institute, Oct. 1981, 242 p.
5. "Electric Power Research Institute/National Bureau of Standards Joint Program on Acoustic Emission," D. Eitzen and J. Quinn RP608-3, Sect. 35 in Nondestructive Evaluation Program Progress in 1981. Coe Corp., eds., NP-2088-SR. Palo Alto, CA: Electric Power Research Institute, Dec. 1981, 35-1 - 35-18.
6. "Summary of Fundamental Developments for Quantitative Acoustic Emission Measurements," D. Eitzen, F. Breckenridge, R. Clough, E. Fuller, N. Hsu, and J. Simmons, EPRI NP-1877, Res. Proj. 608-1. Palo Alto, CA: Electric Power Research Institute, June 1981, 86 p.
7. "Ultrasonic Research Summary Report and Literature Guide to the National Bureau of Standards/Office of Naval Research Program," M. Greenspan and D. Eitzen, Nat. Bur. Stand. (U.S.), NBSIR 82-2529, June 1982.
8. "Ultrasonic Measurements of Titanium 6211 Weld and Plate," G. Blessing, Nat. Bur. Stand. (U.S.) NBSIR 82-2500, May 1982.

9. "Nondestructive Characterization of the Precipitation Hardness Process in Aluminum Alloys," M. Rosen, S. Fick, C. Friant, and E. Horowitz, Johns Hopkins U., Center for Matls. Res. Report No. CMR-NDE-2, Sept. 1981, 49 p.
10. "Correlation of Ultrasonic Data with Hardness after Aging 2024 Aluminum Alloy Under T4, TR351, and T851 Conditions," M. Rosen, S. Fick and E. Horowitz, Johns Hopkins U., Center for Matls. Res. Report No. CMR-NDE-4, Nov. 1981.
11. "Magnetostructively-Driven Ultrasonic Device for Sound Velocity Measurements in Thin Ribbons," F. Nadeau, S. Fick, M. Rosen and E. Horowitz, Johns Hopkins U., Center for Matls. Res. Report No. CMR-NDE-3, Nov. 1981.
12. "Integral Equations for Transient Electromagnetic Fields," Egon Marx, NBS Technical Note 1157, February 1982.

U.S. DEPT. OF COMM. BIBLIOGRAPHIC DATA SHEET (See instructions)		1. PUBLICATION OR REPORT NO. NBSIR-82-2617	2. Performing Organ. Report No.	3. Publication Date December 1982
4. TITLE AND SUBTITLE Technical Activities, 1982, Office of Nondestructive Evaluation				
5. AUTHOR(S) H. T. Yolken				
6. PERFORMING ORGANIZATION (If joint or other than NBS, see instructions) NATIONAL BUREAU OF STANDARDS DEPARTMENT OF COMMERCE WASHINGTON, D.C. 20234			7. Contract/Grant No.	
			8. Type of Report & Period Covered	
9. SPONSORING ORGANIZATION NAME AND COMPLETE ADDRESS (Street, City, State, ZIP)				
10. SUPPLEMENTARY NOTES <input type="checkbox"/> Document describes a computer program; SF-185, FIPS Software Summary, is attached.				
11. ABSTRACT (A 200-word or less factual summary of most significant information. If document includes a significant bibliography or literature survey, mention it here) A review of nondestructive evaluation programs at NBS, for FY1982 is presented in this annual report.				
12. KEY WORDS (Six to twelve entries; alphabetical order; capitalize only proper names; and separate key words by semicolons) Acoustic emission, eddy currents, imaging, leakage testing, magnetics, material parameters, nondestructive evaluation, optics, penetrants, radiography, and ultrasonics.				
13. AVAILABILITY <input checked="" type="checkbox"/> Unlimited <input type="checkbox"/> For Official Distribution. Do Not Release to NTIS <input type="checkbox"/> Order From Superintendent of Documents, U.S. Government Printing Office, Washington, D.C. 20402. <input checked="" type="checkbox"/> Order From National Technical Information Service (NTIS), Springfield, VA. 22161			14. NO. OF PRINTED PAGES 185	
			15. Price \$16.50	

